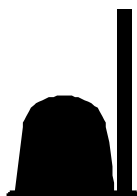


Organometallics in confined geometries:

Ferrocene in zeolite Y



The research described in this thesis was performed at the Neutron Scattering and Mössbauer Spectroscopy group of the Interfaculty Reactor Institute, Delft University of Technology, Mekelweg 15, 2629 JB Delft, The Netherlands.

Organometallics in confined geometries:

Ferrocene in zeolite Y

Proefschrift

ter verkrijging van de graad van doctor
aan de Technische Universiteit Delft,
op gezag van de Rector Magnificus prof. ir. K. F. Wakker,
voorzitter van het College voor Promoties,
in het openbaar te verdedigen op maandag 26 november 2001 om 13.30 uur

door

Ewout KEMNER

natuurkundig ingenieur
geboren te Amsterdam

Dit proefschrift is goedgekeurd door de promotoren:

Prof. dr. G. J. Kearley

Prof. dr. I. M. de Schepper

Samenstelling promotiecommissie:

Rector Magnificus,	voorzitter
Prof. dr. G. J. Kearley,	Technische Universiteit Delft, promotor
Prof. dr. I. M. de Schepper,	Technische Universiteit Delft, promotor
Prof. dr. S. W. de Leeuw,	Technische Universiteit Delft
Prof. dr. J. A. Moulijn,	Technische Universiteit Delft
Dr. A. M. van der Kraan,	Technische Universiteit Delft
Dr. H. Grimm,	Forschungszentrum Jülich
Dr. A. N. Fitch,	European Synchrotron Radiation Facility
Prof. dr. ir. C. W. E. van Eijk,	Technische Universiteit Delft, reservelid

Published and distributed by: DUP Science

DUP Science is an imprint of
Delft University Press
P.O. Box 98
2600 MG Delft
The Netherlands
Telephone: +31 15 27 85 678
Telefax: +31 15 27 85 706
E-mail: DUP@Library.TUdelft.nl

ISBN 90-407-2243-9

Keywords: neutron scattering, organometallics, zeolites

Copyright © 2001 by E. Kemner

All rights reserved. No part of the material protected by this copyright notice may be reproduced or utilized in any form or by any means, electronic or mechanical, including photocopying, recording or by any information storage and retrieval system, without written permission from the publisher: Delft University Press.

Printed in The Netherlands

Contents

Introduction	1
1 Theory	7
1.1.1 Introduction to neutron scattering	7
1.1.2 Basics of neutron scattering	7
1.1.3 Quasielastic neutron scattering	12
1.1.4 Reorientational motions	15
1.1.5 Intramolecular vibrations	18
1.2 Density Functional Theory	23
1.3 Atoms in molecules	27
2 Localization of ferrocene in NaY zeolite by powder X-ray and neutron diffraction	31
E. Kemner, A.R. Overweg, L. van Eijck, A.N. Fitch, E. Suard, I.M. de Schepper & G.J. Kearley, <i>Submitted to J. Phys. Chem. B</i>	
Abstract	31
2.1 Introduction	31
2.2 Experimental section	32
2.3 Structure determination	33
2.4 Discussion	42
2.5 Conclusions	46
3 How van der Waals bonds orient molecules in zeolites	49
E. Kemner, I.M. de Schepper & G.J. Kearley, <i>Submitted to Chem. Comm.</i>	
Abstract	49
3.1 Introduction	49
3.2 Results	50
3.3 Discussion	52
4 Molecular motion of ferrocene in a faujasite-type zeolite: a quasielastic neutron scattering study	55
E. Kemner, I.M. de Schepper, A.J.M. Schmets, H. Grimm, A.R. Overweg & R.A. van Santen, <i>J. Phys. Chem. B</i> 104 (2000) 1560	
Abstract	55
4.1 Introduction	55

4.2	Quasielastic neutron scattering	55
4.3	Experiment	56
4.4	Results	57
4.5	Discussion	60
5	The vibrational spectrum of solid ferrocene by inelastic neutron scattering	61
	E. Kemner, I.M. de Schepper, G.J. Kearley & U.A. Jayasooriya, <i>J. Chem. Phys.</i> 112 (2000) 10926	
	Abstract	61
5.1	Introduction	61
5.2	Experiment and results	63
5.3	Discussion	68
6	Ferrocene-zeolite interactions measured by inelastic neutron scattering	71
	E. Kemner, A.R. Overweg, U.A. Jayasooriya, S.F. Parker, I.M. de Schepper & G.J. Kearley, <i>Submitted to Appl. Phys. A</i>	
	Abstract	71
6.1	Introduction	71
6.2	Experiment	72
6.3	Computations	72
6.4	Results and discussion	73
6.5	Conclusions	77
7	Low frequency modes of ferrocene in zeolite Y	79
	based on E. Kemner, C.F. de Vroege, M.T.F. Telling, I.M. de Schepper & G.J. Kearley, <i>Submitted to Appl. Phys. A</i>	
	Abstract	79
7.1	Introduction	79
7.2	RKS experiment	80
7.3	IRIS experiment	85
7.4	Computations	85
7.5	Discussion and conclusions	91
	General discussion and conclusions	93
	Summary	97
	Samenvatting	99

A	Model independent determination of the elastic incoherent structure factor in neutron scattering experiments	101
	E. Kemner, I.M. de Schepper, A.J.M. Schmets & H. Grimm, <i>Nucl. Instr. Meth. B</i> 160 (2000) 544	
	Abstract	101
A.1	Introduction	101
A.2	Theory	104
A.3	Example	107
A.4	Conclusions	110
B	TOSCA and TFXA	111
	Dankwoord	113
	Curriculum Vitae	115

Introduction

The term 'catalysis' was first introduced in 1835 by the Swedish scientist Berzelius, who said that a catalyst is a compound that increases the rate of a chemical reaction, but is not consumed by the reaction. With this definition he instigated a debate which lasted throughout the remaining 19th century, until in 1887 the German Ostwald came up with the definition which is still accepted: 'A catalyst is a substance that accelerates the rate of a chemical reaction without being part of its final products.' The catalyst acts by forming intermediate compounds with the molecules involved in the reaction, offering them an alternate, more rapid path to the final products.¹ Catalysis is very important in a wide range of fields. The bio-chemical processes in a cell are governed by enzymes and proteins that act as catalysts. Many industrial chemical processes rely on catalysis, for instance in the production of plastics and fertilizers and in petroleum refining. Also, in environmental chemistry catalysts are essential to breaking down pollutants such as automobile and industrial exhausts.¹ For these latter, very sophisticated processes the use of highly selective catalysts is demanded. Zeolites offer the possibility to design such catalysts.

Popularly spoken zeolites are hydrated minerals with a very open porous structure. They occur both naturally and man-made. There are hundreds of different types of zeolites known at the moment, but more are still being developed. The word 'zeolite' literally means 'boiling rock' and is Greek in origin, coming from the words 'zein', to boil, and 'lithos', rock. It was coined in 1756 by the Swedish scientist Cronstedt who found that upon heating of the mineral stilbite, the sample evolved steam.²

More precisely zeolites are crystalline aluminosilicates with a three-dimensional open framework structure of channels and cavities of molecular dimensions formed by SiO_4 and AlO_4 tetrahedra bonded by the oxygen atoms at the corners of the tetrahedra. The tetrahedra can be linked in many ways, giving rise to different structures. Since the cavities and channels are of molecular dimensions they are, after water removal, accessible to guest molecules. Zeolites thus have the property of acting as sieves on a molecular scale, unlike other porous adsorbents such as activated carbons and alumina or silica gels that contain much larger sieves. Too large molecules will not be able to access the channel system in the zeolite. Catalytic centres in the interior of the zeolite are thus only accessible to molecules that are of the correct size. Another property of zeolites is the very high internal surface area formed by the channels and cavities (typically hundreds of square meters per gram of zeolite), which is a main asset in catalysis. An example of the structure of one kind of zeolite, called Y-type zeolite, is shown in Fig. 1.

In the present study we focus on Y-type zeolites. They are extensively used in the petrochemical industry for catalytic cracking of hydrocarbons. In a Y-type zeolite the primary building blocks of all zeolites, the tetrahedra, combine to form two secondary building blocks. These are truncated octahedrons with windows consisting of six-membered oxygen rings, the sodalite cages, and hexagonal prisms (see Fig. 2). They are connected in such a way that they leave especially large cavities, the supercages. The supercage of a Y-type zeolite is shown in Fig. 2. The supercage has an approximately

spherical shape with a diameter of 11.8 Å. The entrance to the supercage consists of a ring of twelve oxygen atoms, with a diameter of 7.4 Å.

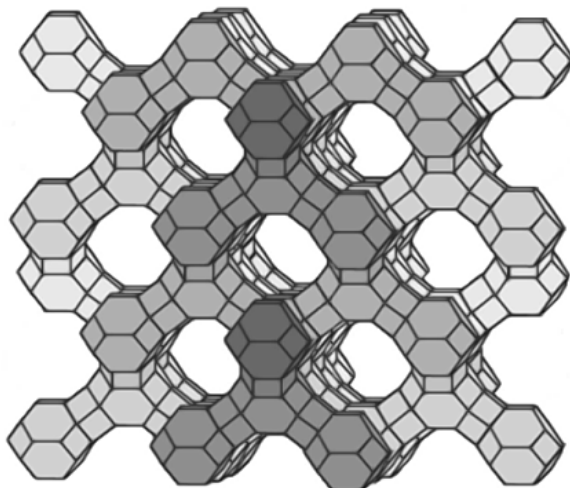


Figure 1 The structure of a Y-type zeolite, showing the channels and cavities. The framework is formed from silicon, aluminium and oxygen atoms. The large cavities are called supercages.

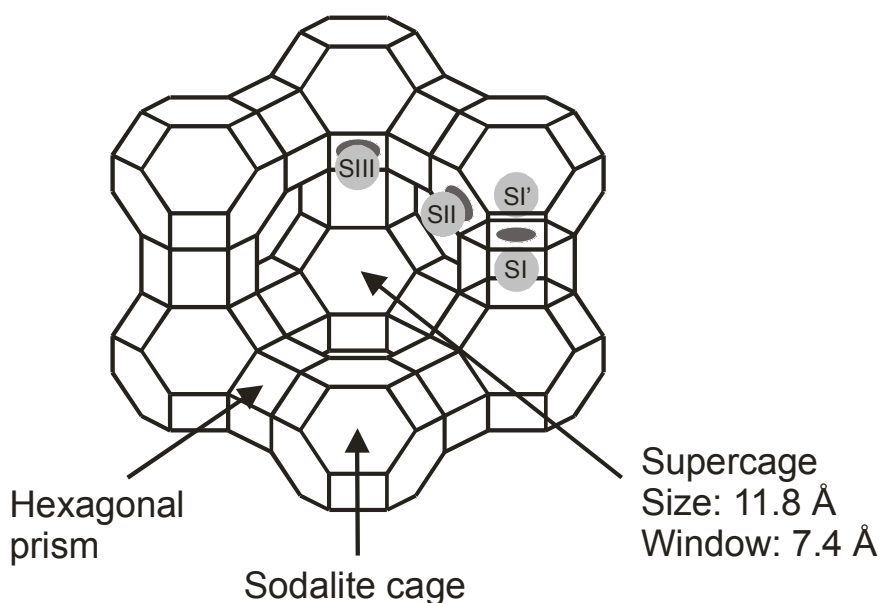


Figure 2 The supercage of a Y-type zeolite. The Si and Al atoms are on the edges and the O atoms on the centres of the solid lines. SI, SI', SII and SIII give the possible cation positions.

The ratio between Si and Al atoms in a zeolite can vary. The trivalence of aluminium causes a net negative charge of the framework. This is compensated for by cations occupying certain extraframework positions. In zeolite Y there are four specific sites the

cations can occupy. They are labeled SI, SI', SII and SIII in Fig. 2. Sites SI and SI' are located within a hexagonal prism and a sodalite cage, respectively. Cations on these sites will not be able to interact with adsorbed molecules in the supercage. Cations on sites SII and SIII, which are located on the surface of the supercage, will be able to do so. The cations can be monovalent like H^+ and Na^+ , but also divalent like Mg^{2+} and Ca^{2+} . It is custom to use the cation in the zeolite name. NaY zeolite thus means a Y-type zeolite containing sodium cations. The general chemical formula of a dehydrated zeolite is $K_{x/n}(AlO_2)_x(SiO_2)_y$, with K a cation of valence n.

In a hydrated zeolite the cations have considerable motional freedom that permits ion exchange. Ion exchange permits the largest volume use of zeolites, which is their use in washing detergents as water softening agents, replacing phosphates. They do this by exchanging the ions they contain for calcium and magnesium ions present in the water, thereby preventing scaling. There are also catalytic applications of ion exchange. Zeolites are excellent supports for catalytically active metals, metal sulfides and metal complexes. To introduce these catalytic centres into the zeolite interior ion exchange is an obvious choice.

The disadvantages of metal incorporation by ion exchange are undesired oxidation states of the ions and their unwanted final locations in the zeolite. The metal ions will, in case of a Y-type zeolite, occupy the SI and SI' sites and not the SII or SIII sites where they are accessible to adsorbed molecules.

An alternative method that overcomes these problems is incorporation of metals by vapour phase insertion of volatile compounds. Here organometallic complexes are vapourised, after which the vapour is absorbed by the zeolite. Metal carbonyls are particularly favoured because they contain metals in a zerovalent oxidation state. Moreover, the carbonyl ligands can be removed under mild conditions after insertion of the compound in the zeolite. This makes the formation of neutral metal clusters possible. Furthermore the compounds are deposited in the supercages only.

In this thesis we study the inclusion of the organometallic compound ferrocene $Fe(C_5H_5)_2$ in zeolite Y. Ferrocene is used to introduce iron in the voids of zeolites. The deposition of small iron particles is of great interest because of their potential use in catalytic processes that involve C-C bond formation, such as the Fischer-Tropsch process.³ A ferrocene molecule consists of an iron atom surrounded on two sides by a cyclopentadienyl C_5H_5 ring (see Fig. 3). This structure of ferrocene was first proposed by Dunitz and Orgel,⁴ who called it 'a molecular sandwich'. The radius of a cyclopentadienyl ring is 2.33 Å, while the distance between the two rings is 3.32 Å. One or two ferrocene molecules will thus fit inside a zeolite Y supercage. Besides its potential application of introducing iron in the zeolite, ferrocene is a relatively simple molecule and ferrocene adsorbed in zeolite can thus be used as a model for zeolites containing more complicated organometallics.

Ferrocene itself is also of catalytic interest. Intermediates of metallocenes such as ferrocene have a potential application in polymer synthesis. Here the relative orientation and dynamics of the metallocene rings determine the stereochemistry of the polymer, with cis- and trans-orientations giving rise to atactic and isotactic polymers, respectively. This could enable the design of polymers on a molecular level.⁵

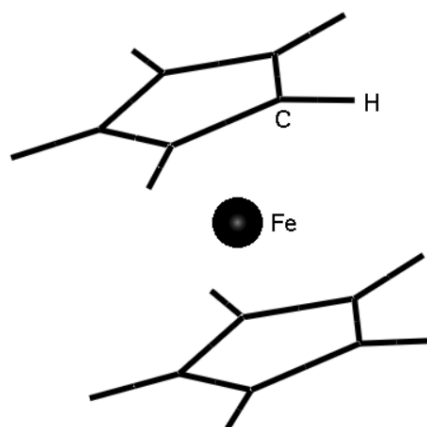


Figure 3 The ferrocene molecule, $\text{Fe}(\text{C}_5\text{H}_5)_2$. It consists of an iron Fe atom sandwiched by two cyclopentadienyl C_5H_5 rings.

The inclusion of ferrocene molecules in the voids of zeolites has been investigated before. One remarkable effect found is that unlike pure ferrocene in the solid or gas-phase state, ferrocene in zeolite Y oxidizes quite easily.^{3,6,7} Ozin et al.⁶ have studied the interaction of ferrocene with both nonacidic NaY zeolite and acidic $\text{H}_n\text{Na}_{56-n}\text{Y}$ zeolites. Dutta et al.⁷ investigated the oxidation of ferrocene to ferrocinium ions in zeolite Y under exposure of oxygen. Suib et al.⁸ have studied ferrocene in the zeolite ZSM-5. Li et al.⁹ made the capability of ferrocene in zeolite Y to transfer electrons the subject of their study. Overweg et al.^{3,10} performed a detailed study of the motion of ferrocene in zeolite Y by means of ^2H and ^{13}C NMR and Mössbauer spectroscopy, in order to get a deeper understanding of the interaction of encaged ferrocene with a zeolite. They particularly focused on the dynamics of ferrocene in Na_{55}Y . At temperatures below 225 K they found that the ferrocene molecules in Na_{55}Y are firmly fixed in the zeolite, their only motional freedom being rapid rotation of the cyclopentadienyl rings about the main ferrocene axis. They suggested that the interaction between the zeolite and the ferrocene molecules takes place via the extraframework Na^+ ions and the aromatic cyclopentadienyl rings, which are slightly negatively charged. Motional reorientations at higher temperatures involve translational processes rather than rotational reorientations. The main translational process was suggested to be intracage rather than cage-to-cage diffusion. From this they derived an activation energy for jumps from SII to SII ion of the ferrocene molecule, being 36.2 and 46.4 kJmol^{-1} for loadings of one and two ferrocene molecules per supercage, respectively. However, due to the timescale of NMR experiments ($\sim\mu\text{s}$) they could not determine the nature of the reorientational motions more precisely. Moreover, the actual location of ferrocene in Na_{55}Y zeolite remained a question.

The motion of ferrocene in zeolite Y has also been studied by Kaiser et al.¹¹ by muon spectroscopy. The comparison with Overweg et al. and with the present study was however hampered by the nature of their technique. The addition of a muon μ^+ adduct

to the ferrocene molecule disturbs the electron system of the ferrocene molecule. This will have effect on any electrostatic interaction between the ferrocene molecule and the zeolite.

It is the scope of this thesis to further illuminate the interaction between ferrocene molecules and the supercages of zeolite Y. For this we give the location of the ferrocene molecules in the supercages and look at the dynamical behaviour of ferrocene molecules locked up in the supercages of zeolite Y. Furthermore, we look into differences between a single ferrocene molecule, solid (crystalline) ferrocene and ferrocene in a zeolite supercage, thus illustrating the influence of a surrounding geometry on an engaged molecule. We focus on two types of zeolites, Na₅₅Y and K₅₅Y. Most of the work presented here is based on work presented elsewhere.

First we introduce, for the interested reader, in chapter 1 the theory behind the main experimental techniques and some models used for the interpretation of the experimental results. This involves inelastic and quasielastic neutron scattering, and models used to interpret the acquired data. We also describe two techniques used to model molecules in zeolites, density functional theory and a topological analysis of the electron density. In chapter 2 we give the results of neutron and X-ray powder diffraction on ferrocene Fe(C₅H₅)₂ in Na₅₅Y zeolite, and show the preferred location of ferrocene for loadings of one and two ferrocene molecules per zeolite supercage. Next, in chapter 3 we analyse the interaction between a ferrocene molecule and the zeolite by performing a topological analysis of the electron density. Chapter 4 gives the results of quasielastic neutron scattering on ferrocene in KY zeolite. Here we look into the reorientational motions of the cyclopentadienyl rings of a ferrocene molecule inside a Y-type zeolite. Chapter 5 gives the results of inelastic neutron scattering on solid ferrocene. This technique probes the internal vibrations in the ferrocene molecules. We also model the spectra with *ab-initio* density functional theory. In chapter 6 we discuss inelastic neutron scattering on the internal vibrations in ferrocene in a Y-type zeolite. We will compare these with those of solid ferrocene and with density functional theory. In chapter 7 we study the vibrational modes of the ferrocene molecules as a whole with respect to zeolite Y framework. We calculate the frequencies of these modes with density functional theory. Next we give a summary of this thesis and state some general conclusions. Finally we give some additional information. In appendix A we present a new way to obtain the Elastic Incoherent Structure Factor from quasielastic neutron scattering experiments. In appendix B we discuss TFXA and TOSCA, two of the neutron spectrometers used in this thesis.

References

1. G. Ertl & H-J. Freund, *Physics Today* January 1999, 32
2. A.F. Cronstedt, *Kongl. Vetenskaps Acad. Handl. Stockholm* **18** (1756) 120
3. A.R. Overweg, *The Preparation, Modification and Characterization of Some Molecular Sieve Materials* (Eindhoven, 1998) ISBN 90-386-0820-9
4. J.D. Dunitz & L.E. Orgel, *Nature* **171** (1953) 121
5. F. Ciardelli, A. Altomare & M. Michelotti, *Catalysis Today* **41** (1998) 149
6. G.A. Ozin & J. Godber, *J. Phys. Chem.* **93** (1989) 878
7. P.K. Dutta & M.A. Thomsom, *Chem. Phys. Lett.* **131** (1986) 435

8. S.L. Suib, K.C. MacMahon & D. Psaras, *Intrazeolite Chemistry*, Eds. G.D. Stucky & F.G. Dwyer, *Am. Chem. Soc. Symp. Ser.* **131** (1986) 301
9. X. Li & T.E. Mallouk, *J. Phys. Chem.* **91** (1987) 643
10. A.R. Overweg, H. Koller, J.W. de Haan, L.J.M. van de Ven, A.M. van der Kraan & R.A. van Santen, *J. Phys. Chem. B* **103** (1999) 4298
11. C.T. Kaiser, P.C.M. Gubbens, E. Kemner, A.R. Overweg & U.A. Jayasooriya, *In preparation*

Chapter 1. Theory

1.1.1 Introduction to neutron scattering

Neutron scattering plays an important role in the study of statics and dynamics in condensed matter physics. This stems from a number of favourable properties of neutrons compared to other particles used in spectroscopic techniques like electrons and photons. On the one hand thermal neutrons, which are commonly used in neutron scattering, have a wavelength that is of the order of magnitude of inter-atomic distances, rendering a study of the structure of the sample under investigation possible. On the other hand the energy of thermal neutrons is of the same order as the energy of molecular motions such as translations, rotations and vibrations. This makes it possible to study the dynamics of the sample at the same time. For photons and electrons this is not the case and the experimentalist must choose to either study the structure or the dynamics. Furthermore neutrons are neutral particles and interact weakly with matter. This enables a study inside bulk material. Since neutrons interact directly with the nuclei, a study of molecular rotations and vibrations is especially attractive because there are no selection rules involved, so in principle neutrons can map all rotational and vibrational transitions.

1.1.2 Basics of neutron scattering

In inelastic neutron scattering a neutron exchanges energy and momentum with the sample under study. This is schematically shown in Fig. 1.1. The incoming neutron has an initial momentum $\hbar\mathbf{q}_i$ and an initial energy $E_i = \hbar^2\mathbf{q}_i^2/2m_n$, m_n being the mass of a neutron. The scattered neutron has a final momentum $\hbar\mathbf{q}_f$ and final energy E_f .

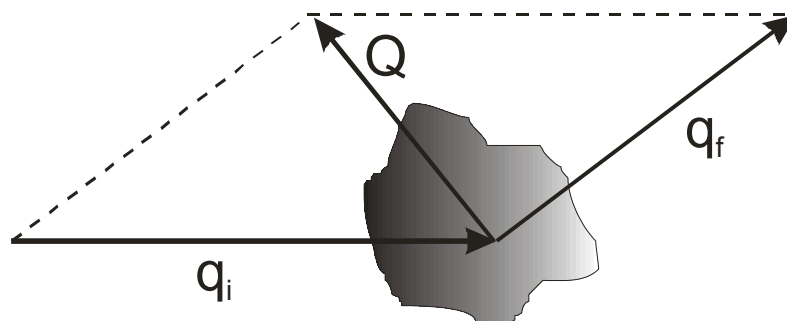


Figure 1.1 The scattering of a neutron with incident wavevector \mathbf{q}_i by a sample. The sample transfers momentum \mathbf{Q} to the neutron, which obtains a wavevector \mathbf{q}_f .

From the laws of conservation of momentum and energy we obtain the momentum transfer $\hbar\mathbf{Q}$ from the sample to the neutron,

$$\hbar\mathbf{Q} = \hbar(\mathbf{q}_f - \mathbf{q}_i) \quad (1.1)$$

and the energy transfer $\hbar\omega$ from the sample to the neutron,

$$\hbar\omega = E_f - E_i = \frac{\hbar^2}{2m_n}(q_f^2 - q_i^2) \quad (1.2)$$

We construct a combined initial state of neutron and sample $|n_i, q_i\rangle$ with the sample labeled n , and the neutron labeled q (we neglect the neutron spin, which will not be used in this thesis). Let $|n_f, q_f\rangle$ represent the final state. We describe the incoming neutron by a plane wave, and the scattered by a spherical wave. The probability $W_{i \rightarrow f}$ of a transition between $|n_i, q_i\rangle$ and $|n_f, q_f\rangle$ is given in first order perturbation theory by Fermi's golden rule,¹

$$W_{i \rightarrow f} = \frac{2\pi}{\hbar} \left| \langle n_f, q_f | \hat{V}(\mathbf{r}) | n_i, q_i \rangle \right|^2 \rho_{k_f}(E_f) \delta(\hbar\omega - E(n_i) + E(n_f)) \quad (1.3)$$

with $\rho_{k_f}(E_f)$ the density of the final states of the neutron and $V(\mathbf{r})$ the interaction potential. The δ -function reflects conservation of energy. In a scattering experiment one studies the distribution of the scattered neutrons as a function of their energy and their direction with respect to the incoming neutron beam. For $\rho_{k_f}(E_f)$ per volume element for neutrons in a solid angle $d\Omega$ and with an energy between E_f and $E_f + dE_f$ we can write

$$\rho_{k_f}(E_f) dE_f = \frac{d\mathbf{k}_f}{(2\pi)^3} = \frac{1}{(2\pi)^3} k_f^2 dk_f d\Omega \quad (1.4)$$

Because the probability of a scattering event is small, the intensity I of the scattered neutrons is proportional to the flux of incoming neutrons $\Phi(E_i)$ (this is called a linear response approximation). This proportionality is given by the double differential cross section

$$\frac{d^2\sigma}{d\Omega d\omega} = \frac{I}{\Phi(E_i) d\Omega d\omega} \quad (1.5)$$

The flux per unit area of the incoming neutrons per solid angle is given by their velocity $\hbar\mathbf{k}_i / m_n$. One obtains the intensity by summing the probabilities of transition between two states over all allowed final states, and averaging over all initial states weighted with a probability $p(n_i)$. The double differential cross section then reads

$$\frac{d^2\sigma}{d\Omega d\omega} = \frac{q_f}{q_i} \left(\frac{m_n}{2\pi\hbar^2} \right)^2 \sum_{n_i} p(n_i) \sum_{n_f} \left| \langle n_f, q_f | V(\mathbf{r}) | n_i, q_i \rangle \right|^2 \delta(\hbar\omega - E(n_i) + E(n_f)) \quad (1.6)$$

For the interaction potential usually the Fermi pseudo-potential is introduced,

$$V(\mathbf{r}) = \frac{2\pi\hbar^2}{m_n} \sum_j b_j \delta(\mathbf{r} - \mathbf{r}_j) \quad (1.7)$$

where \mathbf{r}_j is the position of nucleus j and b_j its scattering length. The scattering length depends on the relative orientation of the spin of the scatterer with respect to the spin of the neutron. One nucleus can thus scatter with two different scattering lengths. We then write the interaction potential as a Heisenberg operator

$$V(\mathbf{r}, t) = \exp\left(\frac{iHt}{\hbar}\right) V(\mathbf{r}) \exp\left(\frac{-iHt}{\hbar}\right) \quad (1.8)$$

with H the Hamiltonian of the system. By using an integral representation for the δ -function we finally obtain for the double differential cross section

$$\frac{d^2\sigma}{d\Omega d\omega} = \frac{q_f}{q_i} \frac{1}{2\pi} \int_{-\infty}^{+\infty} dt \exp(-i\omega t) \sum_{j,k} \langle b_j b_k \rangle \langle \exp(-i\mathbf{Q} \cdot \mathbf{r}_j(0)) \exp(i\mathbf{Q} \cdot \mathbf{r}_k(t)) \rangle_T \quad (1.9)$$

where $\langle \dots \rangle_T$ denotes a thermal ensemble average. The averaging over the product of the scattering lengths of the different nuclei in the sample can be written as a sum of a mean scattering length and the deviations from this mean scattering length, due to a random distribution of the nuclei and their random spin distribution:

$$\langle b_j b_k \rangle = \langle b_j \rangle \langle b_k \rangle + \delta_{jk} \left\{ \langle b_j^2 \rangle - \langle b_j \rangle \langle b_k \rangle \right\} = b_{coh}^2 + \delta_{jk} b_{inc}^2 \quad (1.10)$$

The first term gives the interference of the neutron with several nuclei, resulting in coherent scattering. The second term represents incoherent scattering that describes the interaction of a neutron with exactly one nucleus. The scattering lengths vary greatly with the various elements, in a non-systematic way. This is in contrast with X-ray scattering, in which the scattering amplitude is highly dependent on the number of electrons in the scattering nucleus, so heavy atoms scatter more than light atoms and hydrogen is nearly 'invisible'. With neutron scattering it is possible that light atoms scatter more than heavy atoms, making neutron scattering complementary to X-ray scattering. This is especially true for hydrogen atoms, which have a very large incoherent scattering cross sections compared to other elements ($80.2 \cdot 10^{-28} \text{ m}^2$ compared with typically $1 \text{ to } 5 \cdot 10^{-28} \text{ m}^2$).²

Strictly spoken Fermi's golden rule can not be applied to the scattering of thermal neutrons, since the interaction is between a neutron and a nucleus is actually very strong. Fermi's pseudo-potential doesn't resemble the real potential for a neutron in vicinity of a nucleus. However, in practice the combination of the two works well, since the pseudo-potential is constructed to yield the correct results for isotropic scattering when used in combination with the golden rule.

In Eq. (1.9) for the double differential cross section the properties of the neutron and the scatterer appear separated. It is therefore convenient to introduce the dynamic structure factor $S(\mathbf{Q},\omega)$ that describes the dynamical behaviour of the scatterer only, not the behaviour of the neutron. Keeping the distinction between coherent and incoherent scattering in mind, Eq. (1.9) can then be written as

$$\frac{d^2\sigma}{d\Omega d\omega} = N \frac{q_f}{q_i} \{b_{coh}^2 S_{coh}(\mathbf{Q},\omega) + b_{inc}^2 S_{inc}(\mathbf{Q},\omega)\} \quad (1.11)$$

with the coherent and incoherent dynamic structure factors $S_{coh}(\mathbf{Q},\omega)$ and $S_{inc}(\mathbf{Q},\omega)$ defined as

$$S_{coh}(\mathbf{Q},\omega) \equiv \frac{1}{2\pi} \int_{-\infty}^{+\infty} dt \exp(-i\omega t) \frac{1}{N} \sum_{j,k} \langle \exp(-i\mathbf{Q} \cdot \mathbf{r}_j(0)) \exp(i\mathbf{Q} \cdot \mathbf{r}_k(t)) \rangle \quad (1.12)$$

$$S_{inc}(\mathbf{Q},\omega) \equiv \frac{1}{2\pi} \int_{-\infty}^{+\infty} dt \exp(-i\omega t) \frac{1}{N} \sum_j \langle \exp(-i\mathbf{Q} \cdot \mathbf{r}_j(0)) \exp(i\mathbf{Q} \cdot \mathbf{r}_j(t)) \rangle \quad (1.13)$$

The relative magnitudes of $S_{coh}(\mathbf{Q},\omega)$ and $S_{inc}(\mathbf{Q},\omega)$ depend on the nature of the scatterer. It is important to realize that $S_{coh}(\mathbf{Q},\omega)$ reflects collective atomic motions, while $S_{inc}(\mathbf{Q},\omega)$ provides information on the motion of an individual atom. Due to the nature of our sample, ferrocene $\text{Fe}(\text{C}_5\text{H}_5)_2$ in NaY zeolite consisting of Na, Si, Al and O atoms an inelastic neutron scattering experiment will in our case mainly probe the individual motions of the hydrogen atoms of the ferrocene molecules in the zeolite. In general the high incoherent scattering length of hydrogen makes inelastic neutron scattering an extremely powerful tool to study the dynamics of adsorbed molecules containing hydrogen atoms in a zeolite host. In the remainder of this chapter we will therefore focus on the incoherent dynamic structure factor. It is useful to introduce the time Fourier transform of $S_{inc}(\mathbf{Q},\omega)$, the incoherent intermediate scattering function, $I_{inc}(\mathbf{Q},t)$,

$$I_{inc}(\mathbf{Q},t) \equiv \int_{-\infty}^{+\infty} d\omega \exp(i\omega t) S_{inc}(\mathbf{Q},\omega) = \frac{1}{N} \sum_i \langle \exp(-i\mathbf{Q} \cdot \mathbf{r}_i(0)) \exp(i\mathbf{Q} \cdot \mathbf{r}_i(t)) \rangle \quad (1.14)$$

$I_{\text{inc}}(\mathbf{Q}, t)$ describes the decay in time of a single particle density fluctuation. It is this function that often acts as a starting point for the development of models to describe the dynamics of a system. By calculating the intermediate scattering function for a certain model of the time development of $\mathbf{r}_j(t)$ and taking the Fourier transform, one has a theoretical function for $S(\mathbf{Q}, \omega)$ that is directly comparable with the measured $S(\mathbf{Q}, \omega)$.

The motion of an atom in a molecule is a superposition of several different kind of motions. The atom takes part in any translation or rotation of the whole molecule. These can be stochastic, diffusional processes where the molecule performs a random motion. The molecule can also vibrate as a whole, for example due to phonons. It can also vibrate when it is trapped in a potential well. This is the case with hindered rotations (which are sometimes called librations). An atom in a molecule will also vibrate around its equilibrium position in the molecule and this is called an intramolecular vibration. The observed energy transfers associated with random processes such as translational or rotational diffusion are usually of the order of a few μeV to a few meV , and they give rise to a spectral broadening in $S(\mathbf{Q}, \omega)$ around zero energy transfer. This kind of scattering is usually called quasielastic scattering (although formally it is still inelastic scattering, since it involves non-zero energy transfers). The energies associated with phonons and librations are usually of the order of some meV , and give rise to inelastic peaks in $S(\mathbf{Q}, \omega)$ away from zero energy transfer. Intramolecular vibrations occur at still higher energies, of the order of some meV to eV . It is these latter two types of scattering that is normally called inelastic scattering. We show a generalized neutron scattering spectrum as a function of energy transfer in Fig. 1.2, pointing out the different kind of motions. In practice all peaks in the spectrum are broadened with the resolution of the spectrometer.

We write for the position vector $\mathbf{r}(t)$ of a scattering atom in a molecule

$$\mathbf{r}(t) = \mathbf{r}_T(t) + \mathbf{r}_R(t) + \mathbf{u}(t) \quad (1.15)$$

where $\mathbf{r}_T(t)$ is the translational component due to translations of the whole molecule, $\mathbf{r}_R(t)$ the rotational component due to rotations of the whole molecule and $\mathbf{u}(t)$ the displacement of the atom from its equilibrium position in the molecule. An exact calculation of $I_{\text{inc}}(\mathbf{Q}, t)$ taking all motions into account is notoriously difficult. Normally the different motions are treated independently, assuming the different kind of motions do not influence each other. Intramolecular vibrations occur on a much faster time scale (and thus energy scale) than translations and rotations and it is reasonable to assume that they are not much effected by them. The assumption that translations and rotations of the molecule are not coupled might not always be the case, for example in the case of cooperative rotations.

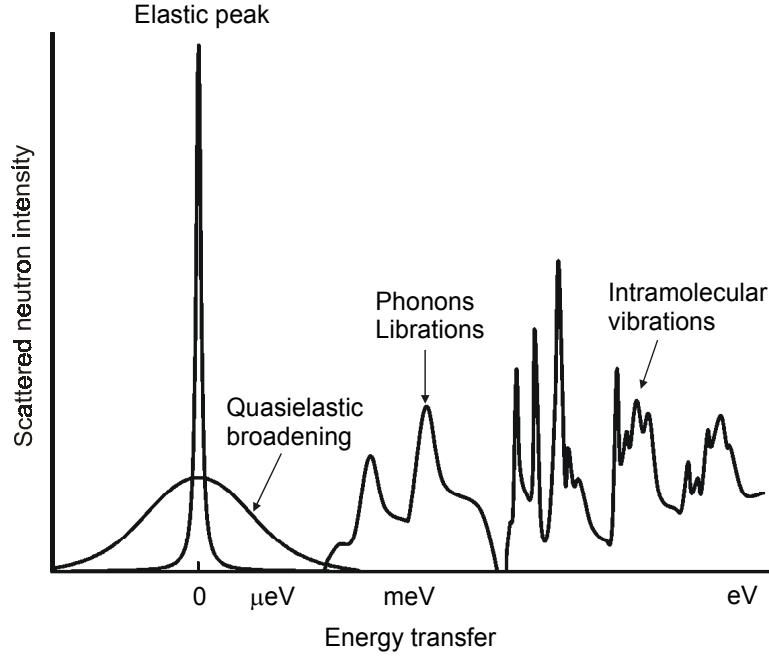


Figure 1.2 Generalized neutron scattering spectrum for a molecule as a function of energy transfer.

Taking the different types of motions as independent $I_{inc}(\mathbf{Q}, t)$ can be factorized as

$$I_{inc}(\mathbf{Q}, t) = I_{inc}^T(\mathbf{Q}, t) \cdot I_{inc}^R(\mathbf{Q}, t) \cdot I_{inc}^V(\mathbf{Q}, t) \quad (1.16)$$

with $I_{inc}^T(\mathbf{Q}, t)$, $I_{inc}^R(\mathbf{Q}, t)$ and $I_{inc}^V(\mathbf{Q}, t)$ the intermediate incoherent scattering functions for translations, rotations and vibrations, respectively. When looking at translations and rotations the vibrational part of the scattering function is usually written as a Debye-Waller factor, $\exp(-\langle \mathbf{u}^2 \rangle Q^2)$, with $\langle \mathbf{u}^2 \rangle$ the mean-square displacement of the atom.

1.1.3 Quasielastic neutron scattering

In the remainder of this chapter we will focus on the dynamical behaviour of one hydrogen atom, so $N = 1$ in Eq. (1.14) and we use for simplicity $I(\mathbf{Q}, t) = I_{inc}(\mathbf{Q}, t)$. First we discuss $I(\mathbf{Q}, t)$ for diffusional processes. We write $I(\mathbf{Q}, t)$ more explicitly,

$$I(\mathbf{Q}, t) = \int d\mathbf{r} \int d\mathbf{r}' P^{eq}(\mathbf{r}) P(\mathbf{r}, 0 | \mathbf{r}', t) \exp(i\mathbf{Q} \cdot (\mathbf{r}' - \mathbf{r})) \quad (1.17)$$

where $P^{eq}(\mathbf{r})$ is the equilibrium distribution of one hydrogen atom H and $P(\mathbf{r}, 0|\mathbf{r}', t)$ is the conditional probability of finding H at \mathbf{r}' at time t when it was at \mathbf{r} at time $t=0$. The probabilities are normalized,

$$\int d\mathbf{r} P^{eq}(\mathbf{r}) = 1 \quad (1.18)$$

$$\int d\mathbf{r}' P(\mathbf{r}, 0|\mathbf{r}', t) = 1 \quad (1.19)$$

for all \mathbf{r} and all t . The boundary conditions are

$$\lim_{t \rightarrow 0} P(\mathbf{r}, 0|\mathbf{r}', t) = \delta(\mathbf{r} - \mathbf{r}') \quad (1.20)$$

$$\lim_{t \rightarrow \infty} P(\mathbf{r}, 0|\mathbf{r}', t) = P^{eq}(\mathbf{r}') \quad (1.21)$$

From the second boundary condition, which is due to the ergodic theorem, it follows directly that

$$\lim_{t \rightarrow \infty} I(\mathbf{Q}, t) = \left| \int d\mathbf{r} P^{eq}(\mathbf{r}) \exp(i\mathbf{Q} \cdot \mathbf{r}) \right|^2 \equiv A_0(\mathbf{Q}) \quad (1.22)$$

so that we can rewrite Eq. (1.17) as

$$I(\mathbf{Q}, t) = A_0(\mathbf{Q}) + \{1 - A_0(\mathbf{Q})\} \Delta I(\mathbf{Q}, t) \quad (1.23)$$

with $\lim_{t \rightarrow 0} \Delta I(\mathbf{Q}, t) = 1$ and $\lim_{t \rightarrow \infty} I(\mathbf{Q}, t) = 0$. This yields for the dynamic structure factor

$$S(\mathbf{Q}, \omega) = A_0(\mathbf{Q}) \delta(\omega) + \{1 - A_0(\mathbf{Q})\} \Delta S(\mathbf{Q}, \omega) \quad (1.24)$$

We see that there is a basic separation in $S(\mathbf{Q}, \omega)$. It consists of a δ -function at zero energy transfer, the elastic peak, whose amplitude $A_0(\mathbf{Q})$ gives the equilibrium distribution of the H atom, while the remaining spectrum $\Delta S(\mathbf{Q}, \omega)$ determines the dynamics of the H atom. $A_0(\mathbf{Q})$ is usually called the Elastic Incoherent Structure Factor or EISF. From Eq. (1.24) we obtain $\lim_{\mathbf{Q} \rightarrow 0} A_0(\mathbf{Q}) = 1$, for zero momentum transfer there is only an elastic peak in $S(\mathbf{Q}, \omega)$.

An illustrative example for the equilibrium distribution is the case of a finite number N of fixed sites located at \mathbf{r}_j , each with equal probability $1/N$,

$$P^{eq}(\mathbf{r}) = \sum_{j=1}^n \frac{1}{N} \delta(\mathbf{r} - \mathbf{r}_j) \quad (1.25)$$

From Eqs. (1.22) and (1.25) it follows that in this case $\lim_{Q \rightarrow \infty} A_0(\mathbf{Q}) = \frac{1}{N}$. One can thus, from experiment, directly deduce the number of sites where the H atom can be. If the number of sites is infinite, i.e. there is a continuous motion, such as diffusion, $A_0(\mathbf{Q})$ approaches zero for large Q . On the other hand, if the limit of $A_0(\mathbf{Q})$ is finite, there exist a limited number of sites the H-atom can occupy, and we have a motion restricted in space. For intermediate \mathbf{Q} , the behaviour of $A_0(\mathbf{Q})$ is dependent on the direction of \mathbf{Q} , $\hat{\mathbf{Q}}$. From experiment we obtain the angular average of $A_0(\mathbf{Q})$, thus in our model we must also average over all $\hat{\mathbf{Q}}$. This gives

$$A_0(Q) = \frac{1}{N^2} \sum_{j=1}^N \sum_{j'=1}^N j_0(Q|\mathbf{r}_j - \mathbf{r}_{j'}|) \quad (1.26)$$

where $j_0(x)$ is the zeroth-order Bessel function.

In general we can expand $A_0(\mathbf{Q})$ in powers of \mathbf{Q} , which yields

$$A_0(\mathbf{Q}) = 1 - Q^2 \int d\mathbf{s} P^{eq}(\mathbf{s}) (\hat{\mathbf{Q}} \cdot \mathbf{s})^2 + O(Q^4) \quad (1.27)$$

with \mathbf{R}^{eq} the equilibrium position in space of the probability distribution and $\mathbf{s} = \mathbf{r} - \mathbf{R}^{eq}$ the deviation from this position defined such that $\int d\mathbf{s} P^{eq}(\mathbf{s}) \mathbf{s} = 0$. The angular average gives, using $\langle (\mathbf{Q} \cdot \mathbf{s})^2 \rangle_{\hat{\mathbf{Q}}} = \frac{1}{3} Q^2 s^2$,

$$A_0(Q) = 1 - \frac{1}{3} Q^2 \int d\mathbf{s} P^{eq}(\mathbf{s}) s^2 + O(Q^4) \quad (1.28)$$

We thus have a radius, $R_G = \sqrt{\int d\mathbf{s} P^{eq}(\mathbf{s}) s^2}$, commonly called Guinier radius, that gives us information about the possible deviations from the ‘centre of mass’ of the probability distribution and hence about the area that is accessible to the H atom, and which we can get from experiment from the low Q behaviour of $A_0(Q)$. If only a restricted area of space is accessible to H, R_G will be the radius of this area.

The relaxation of $P(\mathbf{r}, 0 | \mathbf{r}', t)$ is described by a Liouville-like operator $\mathcal{L}(\mathbf{r}')$

$$\frac{\partial}{\partial t} P(\mathbf{r}, 0 | \mathbf{r}', t) = \mathcal{L}(\mathbf{r}') P(\mathbf{r}, 0 | \mathbf{r}', t) \quad (1.29)$$

Above equation closely resembles the Schrödinger equation in quantum mechanics that describes the evolution of wavefunction $\psi(\mathbf{r},t)$. The Hamiltonian $H(\mathbf{r})$ replaces the operator $\mathcal{L}(\mathbf{r})$, with the extra demand that it must be Hermitian. However, the time as defined above is a real variable, while in quantum mechanics time is complex, making the Schrödinger equation fundamentally different. A solution of Eq. (1.29) is

$$P(\mathbf{r},0|\mathbf{r}',t) = \exp(t\mathcal{L}(\mathbf{r}'))P(\mathbf{r},0|\mathbf{r}',0) = \exp(t\mathcal{L}(\mathbf{r}'))\delta(\mathbf{r}-\mathbf{r}') \quad (1.30)$$

By definition we have $\mathcal{L}(\mathbf{r}')P^{eq}(\mathbf{r}')=0$. For the intermediate scattering function $I(\mathbf{Q},t)$ we obtain

$$\begin{aligned} I(\mathbf{Q},t) &= \int d\mathbf{r} \int d\mathbf{r}' \exp(-i\mathbf{Q}\cdot(\mathbf{r}-\mathbf{r}')) \exp(t\mathcal{L}(\mathbf{r}')) \delta(\mathbf{r}-\mathbf{r}') P^{eq}(\mathbf{r}') \\ &= \int d\mathbf{r} \int d\mathbf{r}' \delta(\mathbf{r}-\mathbf{r}') P^{eq}(\mathbf{r}') \exp(t\mathcal{L}^T(\mathbf{r}')) \exp(-i\mathbf{Q}\cdot(\mathbf{r}-\mathbf{r}')) \\ &= \int d\mathbf{r} P^{eq}(\mathbf{r}) \exp(-i\mathbf{Q}\cdot(\mathbf{r})) \exp(t\mathcal{L}^T(\mathbf{r})) \exp(i\mathbf{Q}\cdot(\mathbf{r})) \\ &= \left\langle \exp(-i\mathbf{Q}\cdot\mathbf{r}) \exp(t\mathcal{L}^T(\mathbf{r})) \exp(i\mathbf{Q}\cdot\mathbf{r}) \right\rangle \end{aligned} \quad (1.31)$$

where \mathcal{L}^T is the transposed operator of \mathcal{L} . Note that this result has the same form as Eq. (1.14) for $I(\mathbf{Q},t)$, $\left\langle \exp(-i\mathbf{Q}\cdot\mathbf{r}(0)) \exp(i\mathbf{Q}\cdot\mathbf{r}(t)) \right\rangle$. However, for diffusional processes in general $\exp(t\mathcal{L}^T(\mathbf{r})) \exp(i\mathbf{Q}\cdot\mathbf{r}) \neq \exp(i\mathbf{Q}\cdot\mathbf{r}(t))$.

1.1.4 Reorientational motions

We will now in more detail treat quasielastic neutron scattering on reorientational motions. With the term reorientational motions we mean rotational motions that are hindered by some potential. In a crystal, or in a zeolite, rotations of a molecule will be affected by its environment. This interaction will result in some preferred orientations for the molecule, which are separated by potential barriers. This hindrance potential will reflect the symmetry of the molecule and of its surroundings. We can distinguish two different situations. If the potential barrier is small compared with the rotational constant of the molecule $\hbar^2/2I$, with I the moment of inertia of the molecule, at sufficient temperature the molecule is normally described by a continuous rotational diffusion, and has no preferred orientation in space. If the potential barrier is large compared with $\hbar^2/2I$, the molecule will be trapped in an orientation. At sufficient temperature it will then oscillate in its potential well. This oscillation is called a librational or torsional motion. If the molecule has enough energy to overcome the potential barrier of the hindrance potential, it can jump to another orientation, where it will oscillate again and so on. We will assume that there is no coupling between the

librations and the rotational jumps, and that the rotational jumps are instantaneous. This means we assume that the average time the molecule spends in a potential well is much larger than the time it takes to reorient itself. We also assume that the jump distance is much larger than the librational amplitude. The reorientational jumps are then described by a random walk process over a finite number of discrete sites, the maxima of the continuous probability function describing the whole potential. The discrete probability function that describes the random walk satisfies a rate equation. With the so obtained discrete probability function we can calculate $I(\mathbf{Q}, t)$ and thus (the measurable) $S(\mathbf{Q}, \omega)$. It is found that the average time between two successive jumps τ as a function of temperature T obeys an Arrhenius law³

$$\tau(T) = \tau_{\infty} \exp(E_a / k_B T) \quad (1.32)$$

where E_a is the activation energy, the difference between the potential well and the libration energy. The pre-exponential factor τ_{∞} is equal to twice the frequency of libration.^{4,5}

We will consider the case of a hydrogen atom H moving along N equivalent sites, equally distributed on a circle with radius R (see Fig. 1.3). The hydrogen atom performs a random walk among these sites.

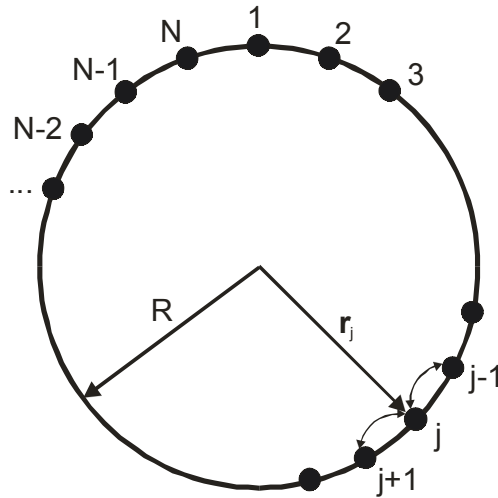


Figure 1.3 Jumps among N equivalent sites, equally distributed on a circle with radius R . Site j has position vector \mathbf{r}_j .

The average time spent by the H-atom on a site between two successive jumps is τ , and jumps are restricted to neighbouring sites only. The probability that the H-atom is at position $\mathbf{r}_j = R \exp\left(\frac{2\pi i j}{N}\right)$ at time t , $P_j(t)$, satisfies the rate equation

$$\frac{d}{dt}P_j(t) = \frac{1}{2\tau} \{P_{j-1}(t) - 2P_j(t) + P_{j+1}(t)\} \quad (1.33)$$

where $P_j(t) = P_{j+N}(t)$. We construct a vector $\mathbf{P}(t)$ whose components are the $P_j(t)$ and a matrix \mathbf{L} that contains the transition rates. We get

$$\frac{d}{dt}\mathbf{P}(t) = \mathbf{L}\mathbf{P}(t) \quad (1.34)$$

with solution

$$\mathbf{P}(t) = \exp(t\mathbf{L})\mathbf{P}(0) \quad (1.35)$$

like Eqs. (1.29) and (1.30). We take $\mathbf{P}_j(0) = \delta_{1,j}$, i.e. at $t = 0$ the H atom is at (the arbitrary) site \mathbf{r}_1 .

We define Λ^ℓ and λ_ℓ ($\ell = 0, \dots, N-1$) to be the eigenvectors and eigenvalues of \mathbf{L} , so that

$$\exp(t\mathbf{L})\Lambda^\ell = \exp(t\lambda_\ell)\Lambda^\ell \quad (1.36)$$

They are given by

$$\lambda_\ell = -\frac{2}{\tau} \sin^2\left(\frac{\pi\ell}{N}\right), \quad \Lambda_j^\ell = \exp\left(2\pi i \frac{\ell j}{N}\right) \quad (1.37)$$

With $\mathbf{P}^{\text{eq}} = \frac{1}{N}\mathbf{1}$ we obtain

$$\begin{aligned} I(\mathbf{Q}, t) &= \frac{1}{N} \sum_{j,j'=1}^N \exp(i\mathbf{Q} \cdot (\mathbf{r}_j - \mathbf{r}_{j'})) \mathbf{P}(t) = \frac{1}{N} \sum_{j,j'=1}^N \exp(i\mathbf{Q} \cdot (\mathbf{r}_j - \mathbf{r}_{j'})) \exp(t\mathbf{L})\mathbf{P}(0) \\ &= \frac{1}{N} \exp(-i\mathbf{Q} \cdot \mathbf{r}_1) \exp(t\mathbf{L}^T) \exp(i\mathbf{Q} \cdot \mathbf{r}_1) \\ &= \frac{1}{N} \sum_{\ell=0}^{N-1} \sum_{j=1}^N \exp(\lambda_\ell t) \Lambda_j^\ell \exp(i\mathbf{Q} \cdot (\mathbf{r}_j - \mathbf{r}_1)) = \sum_{\ell=0}^{N-1} \exp(\lambda_\ell t) A_\ell(\mathbf{Q}) \end{aligned} \quad (1.38)$$

The resulting expression for $S(\mathbf{Q}, \omega)$, averaged over $\hat{\mathbf{Q}}$, is

$$S(\mathbf{Q}, \omega) = A_0(\mathbf{Q})\delta(\omega) + \sum_{\ell=1}^{N-1} A_\ell(\mathbf{Q}) \frac{1}{\pi} \frac{|\lambda_\ell|}{\omega^2 + \lambda_\ell^2} \quad (1.39)$$

The dynamic structure factor thus consists of a central δ -function and $N-1$ Lorentzians, centered on zero energy transfer, the quasielastic broadening. The amplitudes $A_\ell(Q)$ are given by³

$$A_\ell(Q) = \frac{1}{N} \sum_{j=1}^N j_0(Q|\mathbf{r}_j - \mathbf{r}_1|) \cos\left(\frac{2\pi\ell j}{N}\right) \quad (1.40)$$

In Fig. 1.4 we plot $A_0(Q)$ for some values of N , showing the dependence of the EISF on the geometry of the motion.

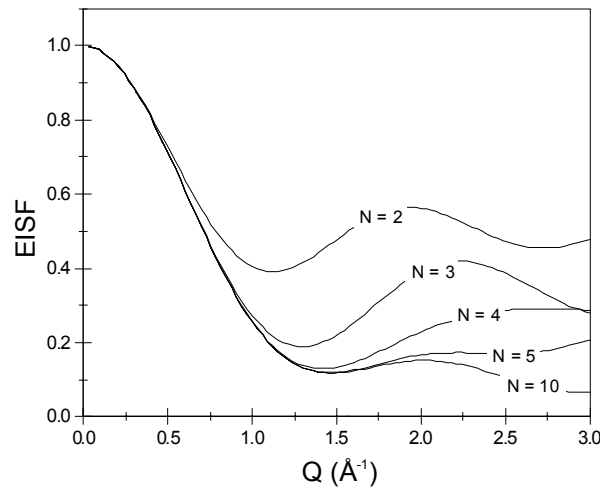


Figure 1.4 The amplitude of the central line $A_0(Q)$ or Elastic Incoherent Structure Factor (EISF) for a jump model for N equivalent sites on a circle for different values of N .

The widths of the Lorentzians λ_ℓ are equal to the absolute value of the eigenvalues of the operator \mathbf{L} (see Eq. (1.37)) and depend on τ . We see that the quasielastic broadening indeed contains the information on the dynamics of the motion. The above discussed jump model, with $N=5$, has been successfully applied to reorientational motions of the metallocenes nickelocene, ruthenocene and ferrocene measured with neutron scattering.^{6,7}

1.1.5 Intramolecular vibrations

When an atom performs a vibrational motion this vibration is commonly described by a harmonic oscillator. We will therefore first discuss the case of one atom performing a harmonic oscillation. Since inelastic neutron experiments on intramolecular vibrations are normally done at very low temperature, so that the energy transfer $\hbar\omega$ is of the order of $k_B T$, a classical approach as above will not suffice. We therefore start from the Schrödinger equation for a one-dimensional harmonic oscillator,

$$H\psi(\mathbf{r}) = \left(\frac{-\hbar^2}{2m} \nabla^2 + \frac{1}{2} m \omega_0^2 r^2 \right) \psi(\mathbf{r}) = E\psi(\mathbf{r}) \quad (1.41)$$

where the Hamiltonian H has the well known eigenvalues $E_n = \hbar\omega_0(n + \frac{1}{2})$, with ω_0 the frequency of vibration and m the mass of the atom. From above equation one can obtain $\mathbf{r}(t)$. Eq. (1.14) becomes after some mathematics¹

$$I(\mathbf{Q}, t) = \exp(-2W(\mathbf{Q})) \exp(y \cosh(x)) \quad (1.42)$$

with

$$x = \omega_0 \left(it + \frac{1}{2} \hbar\beta \right), \quad y = \frac{\hbar(\mathbf{Q} \cdot \mathbf{e})^2}{2m\omega_0 \sinh(\frac{1}{2} \hbar\omega_0\beta)} \quad (1.43)$$

with $\beta = \frac{1}{k_B T}$ and \mathbf{e} the unit vector in the direction of the oscillation. The Debye-Waller factor $\exp(-2W(\mathbf{Q}))$ is obtained with

$$2W(\mathbf{Q}) = \frac{\hbar(\mathbf{Q} \cdot \mathbf{e})^2}{2m\omega_0} \coth(\frac{1}{2} \hbar\omega_0\beta) \quad (1.44)$$

For $S(\mathbf{Q}, \omega)$ we obtain, using $\exp(y \cosh(x)) = \sum_{n=-\infty}^{\infty} \exp(nx) I_n(y)$ with n an integer and $I_n(y)$ a Bessel function of the first kind,¹

$$S(\mathbf{Q}, \omega) = \exp(-2W(\mathbf{Q}) + \frac{1}{2} \hbar\omega\beta) \sum_{n=-\infty}^{\infty} I_n(y) \delta(\hbar\omega - n\hbar\omega_0) \quad (1.45)$$

This is the exact solution for $S(\mathbf{Q}, \omega)$ for a harmonic oscillator. $S(\mathbf{Q}, \omega)$ consists of an elastic peak, two peaks originating from the vibrational frequency at $\omega = \pm\omega_0$ and an infinite number of overtones. We find $\lim_{t \rightarrow \infty} I(\mathbf{Q}, t) = \exp(-2W(\mathbf{Q}))$, while the amplitude of the elastic peak in Eq. (1.45) equals $I_0(y) \exp(-2W(\mathbf{Q}))$. This discrepancy (see Eq. (1.22)) stems from the fact that the long-time behaviour of $I(\mathbf{Q}, t)$ is only valid for an ensemble average. If one takes N harmonic oscillators with $N \rightarrow \infty$, it can be shown that the amplitude of the elastic line equals the Debye-Waller factor.¹

If $\frac{\hbar(\mathbf{Q} \cdot \mathbf{e})^2}{m\omega_0} \ll 1$ Eq. (1.45) can be simplified to

$$S(\mathbf{Q}, \omega) = \exp(-2W(\mathbf{Q})) \cdot \left\{ \delta(\omega) + \frac{\hbar(\mathbf{Q} \cdot \mathbf{e})^2}{2m\omega_0} (1 + n(\omega)) (\delta(\hbar\omega - \hbar\omega_0) + \delta(\hbar\omega + \hbar\omega_0)) \right\} \quad (1.46)$$

with $n(\omega) = (\exp(\hbar\omega\beta) - 1)^{-1}$. $S(\mathbf{Q}, \omega)$ now consists of an elastic peak and just two inelastic peaks at $\omega = \pm\omega_0$. In the limit $T \rightarrow 0$ Eq. (1.46) can be further simplified to

$$S(\mathbf{Q}, \omega) = \exp\left(-\frac{\hbar(\mathbf{Q} \cdot \mathbf{e})^2}{2m\omega_0}\right) \left\{ \delta(\omega) + \frac{\hbar(\mathbf{Q} \cdot \mathbf{e})^2}{2m\omega_0} \delta(\hbar\omega - \hbar\omega_0) \right\} \quad (1.47)$$

If Q is large above equations are not valid and the overtones contribute significantly to $S(\mathbf{Q}, \omega)$.

A polyatomic molecule containing N atoms constitutes a system with $3N$ degrees of freedom. Three of these degrees of freedom correspond to translations and three others to rotations of the molecule as a whole. This results in $3N-6$ internal degrees of freedom, which lead to $3N-6$ independent vibrational modes in which all atoms can partake. Due to symmetry in the molecule some of these modes can coincide, and it is therefore often useful to introduce unique vibrational modes, normal modes, which can be degenerate.

We first consider the displacement of one atom i , described by $\mathbf{r}_i(t)$. We express $\mathbf{r}_i(t)$ as a sum over the displacements due to the normal modes ν ,

$$\mathbf{r}_i(t) = \sum_{\nu} \mathbf{r}_{i;\nu}(t) \quad (1.48)$$

This yields for the incoherent intermediate scattering function for atom i , $I_i(\mathbf{Q}, t)$,

$$I_i(\mathbf{Q}, t) = \prod_{\nu} I_{i;\nu}(\mathbf{Q}, t) \quad (1.49)$$

where $I_{i;\nu}(\mathbf{Q}, t)$ is the incoherent intermediate scattering function for atom i in mode ν . If we take the vibrations to be harmonic we can take for $I_{i;\nu}(\mathbf{Q}, t)$ the expression for a single harmonic oscillator as described above, replacing \mathbf{e} with the (normalized) amplitude vector $\mathbf{C}_{i;\nu}$ of atom i in mode ν , and m with the mass of atom i , m_i . We get

$$\begin{aligned}
I_i(\mathbf{Q}, t) &= \prod_{\nu} \exp(-2W_{i;\nu}(\mathbf{Q})) \exp(y_{i;\nu} \cosh(x_{\nu})) \\
&= \exp(-2W_i(\mathbf{Q})) \prod_{\nu} \sum_{n_{\nu}=-\infty}^{\infty} \exp(n_{\nu} x_{\nu}) I_{n_{\nu}}(y_{i;\nu})
\end{aligned} \tag{1.50}$$

with

$$x_{\nu} = \omega_{\nu} \left(it + \frac{1}{2} \hbar \beta \right), \quad y_{i;\nu} = \frac{\hbar (\mathbf{Q} \cdot \mathbf{C}_{i;\nu})^2}{2m_i \omega_{\nu} \sinh\left(\frac{1}{2} \hbar \omega_{\nu} \beta\right)} \tag{1.51}$$

and

$$2W_i(\mathbf{Q}) = \sum_{\nu} 2W_{i;\nu}(\mathbf{Q}) = \sum_{\nu} \frac{\hbar (\mathbf{Q} \cdot \mathbf{C}_{i;\nu})^2}{2m_i \omega_{\nu}} \coth\left(\frac{1}{2} \hbar \omega_{\nu} \beta\right) \tag{1.52}$$

The incoherent dynamical structure factor for atom i becomes

$$S_i(\mathbf{Q}, \omega) = \exp(-2W_i(\mathbf{Q}) + \frac{1}{2} \hbar \omega \beta) \sum_{\substack{n_j=-\infty \\ j=1 \dots 3N-6}}^{\infty} \delta\left(\hbar \omega - \sum_{\nu=1}^{3N-6} n_{\nu} \hbar \omega_{\nu}\right) \prod_{\mu=1}^{3N-6} I_{n_{\mu}}(y_{i;\mu}) \tag{1.53}$$

We find the usual formula, as given e.g. by Lovesey,¹ confusing since it involves a product of δ -functions, which is formally not defined.

For N atoms we just have to sum all $S_i(\mathbf{Q}, \omega)$ weighted with the scattering cross section of atom i , σ_i . For large Q many modes contribute to the spectrum, not only the overtones of a mode, but also combinations with other modes. However, for small Q we only get an elastic peak and all ground frequencies at $\omega = \pm \omega_{\nu}$, in analogy with above for the case of one harmonic oscillator. By putting $n_{\nu} = \pm 1$ for the mode of interest and $n_{\nu} = 0$ for all other modes we get for the contribution of normal mode ν to the total $S(\mathbf{Q}, \omega)$ in the limit $T \rightarrow 0$, neglecting the elastic peak,

$$S_{\nu}(\mathbf{Q}, \omega) = \sum_{i=1}^N \sigma_i \exp\left(-\sum_{\nu} \frac{\hbar (\mathbf{Q} \cdot \mathbf{C}_{i;\nu})^2}{2m_i \omega_{\nu}}\right) \left\{ \frac{\hbar (\mathbf{Q} \cdot \mathbf{C}_{i;\nu})^2}{2m_i \omega_{\nu}} \delta(\hbar \omega - \hbar \omega_{\nu}) \right\} \tag{1.54}$$

If the molecule also takes part in external motions, like phonons in a crystal, and if these external motions are independent of the internal motions of the molecule, then the total $S(\mathbf{Q}, \omega)$ will be a convolution of the scattering due to the intramolecular vibrations and the scattering due to the external motions. Each peak of an internal mode will then have

a wing whose shape is determined by the external motions and which can contain much of the original total intensity, I_t , of the intensity of the internal mode, I_i ,⁸

$$I_i = I_t \exp(-Q^2 U_e^2) \quad (1.55)$$

$$I_e = I_t - I_i \quad (1.56)$$

where I_e is the intensity of the wing caused by the external motions and U_e^2 the mean square displacement of the atoms due to the external motions.

We can obtain the frequency ω_v of normal mode v and the amplitude vector $\mathbf{C}_{i,v}$ of atom i in mode v for an isolated molecule in the harmonic approximation as follows.⁹ We write the energy E of the vibrating molecule as

$$E = \frac{1}{2} \sum_{j=1}^{3N} \dot{q}_j^2 + \frac{1}{2} \sum_{j,k=1}^{3N} f_{jk} q_j q_k \quad (1.57)$$

with q_1, \dots, q_{3N} the set of mass weighted displacement coordinates, obtained from the Cartesian displacement coordinates $\Delta x_1, \dots, \Delta z_N$ of the N atoms by

$$q_1 = \sqrt{m_1} \Delta x_1, \quad q_2 = \sqrt{m_1} \Delta y_1, \quad q_3 = \sqrt{m_1} \Delta z_1, \quad q_4 = \sqrt{m_2} \Delta x_2, \quad \dots \quad (1.58)$$

The force constants f_{jk} are given by

$$f_{jk} = \left(\frac{\partial^2 V}{\partial q_j \partial q_k} \right)_{eq} \quad (1.59)$$

where V is the potential energy. A possible solution for q_i is given by

$$q_j = A_j \cos(\sqrt{\lambda} t + \varphi) \quad (1.60)$$

which yields with Newton's equation of motion the following set of differential equations

$$\sum_{j=1}^{3N} (f_{jk} - \delta_{jk} \lambda) A_j = 0, \quad k = 1, \dots, 3N \quad (1.61)$$

The $3N$ values λ_v for λ for which above equation has non-vanishing solutions (i.e. not the trivial solution $A_i = 0$ for all i) are obtained by solving

$$|\mathbf{F} - \lambda \mathbf{E}| = 0 \quad (1.62)$$

with \mathbf{F} the matrix formed by the force constants and \mathbf{E} the unit matrix of dimension $3N$. This gives the frequency ω_v of normal mode v with $\omega_v = \sqrt{\lambda_v}$. In general there will be 6 eigenvalues equal to zero, corresponding to translations and rotations of the molecule as a whole. We write A_{jv} for amplitude A_j in vibrational mode v . It is convenient to normalize these amplitudes,

$$A'_{jv} = \frac{A_{jv}}{\sqrt{\sum_{j,v} (A_{jv})^2}} \quad (1.63)$$

which gives $\sum_{j,v} A'_{jv}{}^2 = 1$. The amplitudes A'_{jv} give the amplitude vectors $\mathbf{C}_{i,v}$ of atom i in mode v . In this thesis we obtain the set of force constants f_{jk} by calculating the second derivative of the potential energy by *ab-initio* density functional theory.

1.2 Density functional theory

There are several methods to calculate the properties of molecules, crystals or surfaces *ab-initio*, i.e. from first principles. In these calculations one separates the motions of the much heavier nuclei from the motions of the electrons (the Born-Oppenheimer approximation)¹⁰. The electrons instantly adjust their positions when the nuclei move. Calculation of the electronic structure is thus separated from the calculation of the motions of the nuclei. In traditional *ab-initio* methods, for a system containing N electrons the wavefunction $\Psi(\mathbf{r}_1, \mathbf{r}_2, \dots, \mathbf{r}_N)$ of all electrons is used to describe the electronic structure. Here \mathbf{r}_i gives the position of electron i . The wavefunction can in principle be obtained by solving the Schrödinger equation exactly. For a system of N interacting electrons and N_{nuc} nuclei the Hamiltonian H of the electrons can be written as the sum of the kinetic energy of the electrons, T , the potential energy of the electrons due to the nuclei, V , and the interaction energy of the electrons, U . The Schrödinger equation becomes

$$\hat{H}\Psi = (\hat{T} + \hat{V} + \hat{U})\Psi = \sum_{i=1}^N \left(-\frac{1}{2} \nabla_i^2 + \sum_{\alpha=1}^{N_{\text{nuc}}} \frac{-Z_{\alpha}}{|\mathbf{R}_{\alpha} - \mathbf{r}_i|} + \frac{1}{2} \sum_{\substack{j=1 \\ j \neq i}}^N \frac{1}{|\mathbf{r}_i - \mathbf{r}_j|} \right) = E\Psi \quad (1.64)$$

where we have used atomic units ($e^2/4\pi\epsilon_0 = \hbar = m_e = 1$, with m_e the mass of an electron), and where Z_{α} and \mathbf{R}_{α} are the atomic number and the position of nucleus α , respectively. Solving this exactly is rarely feasible so one has to make approximations. In practice one often assumes the electrons to be independent, which was first proposed by Hartree.¹¹ One electron does not interact with the other electrons one by one, but

with the average electron density $n(\mathbf{r})$. Mathematically the wavefunction Ψ is split in N one-electron functions ψ ,

$$\Psi(\mathbf{r}_1, \mathbf{r}_2, \dots, \mathbf{r}_N) = \psi_1(\mathbf{r}_1) \psi_2(\mathbf{r}_2) \cdots \psi_N(\mathbf{r}_N) \quad (1.65)$$

with ψ_i the wavefunction of electron i . However, the total electron wavefunction Ψ as written above is not antisymmetric when one interchanges two electrons. Physically it should be and the problem can be solved by taking the total wavefunction as an antisymmetrised sum of all products of the one-electron wavefunctions, which was proposed by Fock and Slater.^{12,13} The total wavefunction can be conveniently written as a determinant (called Slater determinant) and the resulting computational method is called a Hartree-Fock method. Note that if the interaction term U were absent, the Hamiltonian would be a sum of equal one-electron Hamiltonians and the wavefunction would be exactly given by a Slater determinant. In practice one takes the one-electron wavefunctions either numerical or expressed in terms of a set of basis functions. Hartree-Fock methods are commonly used in computational chemistry. They are quite successful in predicting structures and energies. However, for large systems they can be very time-consuming.

An alternative approach is Density Functional Theory (DFT), in which one uses the average electron density $n(\mathbf{r})$ to describe the electronic structure of the system. For a system of N electrons this has the obvious advantage that the electron density is a scalar function of three variables (x, y, z) while the wavefunction Ψ is then a function of $3N$ variables ($4N$ when taking the electron spin into account), making computations much easier for DFT. Density functional theories originate from classical thermodynamics. In classical thermodynamics one normally studies the equilibrium properties of systems, which works well for uniform systems. The properties of non-uniform systems, i.e. systems for which the average density varies in space, are more difficult to predict. It turned out to be very productive to postulate the existence of thermodynamic functions, such as the free energy, for arbitrary values of their arguments, i.e. not necessarily corresponding to the equilibrium conditions. This leads to the concept of functionals of density functions, and to a density functional theory. It can be shown that these functionals reach an extremal value when the density functions are the equilibrium density functions and that the extremal values are the equilibrium values. In thermodynamics this method is often applied to liquids and liquid-vapour interfaces. For electronic structures this approach was followed by Hohenberg and Kohn.¹⁴ They proved the following theorems:

- I. The non-degenerate ground state wavefunction Ψ_0 of a system of N interacting electrons is a functional of the ground state electron density $n_0(\mathbf{r})$: $\Psi_0 = \Psi_0[n_0]$.
- II. There exists an energy functional $E[n]$ of the electron density $n(\mathbf{r})$ that is minimal for the ground state density $n_0(\mathbf{r})$.

According to the second theorem we can thus find $n_0(\mathbf{r})$ by minimizing $E[n]$ by varying $n(\mathbf{r})$ with the constraint $\int n(\mathbf{r}) d\mathbf{r} = N$. In principle one can, according to the first theorem, subsequently calculate any ground state property of the system. The problem in DFT is to find the energy functional. In analogy with Eq. (1.64) we write

$$E[n] = T[n] + V[n] + U[n] \quad (1.66)$$

Unfortunately the kinetic energy functional $T[n]$ is very complicated. However, the kinetic energy can easily be calculated from the wavefunction. Therefore Kohn and Sham proposed another form of the energy functional,¹⁵

$$E[n] = T_{ni}[n] + V[n] + U[n] + E_{xc}[n] \quad (1.67)$$

where $T_{ni}[n]$ is the kinetic energy of a fictitious system of non-interacting electrons in such an effective potential $v_{eff}[n](\mathbf{r})$ that $n(\mathbf{r})$ is the same as that of the system of interacting electrons, where $v_{eff}[n](\mathbf{r})$ is a functional of the electron density. It is assumed that such a $v_{eff}[n](\mathbf{r})$ exists, and this assumption is believed to be correct for realistic systems. For the potential energy functional $V[n]$ and the interaction energy functional $U[n]$ we have

$$V[n] = \sum_{\alpha=1}^{N_{nuc}} \int \frac{-Z_{\alpha} n(\mathbf{r})}{|\mathbf{R}_{\alpha} - \mathbf{r}|} d\mathbf{r} \quad (1.68)$$

$$U[n] = \int \int \frac{n(\mathbf{r})n(\mathbf{r}')}{|\mathbf{r} - \mathbf{r}'|} d\mathbf{r}d\mathbf{r}' \quad (1.69)$$

Note that the interaction energy also contains self-interaction. The last term, $E_{xc}[n]$ is called the exchange-correlation energy functional and contains all energy terms not accounted for in the other three terms. These are electron exchange, the electron correlation, a correction on the kinetic energy and a correction for the self-interaction.

Since the interaction term between the electrons is now absent, the ground state wavefunction is a Slater determinant of N one-electron wavefunctions. They are found by solving the following set of Schrödinger equations:

$$\left(-\frac{1}{2} \nabla^2 + v_{eff}[n](\mathbf{r}) \right) \psi_i(\mathbf{r}) = \varepsilon_i \psi_i(\mathbf{r}) \quad (1.70)$$

where ψ_i is a one-electron wavefunction and ε_i the corresponding energy. The density is obtained by

$$n(\mathbf{r}) = \sum_{i=1}^N |\psi_i(\mathbf{r})|^2 \quad (1.71)$$

The above equations have to be solved self-consistently, since the one-electron wavefunctions ψ_i depend on the density via the effective potential, and the density in its turn depends on the wavefunctions. Note that this scheme is only constructed to yield to exact density and energy. The wavefunctions ψ_i and energies ε_i of the fictitious system have no a priori physical meaning. However, sometimes they are used, with varying success.¹⁶ For the effective potential we must take

$$v_{eff}[n](\mathbf{r}) = \sum_{\alpha=1}^{N_{nuc}} \frac{-Z_{\alpha} n(\mathbf{r})}{|\mathbf{R}_{\alpha} - \mathbf{r}|} + \int \frac{n(\mathbf{r}')}{|\mathbf{r} - \mathbf{r}'|} d\mathbf{r}' + \frac{\delta E_{xc}[n]}{\delta n(\mathbf{r})} \quad (1.72)$$

The problem is now to find the correct expression for $E_{xc}[n]$, or equivalently for its functional derivative $v_{xc}[n](\mathbf{r}) \equiv \frac{\delta E_{xc}[n]}{\delta n(\mathbf{r})}$, where $v_{xc}[n](\mathbf{r})$ is called the exchange-

correlation potential. Solving the above set of equations is very similar to the Hartree-Fock method. However, the potential in the Hartree-Fock method is non-local, i.e. it is different for each electron. In the Kohn-Sham scheme the potential is the same for each electron, much facilitating the computations. Also, when we would know the exchange-correlation potential exactly the density and energy according to the Kohn-Sham scheme are also exact.

A very successful approximation for $v_{xc}[n](\mathbf{r})$ is the local density approximation (LDA). Here $v_{xc}[n](\mathbf{r})$ is taken from the results for a homogeneous electron gas where $n(\mathbf{r})$ is constant. These results are exact for the high- and low-density limits, but not for arbitrary $n(\mathbf{r})$. The assumption is that at a point \mathbf{r}' an electron experiences an exchange-correlation potential as though in every point \mathbf{r} the electron density is the same as at point \mathbf{r}' , so to calculate $v_{xc}[n](\mathbf{r} = \mathbf{r}')$ one takes $n(\mathbf{r}) = n(\mathbf{r} = \mathbf{r}')$ for all \mathbf{r} . Nowadays, the exchange-correlation potential is often parameterised from the results of quantum Monte Carlo simulations of a homogeneous electron gas by Ceperley and Alder.¹⁷ This leads to e.g. Perdew-Wang functionals.¹⁸ The local density approximation is obviously exact for a system with constant electron density. It becomes increasingly less accurate with increasingly varying electron density. In practice however, it turns out to be very accurate for a whole range of systems.

In case of a molecule, the set of equations (1.70) and (1.71) can be solved by assuming starting molecular orbitals $\psi_i(\mathbf{r})$. The molecular orbitals $\psi_i(\mathbf{r})$ are often expanded into functions of a basis set describing the atomic valence orbitals, which in principle can be any set of functions as long as they satisfy the usual conditions for these orbitals, like normalisability and orthogonality. One then obtains a starting electron density and hence a starting effective potential with which one obtains new molecular orbitals $\psi_i(\mathbf{r})$ via the N Schrödinger equations. These orbitals are then used to calculate a new electron density and effective potential, and one continues until the

input electron density and the output electron density are consistent with each other within a certain desired accuracy. To increase the flexibility of the calculation one can provide two possible trial basis functions for each atomic valence orbital. It is computationally efficient to numerically tabulate these basis functions. This yields a double numerical (DN) basis set. One can add for each type of atom an orbital to the basis set with an angular momentum one integral number higher than that of the highest occupied orbital in the free atom. These orbitals are called polarized orbitals and together with a DN basis set this yields a double numerical polarized or DNP basis set. If one leaves out the p-orbital for hydrogen atoms one obtains a DND basis set, which we use in this thesis. In practice one takes the atomic orbitals of the basis set to be finite in space and this can be implemented in the calculation by using a cutoff radius above which the atomic orbitals vanish.

1.3 Atoms in molecules

In the preceding section we argued that the properties of a system in the groundstate are defined by the electron density $n(\mathbf{r})$ only. This function can be obtained from the wavefunction $\Psi(\mathbf{r}^N) = \Psi(\mathbf{r}_1, \mathbf{r}_2, \dots, \mathbf{r}_N)$ that contains the coordinates of all N electrons,

$$n(\mathbf{r}) \equiv n(\mathbf{r}_1) = N \int \Psi^*(\mathbf{r}^N) \Psi(\mathbf{r}^N) d\mathbf{r}^{N-1} \quad (1.73)$$

with $d\mathbf{r}^{N-1} = d\mathbf{r}_2 d\mathbf{r}_3 \dots d\mathbf{r}_N$. The wavefunction has to be calculated by *ab-initio* methods. The electron density has the conceptual advantage that it is a function in real space rather than in a mathematically constructed high-dimensional Hilbert space, like the wavefunction of the system. Moreover, $n(\mathbf{r})$ is measurable via X-ray diffraction. In X-ray diffraction one can locate the nuclei, because they correspond to maxima in the electron density and thus scatter the most. This suggests that by looking at the topology of $n(\mathbf{r})$, we can locate the nuclei. This approach has been developed by Bader in his theory ‘Atoms in Molecules’.¹⁹ By analyzing the topological properties of the electron density $n(\mathbf{r})$ one can not only locate the nuclei, but also define atomic properties like the net charge of an atom, its polarization and its energy. This method also clarifies the concept of a bond between atoms. Determining whether there is a bond between two atoms is straightforward. If there is a finite internuclear separation r_0 for which the combined energy $E(r_0)$ of the system of two atoms is a minimum then there is a bond between the two atoms. For a polyatomic system consisting of more than two atoms assigning bonds in this way is not as straightforward, for how can one tell which atoms are bonded with which other atoms by just looking at the total energy of the whole system? Using Bader’s approach one can uniquely define bonds between atoms in a crystal or in a molecule.

We will illustrate this method by looking at a simple molecule, ethene or C_2H_4 . It consists of two carbon atoms, each bonded with two hydrogen atoms (see Fig. 1.5a). In Fig. 1.5b we show the corresponding electron density through the plane containing all 6 atoms. Clearly the maxima in $n(\mathbf{r})$ give the position of the nuclei. We look at the

gradient of the electron density, $\nabla n(\mathbf{r})$, and the paths in real space one gets when following $\nabla n(\mathbf{r})$, the gradient paths.

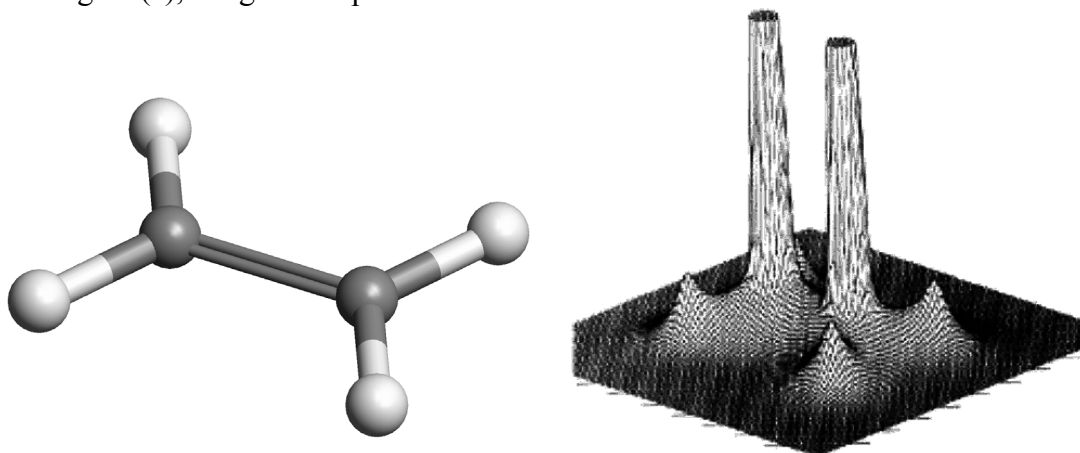


Figure 1.5 (a) The ethene molecule, C_2H_4 . (b) The electron density $n(\mathbf{r})$ for ethene through the plane containing all 6 atoms.

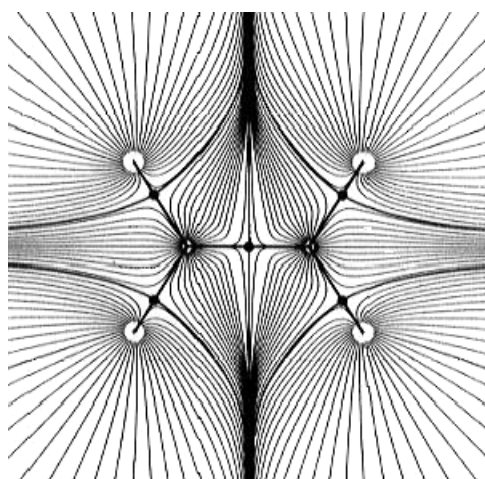


Figure 1.5 (c) Gradient paths $\nabla n(\mathbf{r})$ for this plane. The thick lines are special gradient paths that either end or start at a bond critical point. The ones that end at a bond critical point form the atomic basins, the ones that start at a bond critical point form the bonds.

For ethene some of the gradient paths are shown in Fig. 1.5c. The gradient paths have a sense since they always point towards higher electron density. They will thus end when reaching a maximum in $n(\mathbf{r})$ where $\nabla n(\mathbf{r}) = 0$. As is visible in Fig. 1.5c most of the gradient paths end at a nucleus. We note that gradient paths cannot intercept each other except at points where $\nabla n(\mathbf{r})$ vanishes. The set of gradient paths all ending at the same nucleus defines a distinct region in space. This region is called an atomic basin. An atom is defined as the union of an atomic basin and the nucleus or the local maximum in $n(\mathbf{r})$, the endpoint of the gradient paths. It can be shown that an atom thus defined coincides with the normal concept of an atom as used in chemistry: it is transferable

from one system to another and its properties are additive to yield the corresponding property of the total system. One can now define the average $A(\Omega)$ of the operator $\hat{A}(\mathbf{r}^N)$,

$$A(\Omega) = \frac{1}{2} N \int_{\Omega} d\mathbf{r} \int d\mathbf{r}^{N-1} \left(\Psi^* \hat{A} \Psi + (\hat{A} \Psi)^* \Psi \right) \quad (1.74)$$

where the first integration sign designates integration over the volume of the atomic basin Ω . For example, if we put the operator \hat{A} to ∇^2 we obtain the atomic kinetic energy. For $\hat{A}=1$ we get the atom's electronic population $N(\Omega)$,

$$N(\Omega) = \int_{\Omega} d\mathbf{r} n(\mathbf{r}) \quad (1.75)$$

which yields the net charge of the atom via $(Z - N(\Omega))e$ with Z the charge of the nucleus and e the fundamental charge. For a discussion of other atomic properties we refer to Bader.¹

If we look again to Fig. 1.5b we can also see 'ridges' in the electron density that connect the maxima in $n(\mathbf{r})$. These ridges correspond to the bonds between the atoms. Again we start with the gradient paths of the electron density. In Fig. 1.5c we can distinguish gradient paths that start at a saddle point on the ridges in $n(\mathbf{r})$ between the maxima, where $\nabla n(\mathbf{r}) = 0$, and end at a nucleus. Such a gradient path follows the ridge in $n(\mathbf{r})$. Two paths both originating at the same saddle point thus connect two nuclei with each other. Alternatively, such a pair of gradient paths connecting two nuclei forms a line on which the electron density is a maximum with respect to any other neighbouring line. This line is called the atomic interaction line. An atomic interaction line is a bond-path when the forces on the nuclei vanish (otherwise there clearly is no bonding). The result for ethene is shown in Fig. 1.5c, and it resembles the way chemists would normally draw the bonds between the atoms in ethene. In most cases one indeed recovers the normal chemist's picture of the bonds in a molecule or a crystal. However, sometimes the bond-paths are curved, which is a sign of strain or bond instability. In special occasions one can find bond-paths that do not end at a nucleus, but at another saddle point. Points \mathbf{r}_c in space where $\nabla n(\mathbf{r} = \mathbf{r}_c) = 0$ are called critical points. Both maxima and saddle points are examples of critical points. A saddle point on a bond-path is normally called a bond critical point. Critical points are classified according to the eigenvalues of the Hessian of the electron density, $\nabla(\nabla n(\mathbf{r}))$. We obtain three eigenvalues that can be either positive or negative. This results in four possible sign patterns, (---), (--+), (-++) and (+++) and this gives rise to four different kinds of critical points, (3,-3), (3,-1), (3,+1) and (3,+3). A maximum is a (3,-3) critical point and a bond critical point a (3,-1) critical point. A (3,+1) critical point is a ring critical point, and a (3,+3) critical point is a minimum. It is possible to distinguish different kind of bonds. For this one has to look at the Laplacian of the electron density, $\nabla^2 n(\mathbf{r})$ (which is equal

to the sum of the eigenvalues of the Hessian). If $\nabla^2 n(\mathbf{r}) < 0$ the electronic charge is locally concentrated in point \mathbf{r} . Conversely when $\nabla^2 n(\mathbf{r}) > 0$ the electronic charge is locally depleted. From the topology of $\nabla^2 n(\mathbf{r})$ one can map electron pairs, a concept normally used in chemistry to describe the mechanism of bond forming.¹⁹ It is especially useful to look at the values of $n(\mathbf{r})$ and $\nabla^2 n(\mathbf{r})$ at a bond critical point \mathbf{r}_c . When $\nabla^2 n(\mathbf{r}_c) < 0$ and large in magnitude, $n(\mathbf{r}_c)$ is also large and the electronic charge is concentrated at \mathbf{r}_c . We have a situation where electrons are shared between two nuclei, usually characterized as a covalent or polar bond, or shared interaction. The opposite case when $\nabla^2 n(\mathbf{r})$ is positive and $n(\mathbf{r})$ low in value designates closed-shell interactions, such as ionic bonds, hydrogen bonds and van der Waals bonds. Here the atoms are bound because of the charge being concentrated in the atomic basins, not at the critical point. A far more elaborate discussion is hold by Bader.¹⁹

References

1. S.W. Lovesey, *Theory of Neutron Scattering from Condensed Matter* (Clarendon press, Oxford, 1984)
2. G.L. Squires, *Introduction to the Theory of Thermal Neutron Scattering* (Dover Publications, Mineola, New York, 1996)
3. M. Bée, *Quasielastic Neutron Scattering* (Adam Hilger, Bristol, 1988)
4. G.H. Vineyard, *J. Phys. Chem. Solids* **3** (1957) 121
5. C. Brot, *Chem. Phys. Lett.* **3** (1969) 319
6. A. B. Gardner, J. Howard, T.C. Waddington, R.M. Richardson & J. Tomkinson, *Chem. Phys.* **57** (1981) 453
7. C. Sourisseau, G. Lucazeau, A.J. Dianoux & C. Poinignon, *Mol. Phys.* **2** (1983) 367
8. G.J. Kearley, *Nucl. Instr. Meth. A* **354** (1995) 53
9. E.B. Wilson, J.C. Decius & P.C. Cross, *Molecular Vibrations, The Theory of Infrared and Raman Vibrational Spectra* (McGraw-Hill, New York, 1955)
10. M. Born & J.R. Oppenheimer, *Ann. Physik* **84** (1927) 457
11. D.R. Hartree, *Proc. Cambridge Phil. Soc.* **24** (1928) 89
12. V. Fock, *Z. Physik* **61** (1930) 126; **62** (1930) 795
13. J.C. Slater, *Phys. Rev.* **35** (1930) 210
14. P. Hohenberg & W. Kohn, *Phys. Rev.* **136** (1964) B864
15. W. Kohn & L.J. Sham, *Phys. Rev.* **140** (1965) A1133
16. P.A. Bobbert, *Density Functional Theory, AIO Course of the Dutch Research School for Theoretical Physics* (Nijmegen, 1999)
17. D.M. Ceperley & B.J. Alder, *Phys. Rev. Lett.* **45** (1980) 566
18. J.P. Perdew & Y. Wang, *Phys. Rev. B* **45** (1992) 13244
19. Bader, R.F.W. *Atoms in Molecules. A Quantum Theory* (Clarendon Press, Oxford, 1990)

Chapter 2. Localization of ferrocene in NaY zeolite by powder X-ray and neutron diffraction

E. Kemner, A.R. Overweg, L. van Eijck, A.N. Fitch, E. Suard, I.M. de Schepper & G.J. Kearley, *Submitted to J. Phys. Chem. B*

Abstract

We study the inclusion of the metallocene ferrocene $\text{Fe}(\text{C}_5\text{H}_5)_2$ molecules in the supercages of NaY zeolite. To find the exact location of the ferrocene molecules within the supercages we perform neutron and powder X-ray diffraction on bare NaY zeolite, and on NaY zeolite loaded with one or two ferrocene molecules per supercage. Using the complementary properties of both techniques we show that the ferrocene molecules are located just above a line joining two neighbouring sodium ions at the SII positions in the zeolite supercage. The C_5H_5 rings are oriented towards the sodium ions in an ordered manner. This structure is confirmed by quantum chemistry calculations. The inclusion of ferrocene in a Y-type zeolite provides a homogeneous distribution of iron throughout the zeolite at well-defined locations.

2.1 Introduction

Confinement of transition metals in the voids of zeolite host frameworks has gained considerable attention over the last years.¹⁻⁵ The motivation for this stems from the future prospects of applications in heterogeneous catalysis. Several methods have been applied for the inclusion of transition metals in the cavities of zeolites. The inclusion of metallocenes in the supercages of faujasite type zeolites provides an alternative to classical methods of metal incorporation, such as conventional ion exchange. This new inclusion method has the advantage that the metal will be deposited only in the supercages, where it is wanted to perform the desired catalytic activity. We will show that with this method the transition metals are homogeneously distributed throughout the zeolite at well-defined locations.

Here we study the inclusion of the metallocene ferrocene $\text{Fe}(\text{C}_5\text{H}_5)_2$ molecules in the supercages of NaY zeolite. Ferrocene consists of an iron atom ‘sandwiched’ by two identical parallel cyclopentadienyl C_5H_5 rings with a radius of 2.3 Å, separated by approximately 3.3 Å. NaY zeolite, $\text{Na}_x(\text{AlO}_2)_x(\text{SiO}_2)_{192-x}$, contains so-called supercages (depicted in Fig. 2.1) with a diameter of about 12 Å which are interconnected through windows with a diameter of 9 Å and which are thus accessible to the ferrocene molecules. Each of these supercages contains four sodium ions on the surface of the framework, on the so-called SII positions (see Fig. 2.1).

To fully understand the interaction between the ferrocene molecules and the zeolite framework, a knowledge of the location of ferrocene in the zeolite host is required. In the present study we determine the location of ferrocene in NaY zeolite by means of powder X-ray and neutron diffraction at a temperature $T = 10$ K and $T = 1.5$ K, respectively, for loadings of one and two ferrocene molecules per supercage. Using the complementary properties of both techniques we show that the ferrocene molecules are located just above a line joining two neighbouring sodium ions at the SII positions in the zeolite supercage with the C_5H_5 rings oriented towards the sodium ions in an ordered manner for loadings with one and two ferrocene molecules per supercage.

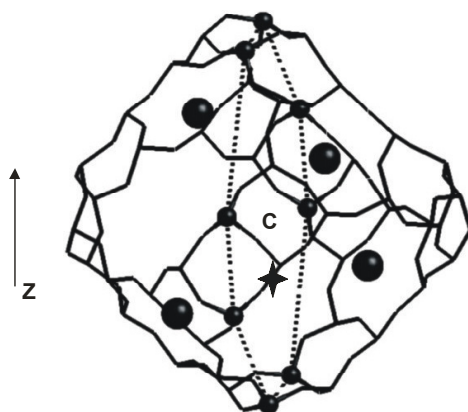


Figure 2.1 The supercage of NaY zeolite. The framework (solid lines) is formed from silicon, aluminium and oxygen atoms. The cage contains four sodium ions (large dots) at the SII positions. The dashed line connecting 8 silicon/aluminium atoms (small dots) gives the plane for which we show a Fourier difference map in Fig. 2.3. The C represents the centre of the supercage, the cross the position of an iron atom as determined from Fig. 2.3.

2.2 Experimental section

The unit cell composition of the NaY zeolite, when dehydrated, is $Na_{55}(AlO_2)_{55}(SiO_2)_{137}$. The zeolite was first dehydrated. For the X-ray diffraction experiments the bare zeolite was then loaded with ferrocene $Fe(C_5H_5)_2$, in a way similar as described by Overweg et al., with an amount of ferrocene corresponding to one and two ferrocene molecules per supercage. After loading, the samples were transferred under nitrogen atmosphere in glass capillaries with a diameter of 1.0 mm, which were then sealed.

Because of the high incoherent scattering cross section of hydrogen we used deuterated ferrocene $Fe(C_5D_5)_2$ for the neutron diffraction experiments. The zeolite was loaded with deuterated ferrocene in the same way as described above, and the samples were transferred under nitrogen atmosphere into vanadium cylinders with a diameter of 7 mm which were sealed with indium.

Powder X-ray diffraction was performed at the BM16 diffractometer of the ESRF in Grenoble, France. We measured NaY zeolite loaded with one and two ferrocene molecule per supercage at a temperature $T = 10$ K. Dehydrated bare NaY zeolite was also measured, at a temperature $T = 300$ K. The wavelength of the synchrotron radiation was 0.803157 Å. The X-ray diffraction patterns were collected for 2θ angles from 0° till 78° .

Powder neutron diffraction was performed at the D2b diffractometer of the ILL in Grenoble, France. We measured NaY zeolite loaded with one and with two deuterated ferrocene molecules at a temperature $T = 1.5$ K. Dehydrated bare NaY zeolite was measured at room temperature. The wavelength of the neutrons was 2.398 Å. Neutron diffraction patterns were collected for 2θ angles from 0° till 158° .

The data were analysed by the Rietveld method using the program WinMProf.⁶ The unit-cell, zero-point, overall scale factor, peak-width, asymmetry and background parameters were refined simultaneously with the structural and thermal parameters. Isotropic thermal parameters were used for all atoms.

2.3 Structure determination

The structure of the bare NaY zeolite that we determine from X-ray and neutron diffraction at room temperature is found to be consistent with that obtained from earlier X-ray and neutron diffraction studies.⁷ The space group is Fd3m. The observed, calculated and difference profiles for bare NaY zeolite are shown in Fig. 2.2a and 2.2b for the neutron and X-ray data, respectively. For clarity we show part of the diffraction patterns only. The final structural parameters to which the refinements converged are shown in Table 2.1a and 2.1b.

Atom	position	x/a	y/a	z/a	B (Å ²)	N
Si/Al	192i	-0.0547(2)	0.0348(3)	0.1250(3)	0.71(8)	192
O(1)	96h	0	-0.1061(2)	0.1061(2)	1.3(2)	96
O(2)	96g	-0.0025(2)	-0.0025(2)	0.1423(3)	2.0(2)	96
O(3)	96g	0.1770(2)	0.1770(2)	-0.0336(3)	3.0(2)	96
O(4)	96g	0.1780(2)	0.1780(2)	0.3171(3)	2.8(2)	96
Na(1)	32e	0.2325(4)	0.2325(4)	0.2325(4)	2.2(5)	32(1)
Na(2)	32e	0.0563(8)	0.0563(8)	0.0563(8)	2.2(5)	13(1)
Na(3)	16c	0	0	0	2.2(5)	6.4(6)

a = 24.8150(2) Å, R_I = 6.33%, R_P = 22.21%, R_{WP} = 20.55%, R_E = 19.04%

Atom	position	x/a	y/a	z/a	B(Å ²)	N
Si/Al	192i	-0.05438(2)	0.03587(2)	0.12464(2)	0.935(7)	192
O(1)	96h	0	-0.10610(4)	0.10610(4)	1.61(4)	96
O(2)	96g	-0.00220(5)	-0.00220(5)	0.14172(7)	2.06(4)	96
O(3)	96g	0.17630(5)	0.17630(5)	-0.03372(7)	2.34(4)	96
O(4)	96g	0.17819(5)	0.17819(5)	0.31773(7)	2.04(4)	96
Na(1)	32e	0.23413(4)	0.23413(4)	0.23413(4)	2.56(7)	31.5(3)
Na(2)	32e	0.05415(9)	0.05415(9)	0.05415(9)	3.1(2)	15.8(3)
Na(3)	16c	0	0	0	5.3(4)	7.2(3)

a = 24.8096(0) Å, R_I = 4.68%, R_P = 9.08%, R_{WP} = 10.23%, R_E = 6.24%

Table 2.1 Final parameters and R factors obtained from a Rietveld refinement on neutron (a) and X-ray (b) powder diffraction on bare NaY zeolite.

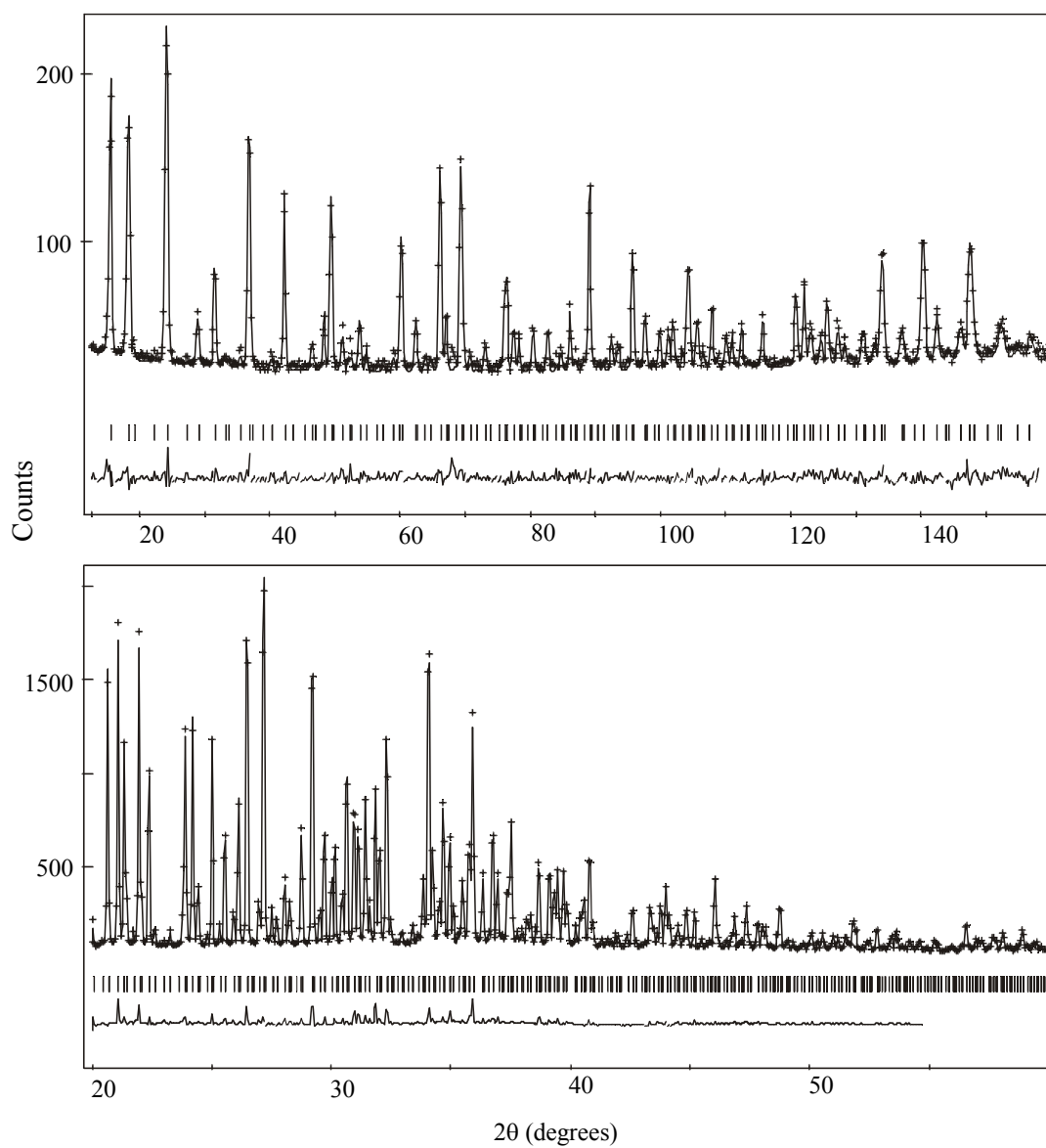


Figure 2.2 Observed, calculated and difference profiles for neutron powder diffraction (a) and X-ray powder diffraction (b) on bare dehydrated NaY zeolite.

We observe no symmetry changes due to the insertion of ferrocene in the zeolite. An initial refinement on the X-ray diffraction pattern of one ferrocene molecule per zeolite supercage using only the atoms of the zeolite framework and the sodium ions gave an unsatisfactory fit. This means that the ferrocene molecules contribute significantly to the diffraction pattern. We calculated Fourier difference maps with the program Gfour⁸ using the observed intensities of the peaks for the pattern on zeolite loaded with ferrocene and those calculated for bare zeolite by WinMProf. These maps then give the missing scattering density (electron density in case of X-ray scattering) in the calculated fit projected on real space. The Fourier difference map on the plane perpendicular to the [0,1,0] axis about the centre of the supercage located at (3/8, 3/8, 3/8) is shown in Fig. 2.3. This plane and the zeolite framework atoms that lie in it are also indicated in Fig. 2.1. There are four spots in this map around the centre of the supercage with significant missing electron density, which we contribute to the presence of iron atoms. Note that although only one ferrocene molecule is present in the supercage, the Fourier map gives more positions because it gives all other positions, which are symmetrically the same. After insertion of iron on these positions in the refinement, the refinement improved, and the spots disappeared in subsequent Fourier difference maps, meaning that the missing electron density indeed corresponded to the presence of iron atoms. One of these iron atoms is depicted with a cross in Fig. 2.3 and this location is also given by the cross in Fig. 2.1.

Fourier difference maps calculated from a refinement on the neutron data on one ferrocene molecule per supercage at 1.5 K using the zeolite framework, the sodium ions and iron at the position as found above give the location of the cyclopentadienyl rings. In the final refinement the geometry of the ferrocene molecule was constrained according to the known geometry of a single (eclipsed) ferrocene molecule⁹ and only the z coordinate is refined. The final results of the refinements on one ferrocene molecule per supercage are shown in Fig. 2.4a and 2.4b and Table 2.2a and 2.2b for the neutron and X-ray data, respectively. We do not include the hydrogen atoms of the cyclopentadienyl rings in the refinement on the X-ray pattern due to their very low scattering factor. Again we show only part of the patterns.

We observe no change in the positions of the ferrocene molecules for the case of two ferrocene molecules per zeolite supercage. The final structural parameters are given in Table 2.3a and 2.3b, the results of the refinements on the collected patterns are shown in Fig. 2.5a and 2.5b. We had to exclude the region up to 20° containing three peaks in the refinement on the neutron data due to the presence of diffuse scattering. Since the number of ferrocene molecules as found from the neutron pattern is less than the number of ferrocene molecules as determined from the preparation, this diffuse scattering may arise from ferrocene molecules outside the zeolite.

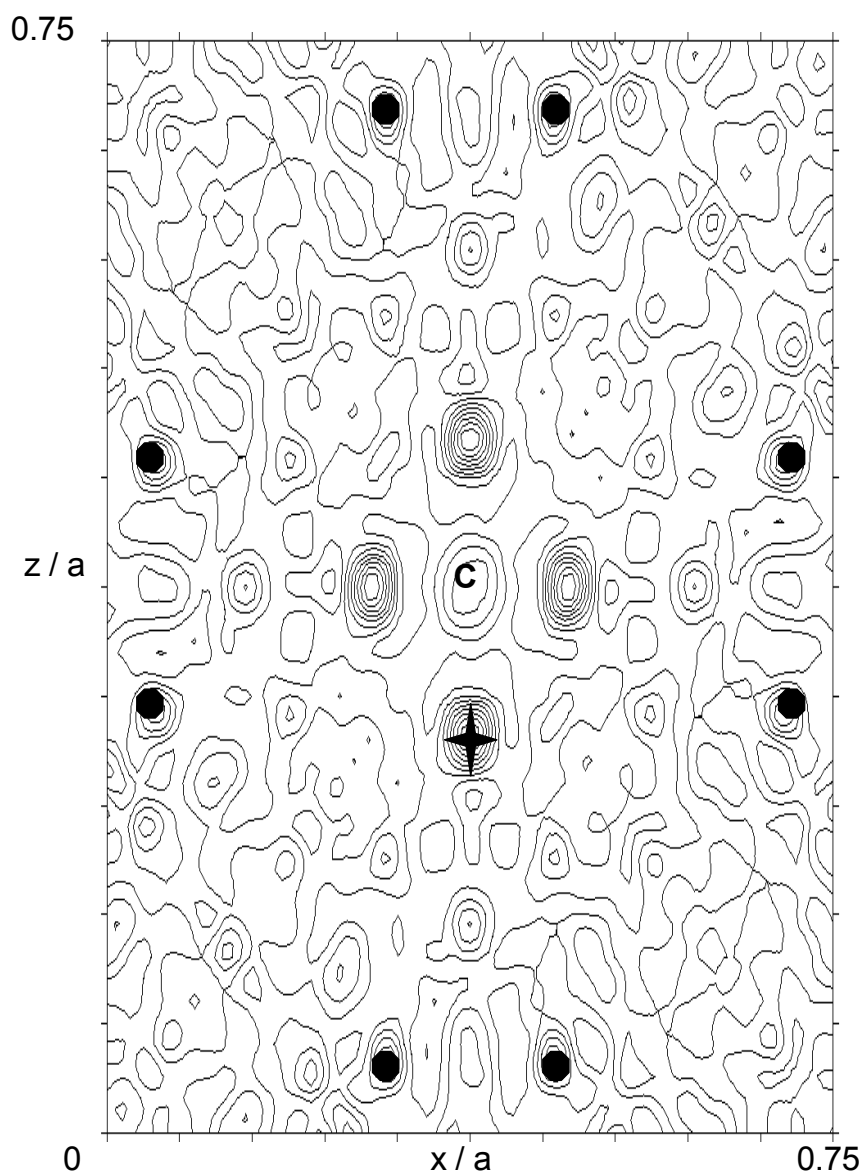


Figure 2.3 Fourier difference map on the plane perpendicular to the $[0,1,0]$ axis about the centre of the supercage located at $(3/8, 3/8, 3/8)$ for the observed intensities of the peaks for the diffraction pattern on zeolite loaded with ferrocene and those calculated for bare zeolite by Rietveld refinement, showing four iron atoms. The small dots represent the framework silicon/aluminium atoms, which lie in this plane (also indicated in Fig. 2.1), the C gives the centre of the supercage. The cross on one of the iron atoms is also indicated in Fig. 2.1, and corresponds to the iron atom in the ferrocene molecule in Fig. 2.8.

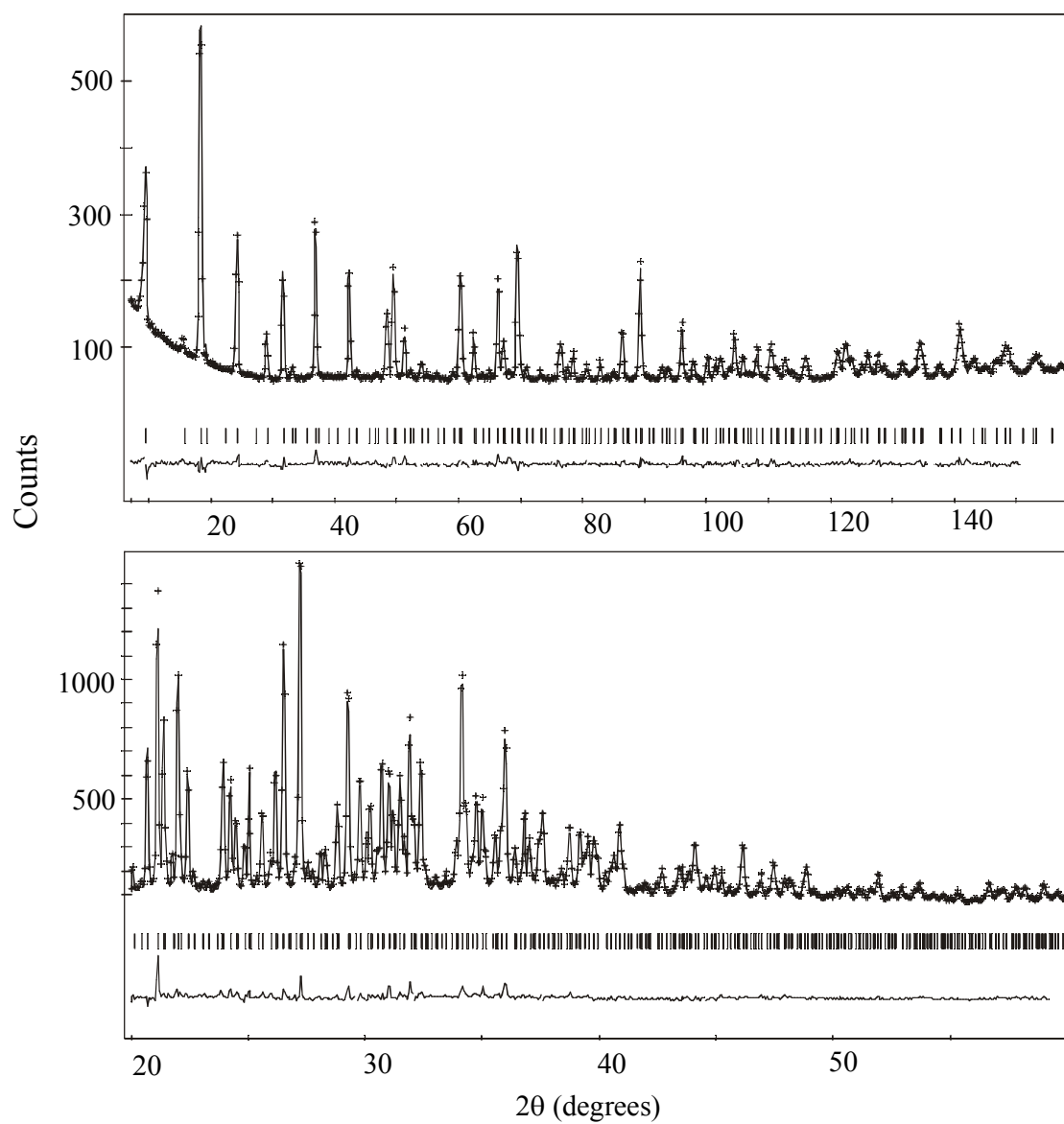


Figure 2.4 Observed, calculated and difference profiles for neutron powder diffraction (a) and X-ray powder diffraction (b) on NaY zeolite loaded with one ferrocene molecule per supercage.

Atom	position	x/a	y/a	z/a	B(Å ²)	N
Si/Al	192i	-0.0548(2)	0.0359(2)	0.1254(2)	0.40(7)	192
O(1)	96h	0	-0.1062(2)	0.1062(2)	1.1(1)	96
O(2)	96g	-0.0025(2)	-0.0025(2)	0.1439(2)	1.8(2)	96
O(3)	96g	0.1782(2)	0.1782(2)	-0.0332(3)	2.9(2)	96
O(4)	96g	0.1760(2)	0.1760(2)	0.3192(3)	2.4(2)	96
Na(1)	32e	0.2355(4)	0.2355(4)	0.2355(4)	1.7(5)	30(1)
Na(2)	32e	0.0591(7)	0.0591(7)	0.0591(7)	2(1)	13(1)
Na(3)	16c	0	0	0	1(1)	6.4(6)
Fe	48f	0.375	0.375	0.2705(3)	1.0(6)	7.54(4)
C(1)	96g	0,3276	0,3276	0.3201(3)	3.3(3)	15.08(8)
C(2)	192i	0,2943	0,3609	0.2858(3)	3.3(3)	30.2(2)
C(3)	192i	0.3070	0,3482	0.2305(3)	3.3(3)	30.2(2)
D(1)	96g	0,3276	0,3276	0.3648(3)	6.4(3)	15.08(8)
D(2)	192i	0,2642	0.3910	0.2997(3)	6.4(3)	30.2(2)
D(3)	192i	0,2884	0,3668	0.1942(3)	6.4(3)	30.2(2)

a = 24.7697(2) Å, R_I = 6.70%, R_P = 16.81%, R_{WP} = 14.93% R_E = 10.47%

Atom	position	x/a	y/a	z/a	B(Å ²)	N
Si/Al	192i	-0.05397(2)	0.03587(2)	0.12430(2)	0.662(4)	192
O(1)	96h	0	-0.10616(5)	0.10616(5)	1.34(5)	96
O(2)	96g	-0.00239(6)	-0.00239(6)	0.14371(7)	1.54(4)	96
O(3)	96g	0.17757(6)	0.17757(6)	-0.03270(8)	1.93(4)	96
O(4)	96g	0.17674(6)	0.17674(6)	0.31859(9)	1.31(4)	96
Na(1)	32e	0.23654(4)	0.23654(4)	0.23654(4)	2.64(7)	33.2(3)
Na(2)	32e	0.0560(1)	0.0560(1)	0.0560(1)	2.1(2)	14.8(3)
Na(3)	16c	0	0	0	1.6(2)	7.7(2)
Fe	48f	0.375	0.375	0.2718(1)	2.6(2)	7.6(1)
C(1)	96g	0,3276	0,3276	0.3214(1)	5.6(3)	15.2(2)
C(2)	192i	0,2943	0,3609	0.2871(1)	5.6(3)	30.4(4)
C(3)	192i	0.3070	0,3482	0.2318(1)	5.6(3)	30.4(4)

a = 24.7669(0) Å, R_I = 3.69%, R_P = 8.25%, R_{WP} = 9.69%, R_E = 6.70%

Table 2.2 Final parameters and R factors obtained from a Rietveld refinement on neutron (a) and X-ray (b) powder diffraction on NaY zeolite loaded with one ferrocene molecule per supercage.

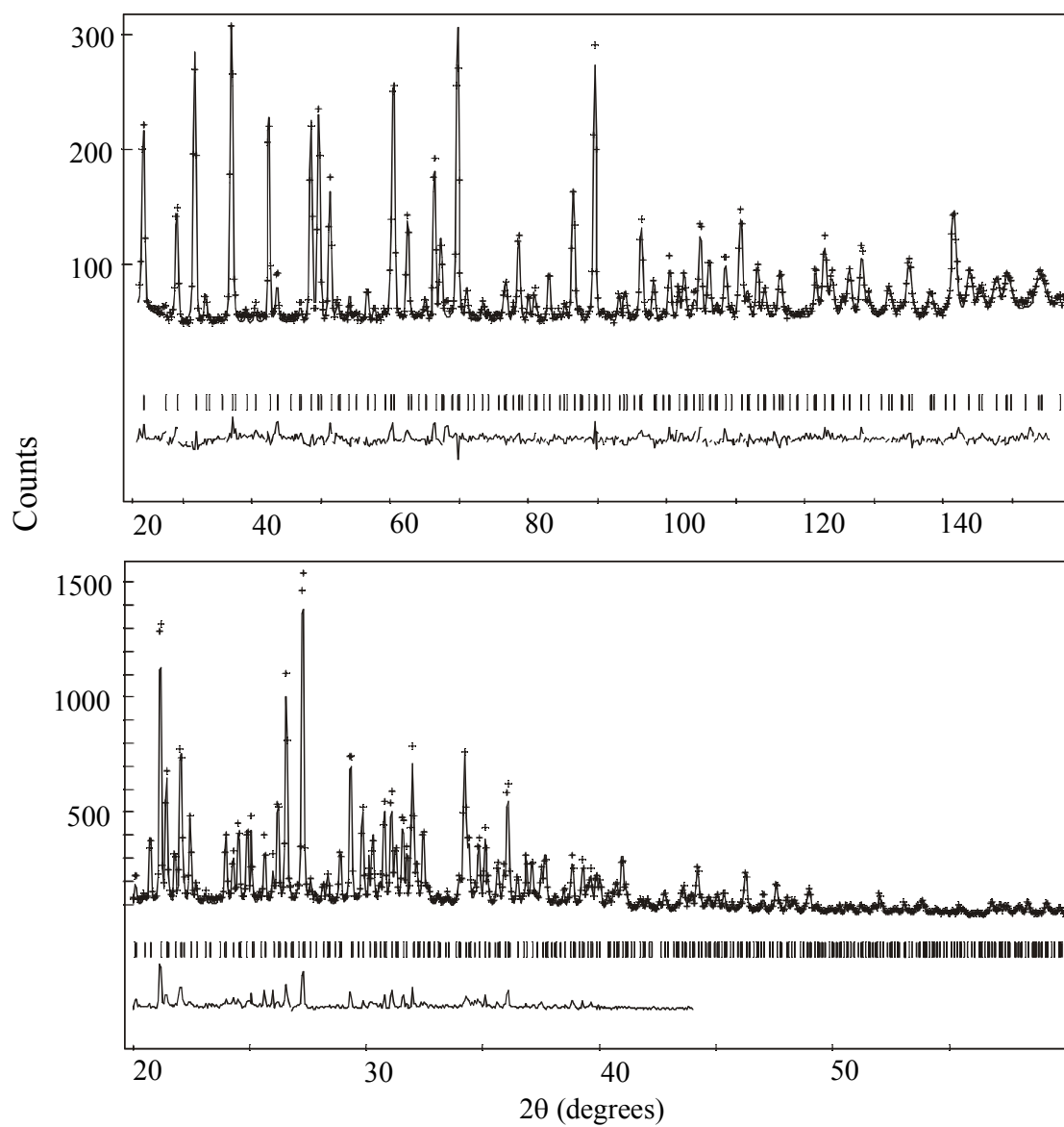


Figure 2.5 Observed, calculated and difference profiles for neutron powder diffraction (a) and X-ray powder diffraction (b) on NaY zeolite loaded with two ferrocene molecules per supercage.

Atom	position	x/a	y/a	z/a	B(Å ²)	N
Si/Al	192i	-0.0541(2)	0.0360(2)	0.1249(2)	0.55(9)	192
O(1)	96h	0	-0.1052(2)	0.1052(2)	2.2(2)	96
O(2)	96g	-0.0034(2)	-0.0034(2)	0.1450(2)	1.9(2)	96
O(3)	96g	0.1785(2)	0.1785(2)	-0.0330(3)	3.4(2)	96
O(4)	96g	0.1756(2)	0.1756(2)	0.3186(3)	3.0(2)	96
Na(1)	32e	0.2397(4)	0.2397(4)	0.2397(4)	4.9(5)	34(1)
Na(2)	32e	0.060(1)	0.060(1)	0.060(1)	4.9(5)	15(1)
Na(3)	16c	0	0	0	4.9(5)	10.2(7)
Fe	48f	0.375	0.375	0.2707(2)	1.3(4)	12.2(2)
C(1)	96g	0,3276	0,3276	0.3203(2)	2.2(2)	24.4(3)
C(2)	192i	0,2943	0,3609	0.2860(2)	2.2(2)	48.8(7)
C(3)	192i	0.3070	0,3482	0.2307(2)	2.2(2)	48.8(7)
D(1)	96g	0,3276	0,3276	0.3650(2)	4.7(2)	24.4(3)
D(2)	192i	0,2642	0.3910	0.2998(2)	4.7(2)	48.8(7)
D(3)	192i	0,2884	0,3668	0.1944(2)	4.7(2)	48.8(7)

a = 24.7129(2) Å, R_I = 7.51%, R_p = 17.64%, R_{WP} = 16.42%, R_E = 11.58%

Atom	position	x/a	y/a	z/a	B(Å ²)	N
Si/Al	192i	-0.05378(3)	0.03590(3)	0.12414(4)	0.71(1)	192
O(1)	96h	0	-0.10628(8)	0.10628(8)	1.66(7)	96
O(2)	96g	-0.00271(9)	-0.00271(9)	0.1445(1)	1.37(7)	96
O(3)	96g	0.1781(1)	0.1781(1)	-0.0323(1)	2.02(7)	96
O(4)	96g	0.17594(9)	0.17594(9)	0.3196(1)	1.38(7)	96
Na(1)	32e	0.24003(7)	0.24003(7)	0.24003(7)	2.7(1)	35.1(4)
Na(2)	32e	0.0584(2)	0.0584(2)	0.0584(2)	2.0(3)	12.4(4)
Na(3)	16c	0	0	0	0.4(3)	7.1(3)
Fe	48f	0,375	0,375	0.2715(1)	2.2(1)	14.6(2)
C(1)	96g	0,3276	0,3276	0.3210(1)	3.9(2)	29.2(4)
C(2)	192i	0,2943	0,3609	0.2868(1)	3.9(2)	58.4(8)
C(3)	192i	0.3070	0,3482	0.2315(1)	3.9(2)	58.4(8)

a = 24.7064(1) Å, R_I = 4.18%, R_p = 13.29%, R_{WP} = 15.16%, R_E = 9.38%

Table 2.3 Final parameters and R factors obtained from a Rietveld refinement on neutron (a) and X-ray (b) powder diffraction on NaY zeolite loaded with two ferrocene molecules per supercage.

2.4 Discussion

There is a clear difference between the patterns for the bare NaY zeolite and the zeolite loaded with one or with two ferrocene molecules per supercage. Due to the higher scattering cross section for the ferrocene molecule as a whole this difference is more pronounced for the neutron diffraction patterns than for the X-ray patterns (the scattering of one ferrocene molecule per supercage amounts to 32% of the total scattering in case of neutron diffraction, and 11% in case of X-ray diffraction). In Fig. 2.6 we show part of the neutron diffraction pattern including the final fit on pure zeolite (top), the corresponding part of the neutron pattern with final fit on one ferrocene molecule per supercage (middle) and the corresponding part of the X-ray pattern with final fit on one ferrocene molecule per supercage (bottom). We have indicated some reflections to illustrate some differences between the three patterns. First there are differences in the relative intensities of the peaks between the neutron diffraction patterns on bare zeolite and on ferrocene in zeolite. One can see, for example, that the intensity of the (10,8,2) reflection is higher than the intensity of the (9,9,3) reflection in case of the bare zeolite but lower in case of the loaded zeolite. The differences between the neutron and the X-ray diffraction patterns on ferrocene in zeolite are more pronounced. For example, the (8,8,4) reflection is of low intensity in case of the neutron pattern, but is much more pronounced in the X-ray pattern. The same goes for the (13,5,1), (10,10,0) and (10,8,2) reflections. Note that the distances between the various reflections shift a bit between the neutron and X-ray patterns because they are plotted as a function of 2θ instead of d spacing.

The adsorption of ferrocene molecules in NaY zeolite has only small effect on the framework structure. One notable effect is a change in the lattice parameter (see also Table 2.4). Fig. 2.7 compares part of the X-ray patterns on pure NaY zeolite and NaY zeolite loaded with one or two ferrocene molecules per supercage. One clearly sees a shift in the position of the peaks, corresponding to a change in the lattice parameter. We find for the bare zeolite a lattice parameter $a = 24.870 \text{ \AA}$ determined from X-ray diffraction and $a = 24.815 \text{ \AA}$ determined from neutron diffraction, which is within the range $24.60 - 25.12 \text{ \AA}$ which is typically found in the literature.⁷ After insertion of one ferrocene molecule per supercage the cell parameter decreases to $a = 24.767 \text{ \AA}$ and 24.770 \AA determined from X-ray and neutron diffraction, respectively. Upon insertion of two ferrocene molecules per supercage the cell parameter further decreases to $a = 24.706 \text{ \AA}$ and $a = 24.713 \text{ \AA}$ as found from X-ray and neutron diffraction.

	a (Å) X-ray	a (Å) neutron
bare NaY	24.810	24.815
+ 1 ferrocene	24.767	24.770
+ 2 ferrocene	24.706	24.713

Table 2.4 Lattice parameter, a , as found from Rietveld refinements on X-ray and neutron diffraction patterns for bare NaY zeolite and NaY zeolite loaded with one or two ferrocene molecules per supercage.

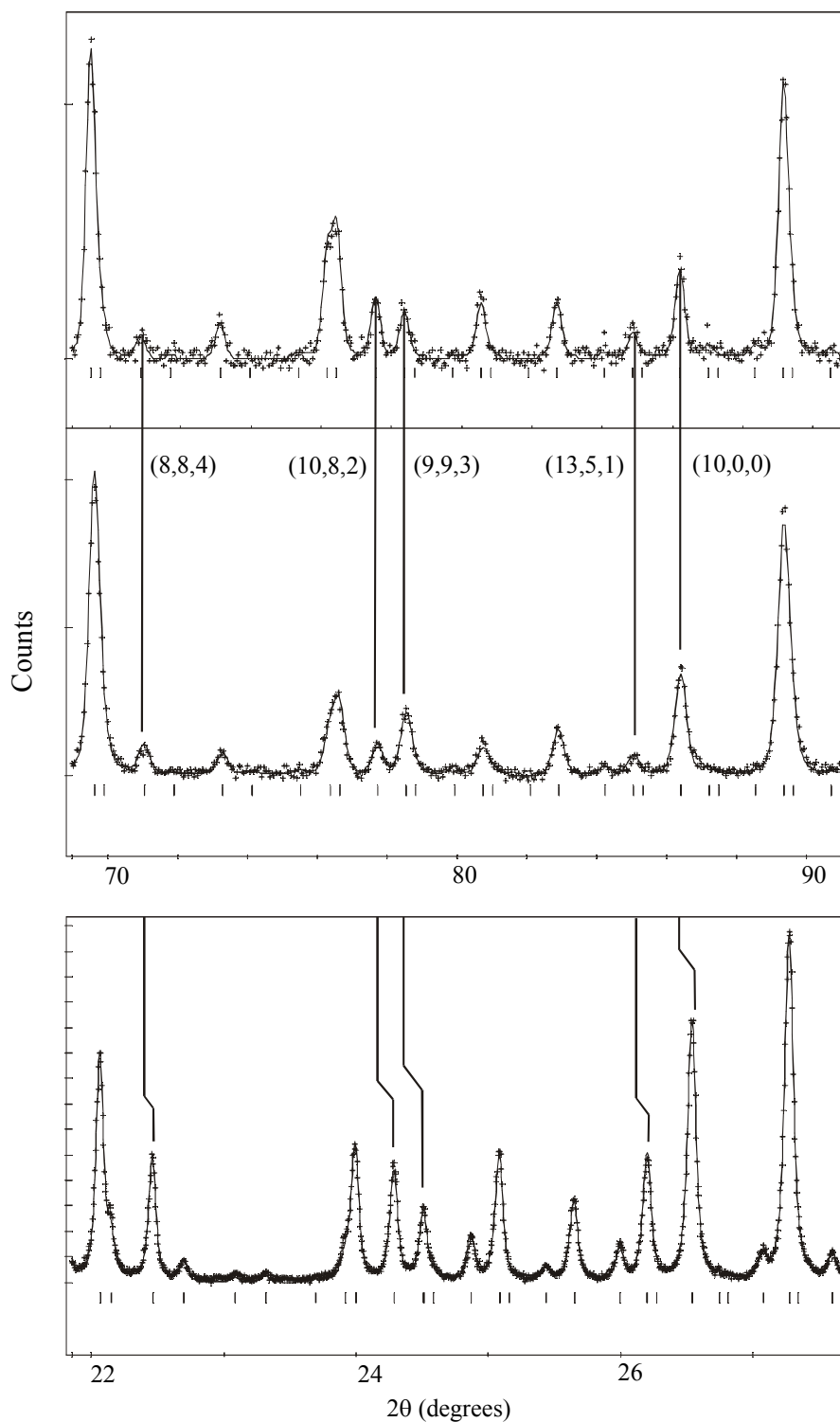


Figure 2.6 Part of the neutron diffraction pattern including the final fit on pure zeolite (top), the corresponding part of the neutron pattern with final fit on one ferrocene molecule per supercage (middle) and the corresponding part of the X-ray pattern with final fit on one ferrocene molecule per supercage (bottom) showing the differences in relative intensity of the reflections.

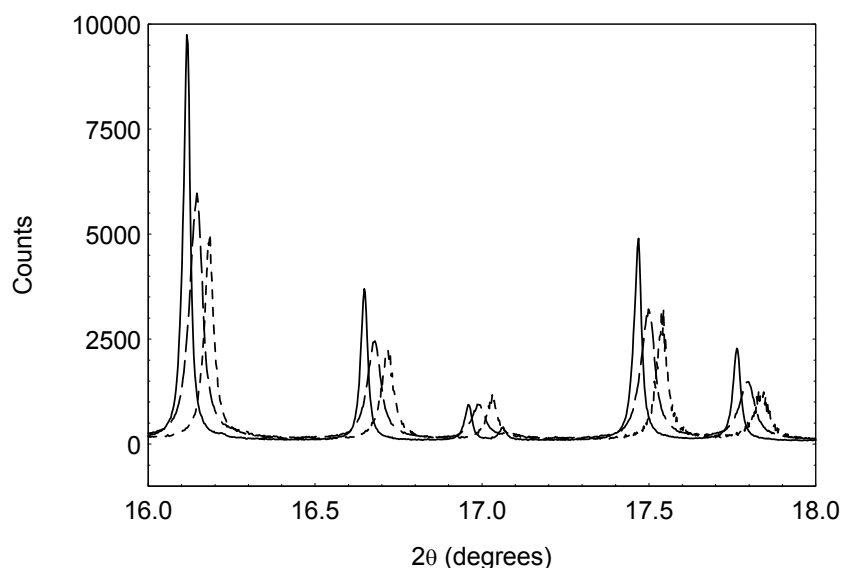


Figure 2.7 Part of the X-ray patterns on pure NaY zeolite (solid line), and NaY zeolite loaded with one (dashed line) or two (dotted line) ferrocene molecules per supercage showing the decrease in lattice parameter upon adsorption of ferrocene molecules in NaY zeolite.

These slight decreases suggest an interaction between the adsorbed ferrocene molecules and the zeolite host. This effect has also been found for benzene in NaY zeolite⁷ and pi-complexes in Y-types zeolites.¹⁰ They suggest that this stems from an interaction between the ions in the zeolite and the pi-electrons of the adsorbed molecules. Indeed we find that for a loading of one ferrocene molecule per supercage the sodium ions at the SII sites shift with 0.083 Å and 0.11 Å for X-ray and neutrons, respectively, towards the center of the supercage, suggesting an interaction between these ions and the cyclopentadienyl rings of the ferrocene molecule. The positions of the sodium ions at the SII sites for loadings of two ferrocene molecules per supercage show an increased shift towards the center of the zeolite supercage, with 0.21 and 0.27 Å compared with the bare zeolite for X-ray and neutrons, respectively. Note that now all sodium ions at the SII sites interact with a ferrocene molecule, whereas in the case of one ferrocene molecule this is on average only half of the sodium ions at these sites. This migration of the sodium cations at the SII sites has also been found for benzene in NaY zeolite, where it was by 0.09 Å for loadings of 2.6 benzene molecules per supercage.⁷

Fig. 2.8 depicts the final result for the position and orientation of the ferrocene molecules with respect to the sodium ions on the SII positions in the zeolite supercage (see also Fig. 2.1 for the whole supercage). Note that the position of the iron atom of the ferrocene molecule corresponds to the cross in Figs. 2.1 and 2.3. The iron atom is on a 48f site, which is on the crossing of two symmetry planes, one parallel to the ferrocene rings through the iron atom, the other perpendicular to the first one, right through the rings. The top carbon and hydrogen (or deuterium) atoms are on a 96g site, the other ones on a general 192i site. With this symmetry only three carbon and three hydrogen or deuterium atoms are needed to fully describe both cyclopentadienyl rings of the

ferrocene molecule in the zeolite supercage. The distance between the centre of the ring and the sodium ion is approximately 3.18 Å for a ferrocene molecule, whereas it is 2.7 Å for a benzene molecule. For the case of two ferrocene molecules per zeolite supercage the second molecule is situated symmetrically the same as the first one, on the top edge of the depicted tetrahedron. Note that the z-axis in Fig. 2.8 corresponds to the z-axis used in the refinement.

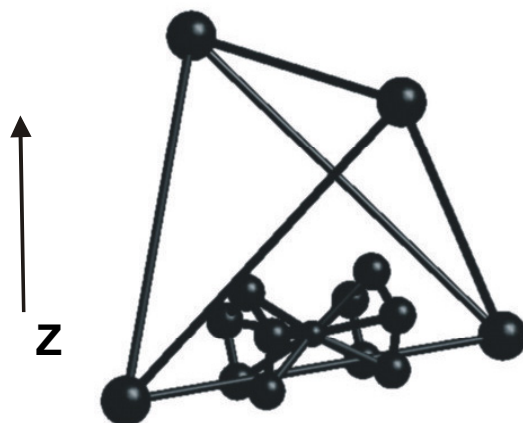


Figure 2.8 Location of a ferrocene molecule in the supercage of NaY zeolite. The large dots connected by solid lines show the four sodium ions in the supercage forming a tetrahedron, and are also shown in Fig. 2.1. The iron atom of the ferrocene molecule is indicated by a cross in Figs. 2.1 and 2.3.

There is no indication that the rings take another orientation than we found, or that they are disordered with respect to each other. Refining the diffraction patterns of ferrocene in zeolite with the rings ‘upside down’ gave notably worse results.

We have also refined the neutron diffraction patterns with the positions of all carbon atoms and deuterium atoms as free parameters. This improves the agreement between the observed and calculated patterns by about 5%. However, the shape of the ferrocene molecule is actually indistinguishable from the starting shape as above because this falls well within the error bars of the positions of the atoms in the ferrocene molecule.

To show that the ferrocene molecule is indeed in an energy minimum on the position in the zeolite supercage as found above we perform *ab-initio* calculations using density functional theory using the module Dmol³ of the program Cerius^{2,11}. For this we optimize the geometry and position of a ferrocene molecule surrounded by a zeolite supercage fragment. The model we use consists of one ferrocene molecule, two sodium cations and part of the zeolite supercage framework as shown in Fig. 2.9. The positions of the atoms are taken from the Rietveld refinement on the neutron diffraction data on one ferrocene molecule per supercage. The oxygen atoms adjacent to the silicon/aluminium atoms are replaced by hydrogen atoms to preserve the electroneutrality of the model. The positions of these terminal hydrogens are fixed during the geometry optimization. The positions of all the other atoms are allowed to

vary. We use the local density approximation, Perdew Wang functionals, the DND basis set,¹¹ and an atomic cutoff radius of 5.5 Å.

After optimization of the geometry we find that the hydrogen atoms of the ferrocene molecule are tilted with about 1.3° from the C₅ rings towards the Fe atom, a trend which is also found with measurements on pure ferrocene¹² or with DFT calculations on a single ferrocene molecule.^{9,13} The ferrocene molecule as a whole virtually stays at the same position, and there are no significant changes in the zeolite fragment. The structure found from the refinements indeed corresponds to an energy minimum.

The difference in total energy between the bare fragment added with the total energy of a single ferrocene molecule as calculated before⁹ and the fragment with a ferrocene molecule amounts to -130 kJ/mol. This compares well with the measured sorption energy of benzene molecules in NaY zeolite, which is around -77 kJmol⁻¹.¹⁴

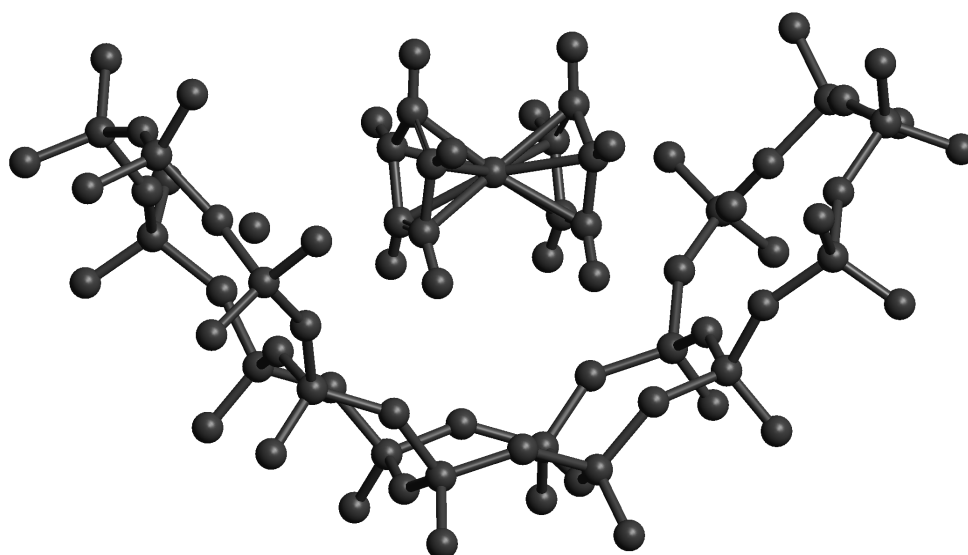


Figure 2.9 Model of a ferrocene molecule inside a zeolite supercage used for DFT calculations.

2.5 Conclusions

We have shown that ferrocene molecules adsorbed in the supercages of NaY zeolite are located just above a line joining two neighbouring sodium ions at the SII positions in the zeolite supercage for loadings of one or two ferrocene molecules per supercage. The cyclopentadienyl C₅H₅ rings of are oriented towards the sodium ions in an ordered manner. The inclusion of ferrocene in a Y-type zeolite thus provides a homogeneous distribution of iron throughout the zeolite at well-defined locations. We have shown this position to be an energy minimum using density functional theory. Also, the unit cell of the zeolite contracts upon adsorption of ferrocene.

With X-ray scattering heavy atoms such as the iron atom in ferrocene are easy to locate due to their high scattering. Lighter atoms, such as for example carbon and hydrogen in the cyclopentadienyl rings of ferrocene, are much harder to locate. Carbon and deuterium atoms are clearly visible in the neutron diffraction patterns, making an accurate determination of the orientation of the cyclopentadienyl rings possible. The combination of both X-ray and neutron powder diffraction could also prove very useful for localizing other transition metal complexes in zeolites with potential applications in e.g. catalysis.

References

1. G.A. Ozin & C. Gil, *Chem. Rev.* **89** (1989) 1749
2. W.M.H. Sachtler & Z. Zhang, *Adv. Catal.* **39** (1993) 129
3. T. Bein, *Comprehensive Supramolecular Chemistry* 1st ed.; Atwood J. L., Davies, J. E. D., MacNicol, D. D., Vögtle, F., Eds.: Elsevier Science Ltd., 1996; Vol. 7, Chapter 20
4. A.R. Overweg, H. Koller, J.W. de Haan, L.J.M. van de Ven, A.M. van der Kraan, & R.A. van Santen, *J. Phys. Chem. B* **103** (1999) 4298
5. E. Kemner, I.M. de Schepper, A.J.M. Schmets, H. Grimm, A.R. Overweg, & R.A. van Santen, *J. Phys. Chem. B* **104** (2000) 1560
6. A. Jouanneaux, *CPD newsletter* **21** (1999) 13
7. A.N. Fitch, H. Jobic & A. Renouprez, *J. Phys. Chem.* **90** (1986) 1311
8. ftp://charybde.saclay.cea.fr/pub/divers/progs_pc/fourier/
9. E. Kemner, I.M. de Schepper, G.J. Kearley & U.A. Jayasooriya, U. A. *J. Chem. Phys.* **112** (2000) 10926
10. M. Czjzek, H. Fuess & T. Vogt, *J. Phys. Chem.* **95** (1991) 5255
11. B. Delley, *J. Chem. Phys.* **354** (1995) 53
12. P. Seiler, J.D. Dunitz, *Acta Crystallogr., Sect. B: Struct. Crystallogr. Cryst. Chem.* **35** (1994) 2020
13. A. Bérces, T. Ziegler & L. Fan *J. Phys. Chem.* **98** (1994) 1584
14. S.M. Auerbach, L.M. Bull, N.J. Henson, H.I. Metiu & A.K. Cheetham, *J. Phys. Chem.* **100** (1996) 5923

Chapter 3. How van der Waals bonds orient molecules in zeolites

E. Kemner, I.M. de Schepper & G.J. Kearley, *Submitted to Chem. Comm.*

Abstract

We study the bindings between a ferrocene guest molecule and the zeolite host by a topological analysis of the electron density as calculated by density functional theory. It transpires that the guest and host are not only connected by hydrogen bonds, but also by some novel bond-paths between region of high electron density on the guest and atoms of the zeolite cage. These bonds are comparable with weak hydrogen bonds. The electronic structure of the ferrocene molecule itself barely changes. It is the orientation in which the ferrocene molecule is held in the zeolite that renders it more reactive.

3.1 Introduction

How is a guest molecule held in a zeolite cage? What is the bonding? How does this affect the reactivity of the guest? To answer these questions in a coherent manner we must examine the topology of electron density between the host and the guest, and then reconsider what we mean by ‘bonding’. Using the approach pioneered by Bader,¹ we reveal only weak H-bonds and even weaker van der Waals bonds between the host and the guest. Yet the reactivity of the guest (ferrocene in the present case) is dramatically increased when it is in the zeolite.^{2,3} The popular concept that the increased reactivity of the guest arises from changes in its electronic structure is incorrect in the present case, and it is the orientation in which the guest ferrocene molecule is held that renders it vulnerable to attack. Analyses of this type in which we separate the electronic and steric effects may have a general impact on the study of catalytic systems. In the current study the guest molecule is ferrocene, $\text{Fe}(\text{C}_5\text{H}_5)_2$, (an iron atom ‘sandwiched’ by two identical parallel cyclopentadienyl C_5H_5 rings) held within the host lattice of NaY zeolite, $\text{Na}_x(\text{AlO}_2)_x(\text{SiO}_2)_{192-x}$. The original interest in this system stems from its use as a preparative route by which iron may be included in the zeolite. The ferrocene molecules occupy “supercages” (shown in Fig. 3.1) in the zeolite which have a diameter of about 12 Å, and each of these contains four sodium ions on its walls (see Fig. 3.1). We have recently determined the position of the ferrocene molecule in the supercage of NaY zeolite to be 0.87Å above a line joining two sodium ions, using powder X-ray and neutron diffraction⁴ (see Fig. 3.1). The question immediately arises as to why the ferrocene molecule does not lie on the line joining two sodium ions since then it would optimize the Coulombic interaction between the π -systems of the aromatic rings and the sodium ions. Such a position would also lead to considerably shorter hydrogen bonds

between the cyclopentadienyl hydrogen atoms and the oxygen atoms of the zeolite. Where is the energy-gain in leaving the ferrocene molecule almost 1 Å above the Na^+ - Na^+ vector, and how can we quantify this? One possibility would be to map out the potential-energy hypersurface of the ferrocene along its normal-mode vectors. A subsequent examination of this map for all atom pairs would reveal the origin of the observed ferrocene position. A far more convenient approach is a direct examination of the electron density for evidence of bonds between the ferrocene molecule and the zeolite cage. An analysis of the electron density should be able to account for the observed location of the ferrocene molecule, and more important, the increased reactivity with respect to the pure compound.

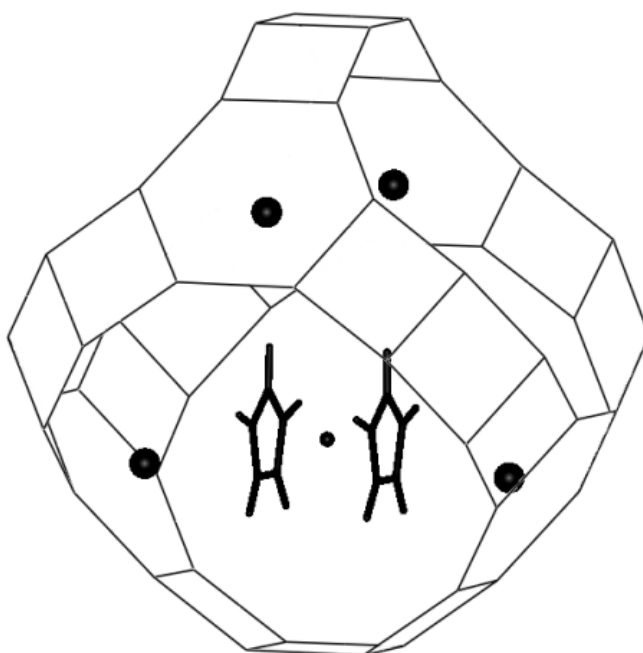


Figure 3.1 Location and orientation of a ferrocene molecule (bold) inside a NaY zeolite supercage. The four spheres show the position of the sodium ions on the walls of the zeolite supercage.

3.2 Results

The first step in the analysis is to ensure that the atomic positions derived from crystallography do indeed correspond to the energy minimum, and that there is consistency between observation and calculation. We achieve this by modelling a realistic fraction of the zeolite containing the ferrocene (Fig. 3.2). The energy of the system is then minimised with respect to the ferrocene position using *ab-initio* density functional theory (Dmol³ within the suite Cerius2)⁵. We use the local density approximation, Perdew Wang functionals, the DND basis set, and an atomic cutoff

radius of 5.5 Å. After optimization of the geometry we find that there is no significant difference in the atomic positions from diffraction experiments and DFT calculations.

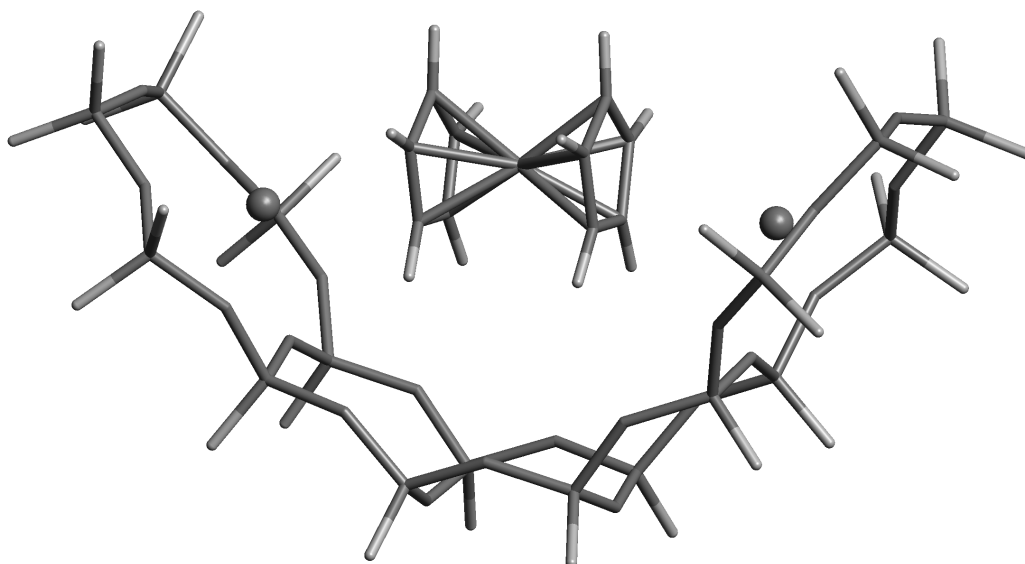


Figure 3.2 Illustration of the zeolite fragment and the ferrocene molecule as used for DFT calculations. Sodium ions are represented by spheres. The oxygen atoms adjacent to the zeolite framework have been replaced by hydrogen atoms.

The DFT calculations also provide the total electron density $n(\mathbf{r})$ map for the model, which we use to perform a topological analysis, and hence obtain a straightforward definition of bonds between atoms. We start by locating the critical points in the electron density, that is, where the gradient of the electron density $\nabla n(\mathbf{r})$ vanishes. In addition to the maxima associated with atom positions, there are also saddle points where the curvature is positive in one direction and negative in the two others. Saddle points are located somewhere in between the nuclei and are usually termed “bond critical points”. The next step is to identify “gradient paths”, i.e. curves such that the gradient vector $\nabla n(\mathbf{r})$ is tangent to it in every point. We will term these paths “ridges” because they are analogous to ridges in a mountainous landscape. Some ridges that originate at a bond critical point and lead to atoms (peaks, in our analogy), and these ridges correspond to bonds. We perform this topological analysis on the electron density with the program FAST,⁶ the results for the bond critical points and the ridges for the model being shown in Fig. 3.3.

All of the bonds that one normally would expect in the zeolite framework and in the ferrocene molecule, are found as expected, but what is of interest here are the bonds that we find between the ferrocene and the zeolite framework. These go via the cyclopentadienyl rings. There are four bonds (or ridges in the electron density) connecting each cyclopentadienyl ring of the ferrocene molecule and the zeolite

framework (see Fig. 3.3). Two of these are between a hydrogen atom of the ring and an oxygen atom of the framework, and these correspond to weak hydrogen bonds. The other two paths are somewhat unusual, and to our knowledge, unique. Essentially, these join both a sodium ion and an oxygen atom of the zeolite to the same point, that point being the center of a bond between two carbon atoms. These bonds lie in a mirror plane of the system, and if this symmetry is broken the van der Waals bonds go to one of the carbon atoms, and the real situation at room temperature probably corresponds to fluxionality of bonding to the alternative carbon atoms.

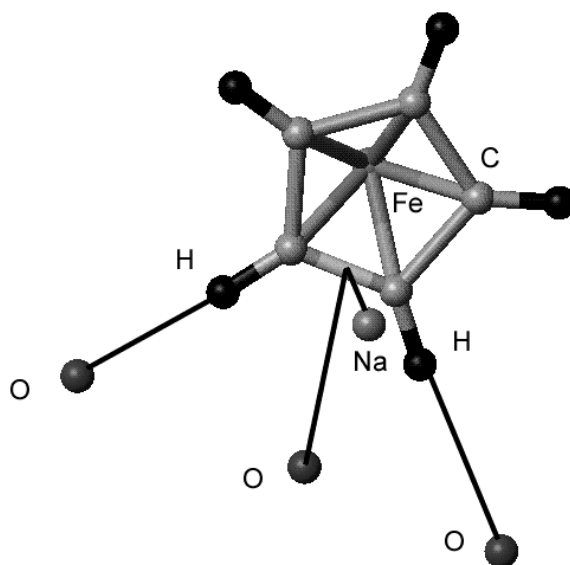


Figure 3.3 Interaction paths between a ferrocene- C_5H_5 ring and atoms in the zeolite framework. We find two paths from a hydrogen atom of the ring to an oxygen atom of the framework. There are also two paths from a sodium ion and an oxygen atom to the centre of a carbon-carbon bond in the ring.

3.3 Discussion

It seems clear that the unexpected position of the ferrocene molecule arises from an interaction of the carbon atoms of the ferrocene with the sodium ions and the oxygen atoms of the zeolite. It should be emphasised that many “ridges” in the electron density eventually flatten out, and hence disappear, but in the present case these ridges in the electron density actually continue as bond-paths. This makes it possible to express these arguments in more chemical terms. The energy associated with the formation of these new bonds more than compensates for the weakening of the hydrogen bond and the weaker interaction of the aromatic π -system with the sodium ion. The length of these bonds and the charge density in the bond critical points are collected in Table 3.1, and these allow a quantitative comparison of the different types of bonds.

	Path length (Å)	n (e/a_0^3) at bond critical point
H – O	2.63	0.0081
ring – O	3.49	0.0057
ring – Na	3.15	0.0057

Table 3.1 Path length and electron density n at the bond critical points for the interaction lines between a cyclopentadienyl ring and the zeolite framework.

For example, the electron density at the critical point of the strong covalent bond between two carbon atoms in benzene amounts to $0.33 e/a_0^3$, and of the bond between oxygen and hydrogen in a water molecule $0.39 e/a_0^3$.¹ An ionic bond has a rather lower value, for example $0.036 e/a_0^3$ in case of NaCl,¹ whilst hydrogen bonds normally have a values for the electron density between $0.001 - 0.035 e/a_0^3$.⁷ In the present case the hydrogen bond between the ferrocene hydrogen and the zeolite oxygen is also within this range, $0.0081 e/a_0^3$, and further, the C...O distance is comparable with that found in C-H...O hydrogen bonds.⁷ Similar values for the electron density at bond critical points are found in van der Waals molecules, for example $0.0077 e/a_0^3$ between Ar and HF and $0.0099 e/a_0^3$ between Ne and HF. These are comparable with the values we find for the interaction between the sodium and oxygen and the center of the CC bond of $0.0057 e/a_0^3$. However, we find distances that are greater than 3 Å, which is somewhat longer than the corresponding distances in Ne/HF (2.11Å) and Ar/HF (2.56Å).

Bonds between π -bondings and positive ions have been observed before,⁸ and a Bader analysis has been reported for hydrogen bonds with a π -bond.⁹ However, to our knowledge the binding between the π -cloud of an aromatic ring and an ion always involves the centre of the ring. In the present case the iron atom may well distort the π -cloud in such a way that two edge-bonds plus the involvement of an extra oxygen atom is energetically more favourable. We stress that these novel bonds should not be thought of as the primary interaction between the ferrocene and the zeolite. They are secondary to the main Coulomb and hydrogen bond interactions, which play the primary role in holding the ferrocene molecule in its place. It follows that rather long weak bonds are responsible for the displacement of the ferrocene molecule from the expected position.

All bonds between the ferrocene and the zeolite are weak and the bonding within the ferrocene itself is virtually unchanged from that of the isolated molecule. Inspection of Fig. 3.1 reveals a large 'free volume' on the exposed side of the ferrocene molecule which is an attractive site for any potential reactants. It is even conceivable that without the van der Waals bonds, the ferrocene would be held deeper in the zeolite cage where it would be less accessible to attack, and in this way very weak bonds could play a crucial role in catalysis.

References

1. R.F.W. Bader, *Atoms in Molecules. A Quantum Theory* (Clarendon Press, Oxford, 1990).

2. E. Kemner, A.R. Overweg, L. van Eijck, A.N. Fitch, E. Suard, I.M. de Schepper & G.J. Kearley, *Submitted*
3. B. Delley, *J. Chem. Phys.* **92** (1995) 508
4. P. Seiler & J.D. Dunitz, *Acta Crystallogr., Sect. B: Struct. Crystallogr. Cryst. Chem.* **35** (1979) 2020
5. E. Kemner, I.M. de Schepper, G.J. Kearley & U.A. Jayasooriya, *J. Chem. Phys.* **112** (2000) 10926
6. <http://www.nas.nasa.gov/Software/FAST/>
7. U. Koch & P.L.A. Popelier, *J. Phys. Chem.* **99** (1995) 9747
8. J.C. Ma & D.A. Dougherty, *Chem. Rev.* **97** (1997) 1303
9. I. Rozas, I. Alkorta & J. Elguero, *J. Phys. Chem. A* **101** (1997) 9457

Chapter 4. Molecular motion of ferrocene in a faujasite-type zeolite: a quasielastic neutron scattering study

E. Kemner, I.M. de Schepper, A.J.M. Schmets, H. Grimm, A.R. Overweg & R.A. van Santen, *J. Phys. Chem. B* **104** (2000) 1560

Abstract

We study the molecular motion of ferrocene $\text{Fe}(\text{C}_5\text{H}_5)_2$ locked up in the supercages of KY zeolite at temperatures $22 \text{ K} \leq T \leq 238 \text{ K}$ by means of quasielastic neutron scattering. The geometry of the motion is determined to be a 5-fold internal jump reorientation of the cyclopentadienyl C_5H_5 rings around the symmetry axis of the ferrocene molecule. We also obtain the mean residence time for these jumps as well as the activation energy for the process. We compare with NMR results on ferrocene in faujasite-type zeolites obtained by Overweg et al.¹, and with quasielastic neutron scattering results on pure ferrocene obtained by Gardner et al.²

4.1 Introduction

Recently Overweg et al.¹ have studied the molecular motions of ferrocene molecules $\text{Fe}(\text{C}_5\text{H}_5)_2$ locked up in the supercages of faujasite type zeolites by means of NMR spectroscopy. They concluded that for temperatures T below 225 K the ferrocene molecules have no translational freedom, the only motion being a, on the timescale of NMR experiments (\sim microseconds), very rapid internal jump rotation of the cyclopentadienyl C_5H_5 rings about their 5-fold axes. The actual value of the residence time τ of the rings at each site was determined by NMR to be much smaller than microseconds. Here we study at various temperatures the dynamics of ferrocene in a KY zeolite by means of quasielastic neutron scattering with which we can probe motions at timescales of the order of nanoseconds as well as the geometry of motion. For ferrocene in a KY zeolite it is found that the motion is consistent with an internal jump rotation of the rings about their 5-fold axes. The residence time $\tau(T) = 62 \text{ ps}$ at $T = 202 \text{ K}$. From the temperature dependence of $\tau(T)$ we determine an activation energy $E_a = 6.0 \text{ kJmol}^{-1}$ needed for the rotations. We compare our results with those obtained by Overweg et al., and with quasielastic neutron scattering results on pure ferrocene.²

4.2 Quasielastic neutron scattering

The theoretical incoherent dynamic structure factor $S(Q, \omega)$, i.e. the scattered neutron intensity as a function of momentum Q and energy ω transfer, is for a powder sample and five fold jump diffusion over a circle with radius R given by³

$$S(Q, \omega) = A_0(Q) \delta(\omega) + B(Q, \omega) \quad (4.1)$$

where the amplitude $A_0(Q)$ of the deltafunction $\delta(\omega)$ is the so-called elastic incoherent structure factor (EISF). $B(Q, \omega)$ is the quasielastic broadening

$$B(Q, \omega) = 2A_1(Q) \frac{1}{\pi} \frac{\lambda_1}{\omega^2 + \lambda_1^2} + 2A_2(Q) \frac{1}{\pi} \frac{\lambda_2}{\omega^2 + \lambda_2^2} \quad (4.2)$$

Here the amplitudes $A_\ell(Q)$ with $\ell = 0, 1, 2$, are given by

$$A_\ell(Q) = \frac{1}{5} + \frac{2}{5} j_0 \left(2QR \sin \frac{\pi}{5} \right) \cos \left(\frac{2\pi \ell}{5} \right) + \frac{2}{5} j_0 \left(2QR \sin \frac{2\pi}{5} \right) \cos \left(\frac{4\pi \ell}{5} \right) \quad (4.3)$$

with $j_0(x)$ the spherical Bessel function of zeroth order and the halfwidths λ_ℓ with $\ell = 1, 2$ are given by

$$\lambda_\ell = \frac{2}{\tau} \sin^2 \frac{\pi \ell}{5} \quad (4.4)$$

where τ is the mean residence time of the molecule at one site. We note that τ depends on T but not on Q , as we will need below. We will also need that $A_0(Q) + 2A_1(Q) + 2A_2(Q) = 1$ for all Q , due to the normalization of $S(Q, \omega)$, i.e. $\int S(Q, \omega) d\omega = 1$ for all Q . We remark that the neutron spectrum observed in experiments is given by Eq. (4.1) folded with the resolution function $R(Q, \omega)$ of the spectrometer.

4.3 Experiment

The sample consisted of ferrocene $\text{Fe}(\text{C}_5\text{H}_5)_2$ loaded into the supercages of dehydrated KY zeolite, prepared similar to the way described by Overweg et al.¹ There is one ferrocene molecule in each supercage. The sample was contained in an indium sealed aluminium flat plate sample chamber.

The neutron scattering measurements have been performed on the backscattering spectrometer BSS of the Forschungszentrum Jülich, Germany. First we used the Si(111) monochromator, resulting in an energy window $-15 \leq \omega \leq 15$ μeV and an energy resolution $\Delta\omega(Q) \approx 0.5$ μeV (HWHM), depending slightly on the momentum transfer Q . Second, the energy window was shifted to $-5 \leq \omega \leq 30$ μeV by using the $\text{Si}_{0.9}\text{Ge}_{0.1}$ (111) monochromator, resulting in an energy resolution $\Delta\omega(Q) \approx 1.2$ μeV , again slightly depending on Q . In both setups the momentum transfer Q ranged from 0.2 till 1.9 \AA^{-1} . We also performed in both setups measurements on vanadium to determine the full resolution function $R(Q, \omega)$ of the spectrometer, which, in good approximation, is of

Lorentzian shape with HWHM $\Delta\omega(Q)$. Measurements on pure KY zeolite show quasielastic spectra also proportional to $R(Q,\omega)$. From the intensity we conclude, as expected, that the scattering from KY zeolite is far less than from ferrocene. Its (small) contribution is accounted for in the modelling procedure.

4.4 Results

Below 100 K no quasielastic broadening in the spectra of ferrocene in KY zeolite is observed, i.e. the spectra $S(Q,\omega)$ are indistinguishable from the resolution function $R(Q,\omega)$. Above 140 K a broadening starts to appear which is very clear at $T = 202$ K. In Fig. 4.1a the spectra for momentum transfers $Q = 1.8 \text{ \AA}^{-1}$ at $T = 22$ and 202 K are plotted.

Clearly the central peak at $T = 202$ K is lower than the peak at $T = 22$ K, whereas the sidewings have more intensity at $T = 202$ K than at $T = 22$ K. This means that at 22 K, $B(Q,\omega) = 0$ and $A_0(Q) = 1$ while at 202 K $B(Q,\omega) > 0$ and $A_0(Q) < 1$ (cf. Eq. (4.1)). The spectra at $T = 202$ K were subsequently fitted with the 5-fold jump reorientational model according to Eqs. (4.1-4.4), where $\delta(\omega)$ is replaced by the normalized resolution function $R(Q,\omega)$. A_0 and τ were taken as two independent fit parameters while A_1 and A_2 were determined by the relations $A_0 + 2A_1 + 2A_2 = 1$ and $A_2(Q)/A_1(Q)$ as given by Eq. (4.3) and $R = 2.33 \text{ \AA}$ (i.e. the actual radius of the cyclopentadienyl rings⁴). The fits for $Q = 1.341$ and 1.883 \AA^{-1} are shown in Fig. 4.1b and 4.1c. We find that all the spectra $S(Q,\omega)$ can be fitted perfectly (like in Fig. 4.1) with the five fold jump model where τ depends on T , but not on Q , as theoretically predicted.

The fitted values for the area of the central line A_0 , the elastic incoherent structure factor, are represented in Fig. 4.2 as a function of Q , as well as theoretical EISF according to Eq. (4.3) with $R = 2.33 \text{ \AA}$. We also show (cf. Bée³) the theoretical predictions for 10-fold jumps. The agreement between theory and experiment is sufficient to ascertain that one indeed observes a five fold jump rotation of the cyclopentadienyl rings of ferrocene over a circle with radius $R = 2.33 \text{ \AA}$.

From the present experiment we find for the mean residence times $\tau(T) = 203$ ps (146 K), 121 ps (170 K), 71 ps (191 K), 62 ps (202 K) and 30 ps (238 K) as shown in Fig. 4.3. The dependence of the mean residence times $\tau(T)$ on temperature T is well described by an Arrhenius law:

$$\tau(T) = \tau_\infty \exp(E_a / k_B T) \quad (4.5)$$

with E_a being the activation energy for a jump reorientation, to be determined from the slope of the curve in Fig. 4.3. We find for E_a a value of $E_a = 6.0 \text{ kJmol}^{-1}$ and for the pre-exponential factor $\tau_\infty = 1.63$ ps.

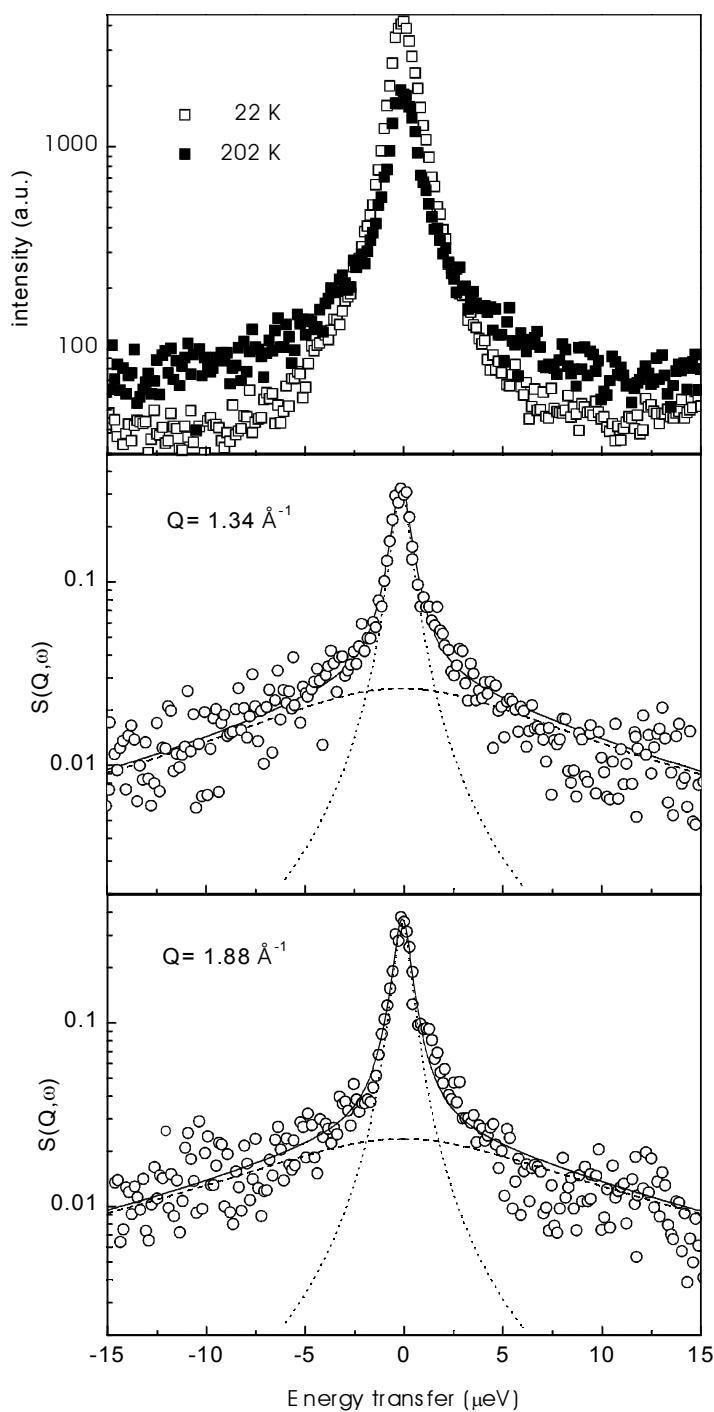


Figure 4.1 Top: Neutron scattering spectra on ferrocene $\text{Fe}(\text{C}_5\text{H}_5)_2$ in KY zeolite for momentum transfer $Q = 1.8 \text{ \AA}^{-1}$ at temperatures $T = 22 \text{ K}$ (open squares) and $T = 202 \text{ K}$ (solid squares) as measured on the BSS spectrometer in Jülich. Middle and bottom: Incoherent dynamic structure factors $S(Q, \omega)$ for momentum transfers $Q = 1.34 \text{ \AA}^{-1}$ and 1.88 \AA^{-1} of ferrocene in KY zeolite (open circles), together with fits according to a 5-fold jump reorientational model (as explained in the text). The dotted line gives the central peak of the fit, the dashed line gives the quasielastic broadening.

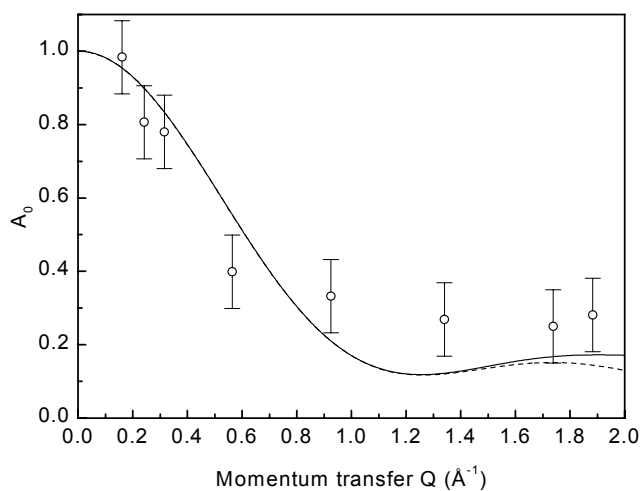


Figure 4.2 Fitted values for the area of the central line A_0 , the incoherent elastic structure factor EISF, for ferrocene in KY zeolite (open circles). The solid line gives the theoretical EISF according to a 5-fold jump reorientational model on a circle with radius $R = 2.33 \text{ \AA}$ (cf. Eq. (1)) and the dashed line for 10-fold jumps (cf. Bée³).

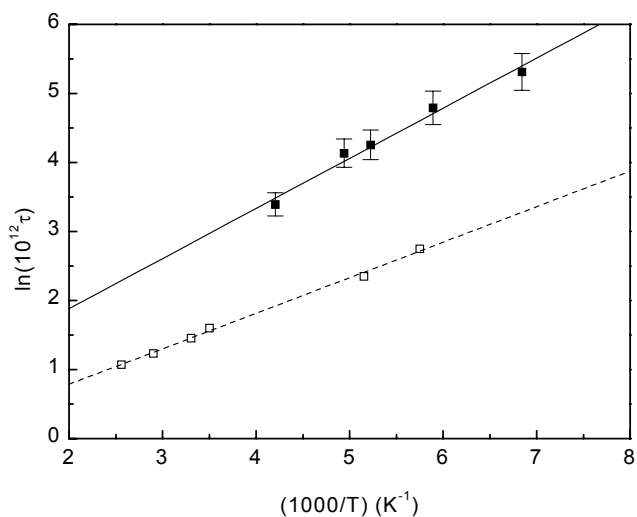


Figure 4.3 Residence times τ obtained from fits on neutron spectra with the 5-fold jump reorientational model as a function of temperature T for ferrocene in zeolite (solid squares, present work) and solid ferrocene (open squares, by Gardner et al.²). The solid line is a fit with an Arrhenius type law.

4.5 Discussion

We conclude that the geometry of the motion of the ferrocene molecules locked up in the supercages of KY zeolite is a 5-fold jump reorientation of the cyclopentadienyl C_5H_5 rings around the symmetry axis of the ferrocene molecule. Quasielastic neutron scattering spectra at different temperatures are perfectly fitted with such a model. Furthermore, the experimental elastic incoherent structure factor as a function of Q is in good agreement with the theoretical curve according to the 5-fold jump reorientational model. For small Q values we find that the radius of the circle is in agreement with the actual radius of the cyclopentadienyl rings (i.e. 2.33 Å), whereas for large values we find that the EISF tends to 1/5, where five is the number of sites used in the 5-fold model. These conclusions are consistent with those obtained by Overweg et al.¹

We are also able to determine the mean residence time of the ferrocene molecule at one site, being 62 ps at 202 K. From the temperature dependence of the mean residence time we determine the activation energy for a jump reorientation of the cyclopentadienyl rings of the ferrocene molecule around their 5-fold axes to be 6.0 kJmol⁻¹. The values of the mean residence times and for the activation energy are considerably larger than those obtained for pure ferrocene (as shown in Fig. 4.3), meaning that the ferrocene molecule is more tightly bound in the supercages of the zeolite than in the pure solid state.

According to Brot⁵ the frequency ω_{libr} of libration of the ferrocene molecule in its potential well is of the order of $\pi\tau_{\infty}^{-1}$, where $\tau_{\infty} = 1.63$ ps is the prefactor in Eq. (4.5). Thus one expects a libration peak in $S(Q,\omega)$ at $\omega \sim \omega_{\text{libr}} \sim 1.3$ meV, far outside the energy window of the BSS spectrometer used in the present work. We prepare experiments on the IRIS spectrometer of ISIS (UK) to confirm the existence of such a libration peak.

References

1. A.R. Overweg, H. Koller, J.W. de Haan, L.J.M. van de Ven, A.M. van der Kraan & R.A. van Santen, *J. Phys. Chem. B* **103** (1999) 4298
2. A.B. Gardner, J. Howard, T.C. Waddington, R.M. Richardson & J. Tomkinson, *Chem. Phys.* **57** (1981) 453
3. M. Bée, *Quasielastic Neutron Scattering* (Adam Hilger, Bristol, 1988)
4. D.R. Lide, *Handbook of Chemistry and Physics*, 79th ed. (CRC Press, Boca Raton, 1998)
5. C. Brot, *Chem. Phys. Lett.* **3** (1969) 319

Chapter 5. The vibrational spectrum of solid ferrocene by inelastic neutron scattering

E. Kemner, I.M. de Schepper, G.J. Kearley & U.A. Jayasooriya, *J. Chem. Phys.* **112** (2000) 10926

Abstract

We calculate the spectrum of internal vibrations of a single ferrocene $\text{Fe}(\text{C}_5\text{H}_5)_2$ molecule using *ab-initio* density functional theory (without free parameters) and compare this with inelastic neutron scattering data on ferrocene in the solid state at 28 K. Due to the good agreement we can assign each vibrational mode to each observed peak in the neutron spectrum and so remove ambiguities existing in the literature. There is also consistency between the calculated potential energy of a single ferrocene molecule for different orientations, φ , of the two cyclopentadienyl C_5H_5 rings with respect to each other, which shows a potential barrier of 0.9 kcal/mol, and electron diffraction, and between the calculated shallow minimum at $\varphi = 9$ degrees and X-ray diffraction.

5.1 Introduction

The ferrocene molecule $\text{Fe}(\text{C}_5\text{H}_5)_2$ has attracted much experimental and theoretical interest during the last forty years.¹⁻¹⁰ The interest lies in the unusual symmetric form of ferrocene (two identical cyclopentadienyl C_5H_5 rings on both sides of the Fe atom) while it is also the stablest member of the metallocene group, which in general has important catalytic properties. The vibrational frequencies of ferrocene have been calculated theoretically before and verified experimentally by Raman and infrared (IR) spectroscopy. We note that only the frequencies of the lines in the Raman and IR spectra can be accurately calculated, but not their relative intensities. So far reliable intensities could not be obtained from *ab-initio* calculations¹¹ since these are indirectly determined by subtle changes in the electron density caused by the vibrations of the nuclei. Therefore, due to a lack of a complete theoretical spectrum, ambiguities easily occur in the assignment of the character of the vibrational mode to the lines observed in the experimental spectra, as discussed e.g. in Ref. 1.

Here we show for the first time that a full comparison can be made between spectra for ferrocene obtained from inelastic neutron scattering (INS) and theoretical *ab-initio* calculations, i.e. including relative intensities. Since neutrons probe the vibrations of the nuclei directly, a theoretical calculation of intensities in the corresponding INS spectrum is feasible. Thus, since both agree, we can unambiguously assign the character of the vibrations to each line in the INS spectrum, as we will do in this paper for the most pro-

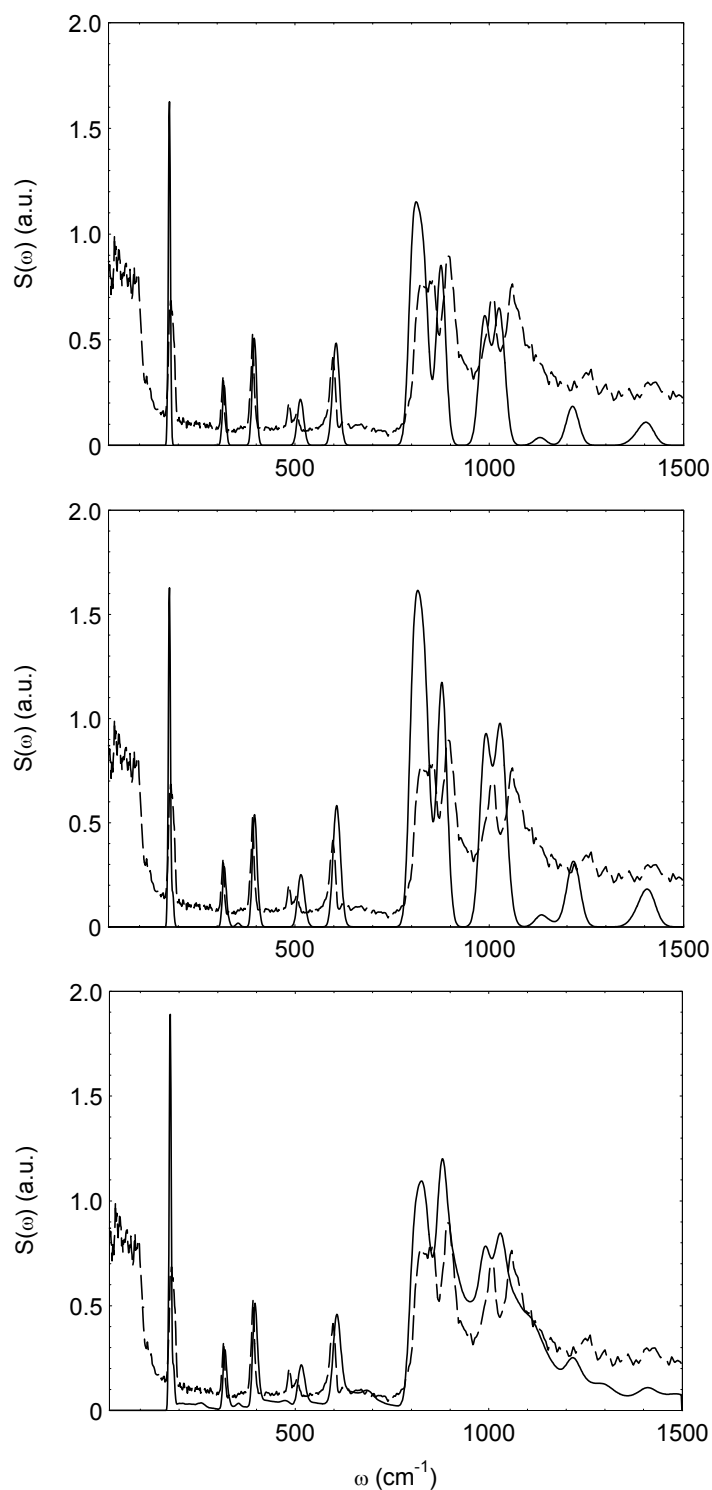


Figure 5.1 Inelastic neutron scattering spectrum $S(\omega)$ for solid ferrocene at 28 K (dashed line) compared with DFT calculations on a single ferrocene molecule (solid line) taking into account (a) only the fundamental vibrational modes, (b) the fundamental modes plus overtones and combinations and (c) fundamental modes, overtones and combinations and phonons, as explained in the text.

minent lines. As a result we can remove some ambiguities existing in the literature.

5.2 Experiment and results

The INS neutron spectrum, i.e. the scattered neutron intensity, of ferrocene is obtained as a function of the energy transfer ($S(\omega)$), using the Time Focused Crystal Analyser (TFXA) spectrometer at ISIS, UK.¹² This spectrometer has an indirect geometry and uses a pyrolytic graphite (002) crystal to select a final neutron energy of 24 cm^{-1} . We note that the momentum transfer, Q , is not constant, but varies as $\sqrt{\omega}$. For simplicity we will use $S(\omega)$ to mean $S(Q, \omega)$. This spectrometer has an energy resolution of 2 - 4%, depending slightly on the energy transfer. The accessible energy (ω) range is 20 - 4000 cm^{-1} . The powdered ferrocene sample was contained in an aluminium sample holder and cooled to 28 K. The spectrum of each detector tube is converted to $S(\omega)$ using standard programmes. The individual spectra are then added to provide a single spectrum. The result for $S(\omega)$ is shown in Fig. 5.1.

The calculations are carried out using density functional theory on a single ferrocene molecule with the module Dmol³ of the program Cerius^{2,13}. We use the local density approximation, Perdew Wang functionals, the DND basis set and an atomic cutoff radius of 4.95 Å. To determine the shape of the molecule from first principles we calculate the energy $E(\varphi)$ of ferrocene for different orientations φ of the two C_5H_5 rings with respect to each other. Here $\varphi = 0$ refers to the state where the atoms of the upper C_5H_5 -ring are just on top of the corresponding atoms in the lower ring. This is called the 'prismatic'⁴ or 'eclipsed' orientation. The angle $\varphi = 36$ degrees refers to the 'antiprismatic' or 'staggered' orientation, where the atoms in the upper ring are just between the corresponding atoms in the lower ring. First we optimize the positions of the atoms in the eclipsed orientation ($\varphi = 0$). We find for the bond lengths: 1.423 Å (CC), 1.093 Å (CH) and 2.027 Å (FeC). We find the H atoms to be tilted 1.6° from the C_5 ring towards the Fe atom. These results agree with those in the literature.^{1,2} We then calculate the energy $E(\varphi)$ for different angles φ using these values for the bond lengths and CH tilt, using the DFT program as discussed above.

The result for $E(\varphi)$ is shown in Fig. 5.2. The energy is clearly lower for the eclipsed ($\varphi = 0$) than for the staggered orientation ($\varphi = 36$ degrees), although the potential barrier of 0.9 kcal/mol is small, being virtually the same as has been derived before from electron diffraction (0.9 ± 0.3 kcal/mol) on ferrocene in the gas phase.³ There are several shallow minima in $E(\varphi)$ which are grouped around $\varphi = 0$ and extend up to about 12 degrees, which could be artefacts of the numerical calculations. The overall shape of the potential barrier closely resembles a cosine, as shown in Fig. 5.2. For further calculations we take the rings of the ferrocene molecule as rotated by 9 degrees from the eclipsed orientation, to agree with X-ray diffraction on the low temperature phase of solid ferrocene.² We optimize in this orientation the geometry of the ferrocene molecule again, but find no differences in bond lengths and CH tilt from the eclipsed configuration as given above.

Using the so determined shape of ferrocene we calculate the vibration frequencies of the normal modes and the displacements of all the atoms for each of these modes. These results are taken as input for the program CLIMAX, which converts the data to a theoretical inelastic neutron scattering spectrum $S(\omega)$.¹⁴ CLIMAX has been devised to include the overtones and combinations (due to multiple excitations) and external lattice modes (phonons) in the calculation of the neutron scattering spectrum. Thus we calculate $S(\omega)$ in three steps.

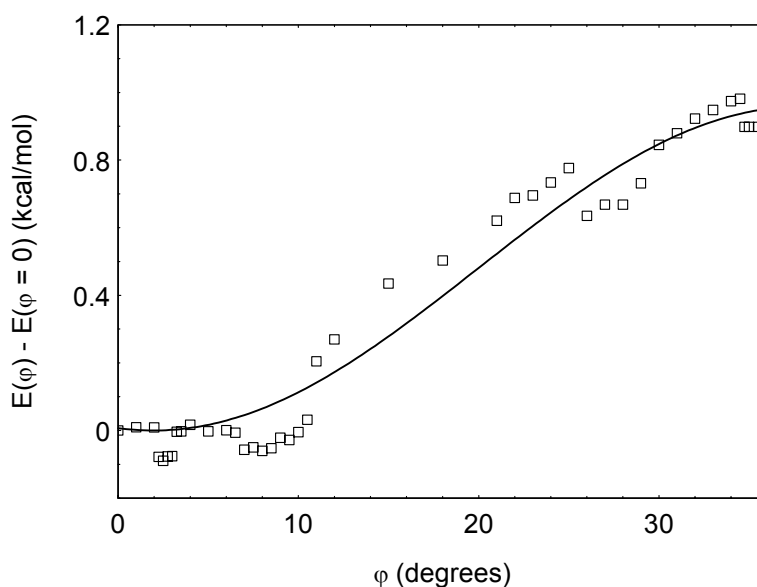


Figure 5.2 Internal potential $E(\varphi)$ for rotation of the two C_5H_5 rings in the ferrocene $Fe(C_5H_5)_2$ molecule with respect to each other according to DFT calculations as a function of orientation φ where $\varphi = 0$ corresponds to the eclipsed orientation (open squares). Also shown is a fit with $E(\varphi) = a(1 - \cos(\pi(\varphi - b)/36))$, with amplitude $a = 0.47$ kcal/mol and phase $b = 1.96$ degrees (solid line).

First we treat ferrocene as an isolated purely harmonic molecule. This yields the fundamental vibrational frequencies ω_n and their relative intensities. Here $n = 1, \dots, 34$, where we apply the nomenclature commonly used in the literature.⁵ Using the resolution of the spectrometer we so obtain the fundamental spectrum $S_f(\omega)$, as shown in Fig. 5.1a.

Next we include the effect of multiple excitations of ferrocene induced by the incoming neutrons. This yields the spectrum $S_{f,o}(\omega)$ shown in Fig. 5.1b. It consists of the fundamental modes ω_n , its overtones, i.e. linear combinations of one ω_n , and their combinations, i.e. linear combinations of different fundamental modes. We observe that there are only minor differences between $S_f(\omega)$ and $S_{f,o}(\omega)$. Virtually none of the very many overtones and combinations can be observed directly (except maybe the one at $\omega = 350 \text{ cm}^{-1}$). In practice, the main effect of multiple excitations is that the intensities increase with increasing ω (cf. Figs. 5.1a and 5.1b), due to the increasing number of overtones and combinations.

Finally we incorporate the effect of the lattice vibrations (phonons) in solid ferrocene. We assume that the phonon spectrum is given by the experimental $S(\omega)$ with $0 \leq \omega \leq 150 \text{ cm}^{-1}$ (cf. Fig. 5.1). This phonon spectrum is convoluted¹⁴ with the theoretical result $S_{f,o}(\omega)$ to yield $S_{f,o,p}(\omega)$ as shown in Fig. 5.1c. One sees that the convolution procedure causes significant sidewings in $S_{f,o,p}(\omega)$ to the right of each fundamental peak in $S_{f,o}(\omega)$ (cf. Figs. 5.1b and 5.1c), as has been discussed before.¹⁴

On the basis of the good agreement between the theoretical and experimental spectra in Fig. 5.1c we can, with some confidence, determine the vibrational character of each peak in the experimental spectrum $S(\omega)$.

We start with the six sharp experimental peaks visible at 180, 315, 391, 485, 504 and 598 cm^{-1} . In Table 5.1 we compare these values with the present theoretical calculations, from which we derive its character and the labeling according to Ref. 4. In Fig. 5.3 we give the graphical representations of these vibrational modes: ring-metal-ring bend combined with antisymmetric ring tilt (180 cm^{-1}), metal-ring stretch (315 cm^{-1}), symmetric ring tilt (391 cm^{-1}), metal-ring stretch with oscillating Fe (485 cm^{-1}), antisymmetric ring tilt combined with ring-metal-ring bend (504 cm^{-1}) and out of plane ring distortion (combined with CH bending, symmetric and antisymmetric) (598 cm^{-1}). For all these six modes it appears that each H-nucleus moves in phase with its nearest C-nucleus.

Next, one sees a strong and very broad peak in the measured INS spectrum between ~ 820 and $\sim 860 \text{ cm}^{-1}$. We attribute this peak to the contributions of six vibrational modes (also represented in Fig. 5.3), which are in order of increasing energy in-phase CH bending perpendicular to the ring plane (14), in- and out-of-phase CH bending perpendicular to the ring plane with all the carbon atoms of one ring moving in phase (2 and 9), out-of-phase ring distortion in the ring plane (33), out-of-phase CH bending perpendicular to the ring plane (19), and in-phase ring distortion in the ring plane (27). For these modes it appears that in most cases the H-nuclei move out of phase with their nearest C-nucleus, but that the CH bond length is fixed.

Then, we assign the sharper isolated peak near 900 cm^{-1} to an in-phase CH bending perpendicular to the ring plane and an out-of-plane ring distortion combined with CH bending. Finally, we attribute the experimental peak at 1010 cm^{-1} to two modes, being, respectively, out- and in-phase CH bending in the ring plane and we assign the last clearly visible peak at 1060 cm^{-1} again to CH bending in the ring plane (cf. Table 5.1 and Fig. 5.3).

Present			Ref. 4	
INS (cm^{-1})	DFT ($\varphi = 9^\circ$) (cm^{-1})	Mode #	IR and Raman (cm^{-1})	Mode #
$\lesssim 20$	9	6	44	6
180	177	22,21	179	22
315	318	4	309	4
391	395	16	389	16
485	511	11	478	11
504	519	21,22	492	21
598	606	28,34	569	34
			597	28
820 – 860	800 – 840	2,9,14,19,27,33	814 – 855	2,9,14,19
900	876	14,19,25,31	885	33
			897	27
1010	988	13,18	998	13
			1005	18
1060	1026	24,30	1055	31
			1058	25

Table 5.1 The frequencies of the normal modes and their assignment for the present INS experiment and DFT calculations, and the frequencies and assignments from IR and Raman experiments taken from the literature.

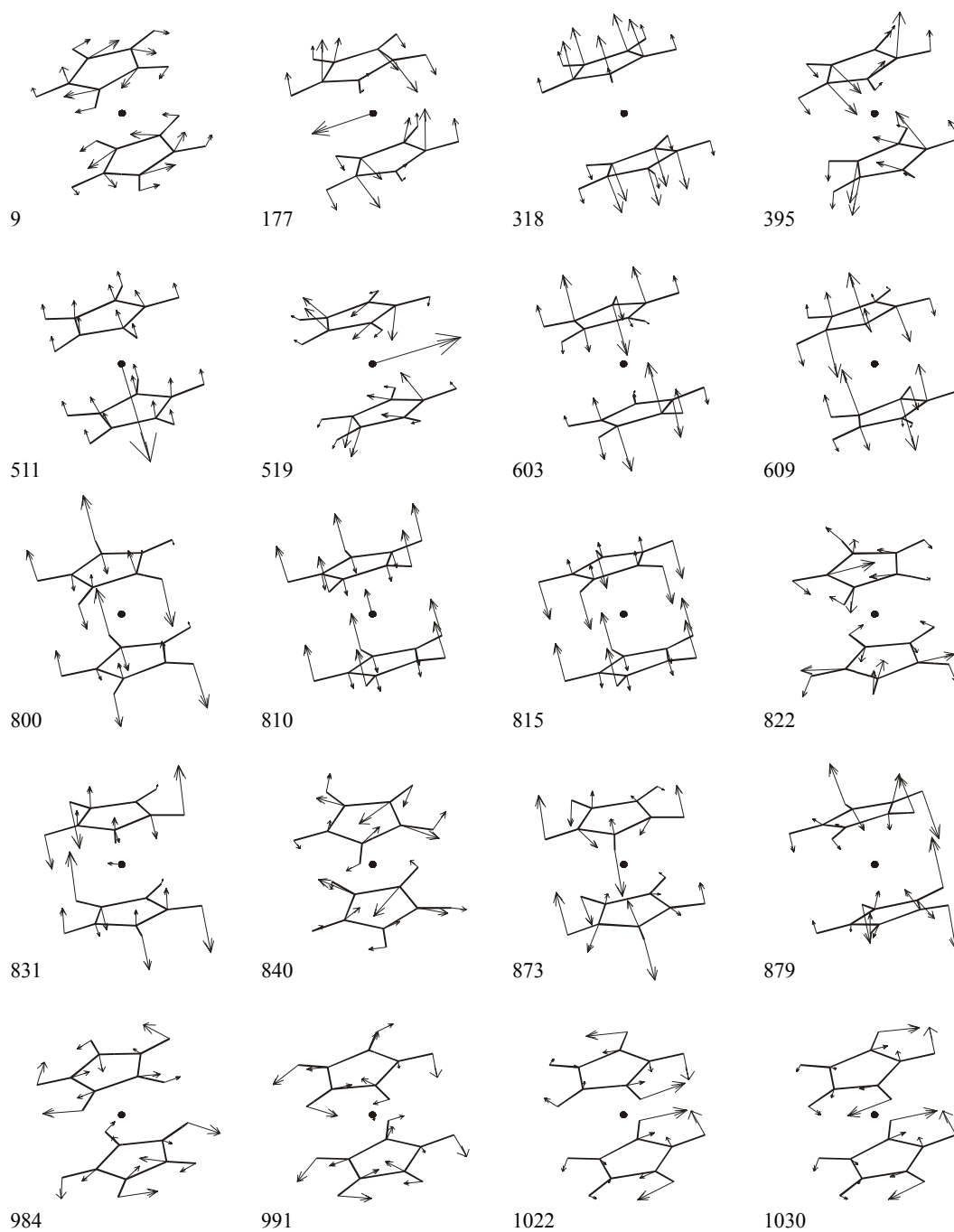


Figure 5.3 Graphical representation of the vibrational modes of ferrocene as calculated by DFT. The arrows give the direction and amplitude of the motion of the atoms, the numbers give the calculated frequencies in cm^{-1} .

5.3 Discussion

By means of density functional theory we have identified the vibrational character of the most prominent peaks in the INS spectrum of solid ferrocene at 28 K. We start our comparison with results given in the literature with the lowest lying eigenmode, the so called torsion mode (number 6 in Ref. 4). Here the two C_5H_5 rings oscillate in plane, but out of phase with each other with frequency ω_6 around the equilibrium position at $\varphi = 9^\circ$ (cf. Fig. 5.3). From our DFT calculations with $\varphi = 9^\circ$ we find $\omega_6 = 9 \text{ cm}^{-1}$ and an intensity as large as that of the peak at 180 cm^{-1} (see Fig. 5.1a). Therefore this torsion mode falls outside the region $\omega \gtrsim 20 \text{ cm}^{-1}$ covered by our neutron spectrometer. We note however, that our result $\omega_6 = 9 \text{ cm}^{-1}$ is extremely sensitive to the equilibrium position φ . By varying φ between 6 and 10 degrees we estimate the uncertainty in $\omega_6 = 9 \text{ cm}^{-1}$ to be at least 100%, i.e. $0 \lesssim \omega_6 \lesssim 20 \text{ cm}^{-1}$. Since we do not see a sharp peak with the correct intensity in the experimental $S(\omega)$ for $\omega > 20 \text{ cm}^{-1}$ we conclude that the torsion mode frequency must indeed lie in the range $0 \lesssim \omega_6 \lesssim 20 \text{ cm}^{-1}$. In IR spectra a very weak line has been observed at 44 cm^{-1} which has been tentatively attributed to the torsion mode,⁷ while Howard et al.⁸ suggested that a peak at 56 cm^{-1} in their inelastic neutron spectrum (at room temperature) might be due to torsion. Our present experiment does not confirm these two expectations. Gardner et al.⁹ find in their inelastic neutron spectrum at 5 K a peak at 22 cm^{-1} , and our calculations lend support to their assignment of this peak to the torsion mode.

From our DFT calculations it follows that only the torsion mode frequency ω_6 is sensitive to the equilibration position φ due to the several local minima in the potential barrier as described above. All other frequencies do not change more than a few percent when φ is varied between 0 and 12 degrees.

The modes seen in the INS spectrum at 180, 315, 391, 485 and 504 cm^{-1} agree with those given in the literature (see Table 5.1), including their character. We note that the modes at 180 and 504 cm^{-1} are both linear combinations of mode numbers 21 and 22.⁴ This has been suggested before.^{1,6}

In our INS spectrum we do not find a peak at 569 cm^{-1} as reported for IR and Raman spectra, where it is attributed to mode number 34 (cf. Table 5.1 and Ref. 4). Instead we find that the modes 28 and 34 yield indistinguishable peaks at 598 cm^{-1} . This confirms the assumption of Lippincott,⁵ based on their character, that both modes have the same frequency. The peak at 569 cm^{-1} , alluded to above, is only actually present in the spectrum shown by Winter et al.,¹⁰ who assigned it to mode 34. However this peak is rather weak and there are several other weak peaks in their IR spectrum, which were left unassigned. It seems likely that these peaks arise from impurities.

The broad INS peak between 820 and 860 cm^{-1} agrees with IR and Raman spectra, including their main character. However, we find that the parallel ring-distortion modes 27 and 33 are included in this INS peak, contrary to what is conjectured for IR and Raman spectra (cf. Table 5.1). Also, we find that the INS peak at 900 cm^{-1} is certainly not due to these modes 27 and 33. Instead, the character is given by orthogonal CH

bends with the hydrogens moving out of phase (14,19,25,31, cf. Table 5.1 and Fig. 5.3). The INS peak at 1010 cm^{-1} is due to parallel CH bends (13,18) like in IR and Raman spectra. The INS peak at 1060 cm^{-1} is due to parallel CH bends (24,30) and not to orthogonal CH bends (25,31) as suggested for IR and Raman spectra. In conclusion we add a new character to the peaks in the spectrum at 900 and 1060 cm^{-1} . We finally note that we have calculated the fundamental modes of an isolated ferrocene molecule which appear to agree reasonably well with those observed in solid ferrocene. Differences might be due to the fact that in solid ferrocene the molecules are not isolated, but interact with each other. Clearly, the low-frequency modes, such as the torsion, will be the most affected. To calculate this interaction from first principles is a formidable task but seems feasible in the near future.

References

1. A. Bérces, T. Ziegler & L. Fan, *J. Phys. Chem.* **98** (1994) 1584
2. P. Seiler & D. Dunitz, *Acta Cryst.* **B35** (1979) 2020
3. A. Haaland & J.E. Nilsson, *Acta Chem. Scand.* **22** (1968) 2653
4. J.S. Bodenheimer & W. Low, *Spectrochim. Acta* **29A** (1973) 1733
5. E.R. Lippincott & R.D. Nelson, *Spectrochim. Acta* **10** (1958) 307
6. E. Diana, R. Rossetti, P.L. Stanghellini & S.F.A. Kettle, *Inorg. Chem.* **36** (1997) 382
7. F. Rocquet, L. Berreby & J.P. Marsault, *Spectrochim. Acta* **29A** (1973) 1101
8. J. Howard, T.C. Waddington & C.J. Wright, *J. Chem. Soc. Faraday Trans. 2* **72** (1976) 513
9. A.B. Gardner, J. Howard, T.C. Waddington, R.M. Richardson & J. Tomkinson, *Chem. Phys.* **57** (1981) 453
10. W.K. Winter, B. Curnutte, Jr. & S.E. Whitcomb, *Spectrochim. Acta* **12** (1959) 1085
11. K. Palmo & S. Krimm, *J. Comput. Chem.* **19** (1998) 754
12. <http://www.isis.rl.ac.uk/CrystalAnalysers/tfxa.htm>
13. B. Delley, *J. Chem. Phys.* **92** (1990) 508
14. G.J. Kearley, *Nucl. Instr. Meth. A* **354** (1995) 53

Chapter 6. Ferrocene-zeolite interactions measured by inelastic neutron scattering

E. Kemner, A.R. Overweg, U.A. Jayasooriya, S.F. Parker, I.M. de Schepper & G.J. Kearley, *Submitted to Appl. Phys. A*

Abstract

The measured inelastic neutron scattering (INS) vibrational spectrum of ferrocene $\text{Fe}(\text{C}_5\text{H}_5)_2$ in the supercages of KY zeolite is compared with that of solid ferrocene. Only small differences between these spectra are observed. It is shown that these differences are compatible with those calculated by *ab-initio* calculations taking account only of the geometry of the ferrocene and ignoring the molecular environment. We conclude that the ferrocene-zeolite interactions are rather weak, and comparable with the intermolecular interactions in solid ferrocene.

6.1 Introduction

Zeolites are crystalline aluminosilicates with a three-dimensional open framework structure of channels and cavities of molecular dimensions. They can act as molecular sieves, making catalytic centres in the interior of the zeolite only accessible to molecules of the correct size. Such catalytic centres, especially clusters of transition metals, can be incorporated in zeolites by vapour phase insertion of volatile metal compounds, such as ferrocene, $\text{Fe}(\text{C}_5\text{H}_5)_2$. This molecule consists of an iron atom 'sandwiched' between two identical parallel cyclopentadienyl, C_5H_5 , rings.

The interaction between the ferrocene and the zeolite can be estimated by comparing the vibrational spectra of pure ferrocene with that of ferrocene in the zeolite. INS has the advantage that the spectrum of the ferrocene molecule is much stronger than that of the zeolite. Further, we have recently determined the crystal structure of ferrocene in a Y-type zeolite (see Fig. 6.1),¹ so that we are now in a position to make a quantitative analysis of the spectra, by combining *ab-initio* calculations with INS spectra.

In the zeolite, the ferrocene molecules are located just above a line joining two neighbouring cations on the surface of the supercage, with the two cyclopentadienyl rings in the 'eclipsed' orientation. The cyclopentadienyl rings are orientated towards the cations in the zeolite supercage. In a previous study² we calculated the spectrum of internal vibrations of a single ferrocene $\text{Fe}(\text{C}_5\text{H}_5)_2$ molecule (i.e. in the gas phase) using *ab-initio* density functional theory (without free parameters). The minimum-energy configuration of an isolated ferrocene molecule has the rings rotated by 9° from the eclipsed orientation, and our calculated INS spectrum for this orientation compares well with the measured INS spectrum of ferrocene in the solid state at 28 K.² In the present paper we extend and compare this work with an analysis of the INS spectrum of

ferrocene in KY zeolite at 20 K. It transpires that both in solid ferrocene, and in ferrocene in KY zeolite, the intermolecular interactions are very weak. For the most part, the differences between the INS spectra of the two materials are compatible with the geometric differences of the ferrocene molecule in the two environments.

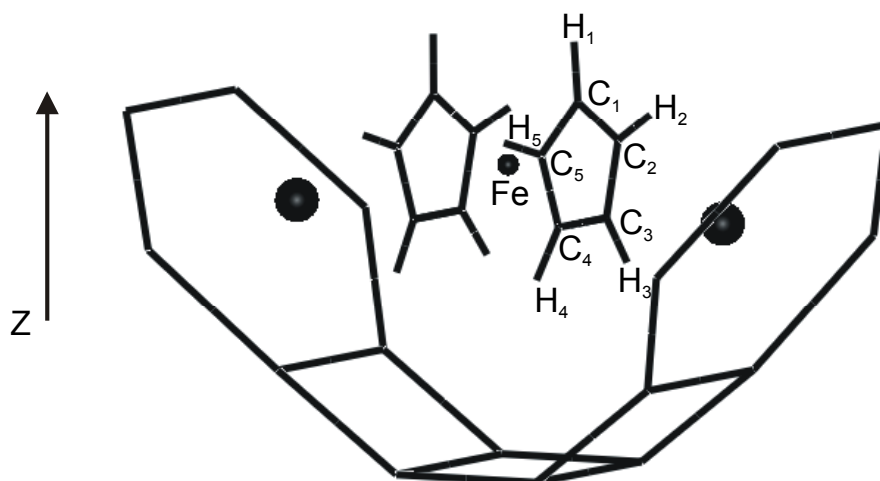


Figure 6.1 A ferrocene molecule in a zeolite Y supercage. For clarity we show only the part of the zeolite that is nearest to the ferrocene molecule. The spheres are the positions of the cations.

6.2 Experiment

The INS neutron spectrum $S_z(\omega)$, of ferrocene in KY zeolite was obtained using the TOSCA spectrometer at ISIS, UK.³ Although the momentum transfer Q on TOSCA is not constant but varies as $\sqrt{\omega}$, for simplicity we will use $S(\omega)$ to mean the cut taken through (Q, ω) -space by this spectrometer. The energy resolution can be taken as about 2% of the energy transfer over the range studied in this paper (100 – 1500 cm^{-1}). The ferrocene in KY zeolite powder sample was contained in an aluminium sample holder sealed with indium and cooled to 20 K. We also measured the INS vibrational spectrum of bare, dehydrated, KY zeolite at 20 K. The resulting spectra for the bare zeolite and for ferrocene in KY zeolite are shown in Fig. 6.2, from which it is clear that the spectrum of bare KY zeolite is almost flat compared with that of ferrocene in KY zeolite.

6.3 Computations

For the theoretical INS spectra we first take the spectrum $S_{t,s}(\omega)$ as obtained before² for gas-phase ferrocene with the rings rotated by 9° . Energy calculations were performed

using Dmol³ as part of the suite Cerius^{2,4} with the local density approximation, Perdew Wang functionals,⁵ the DND basis set⁴ and an atomic cutoff radius of 5.5 Å. After optimizing the geometry, the full force-constant matrix was calculated in Cartesian space by the finite difference method. The results were taken as input for the program CLIMAX, which converts the data to theoretical inelastic neutron scattering spectra $S(\omega)$.⁶ In the present study we first calculate in the same manner $S_{t,e}(\omega)$ for gas phase ferrocene in the eclipsed orientation. Then we take from Ref. 1 the geometry optimized result for a fragment of the zeolite supercage containing one ferrocene molecule, as shown in Fig. 6.1. We calculate $S_{t,z}(\omega)$ for only the ferrocene molecule in this geometry, without the zeolite framework. The various bond lengths and the tilt of the H atoms from the cyclopentadienyl ring towards the Fe atom are given in Table 6.1 for ferrocene in its ‘zeolite’ geometry and for ferrocene in the gas phase.

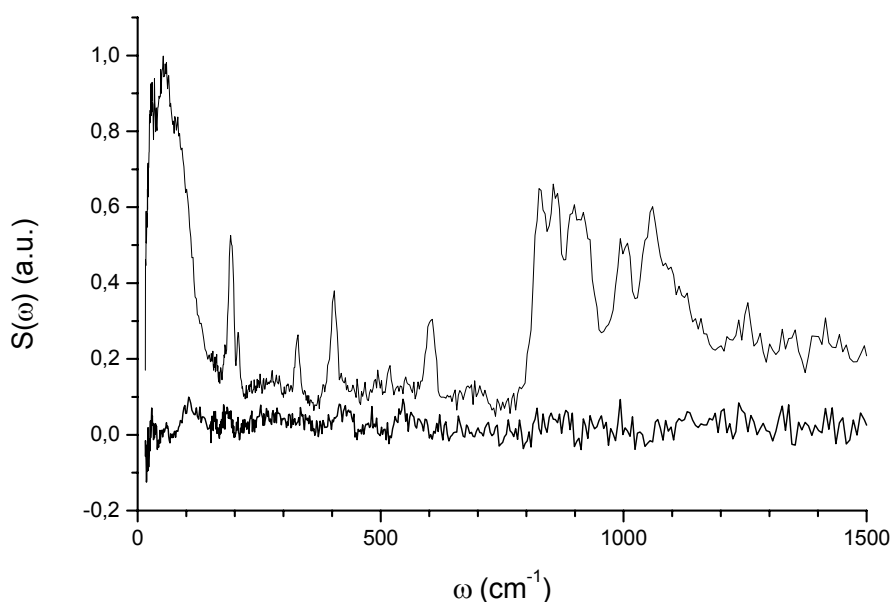


Figure 6.2 Inelastic neutron scattering spectrum $S(\omega)$ for dehydrated KY zeolite at 20 K (bottom line) and inelastic neutron scattering spectrum $S_z(\omega)$ for ferrocene in KY zeolite at 20 K (top line).

6.4 Results and discussion

In Fig. 6.3 we compare the INS spectrum, $S_z(\omega)$, of ferrocene in KY zeolite with that calculated for the minimum-energy configuration of the gas-phase molecule. The agreement is good, and it follows that the character of the vibrations is the same for ferrocene in the gas-phase, the pure solid. Frequency data are collected in Table 6.2.

	ferrocene in zeolite	Gas-phase ferrocene
C ₁ C ₂ , C ₅ C ₁	1.425 Å	all CC 1.423 Å
C ₂ C ₃ , C ₄ C ₅	1.429 Å	
C ₃ C ₄	1.431 Å	
C ₁ H ₁ , C ₂ H ₂ , C ₅ H ₅	1.093 Å	all CH 1.093 Å
C ₃ H ₃ , C ₄ H ₄	1.095 Å	
C ₁ Fe	2.025 Å	all CFe 2.027 Å
C ₂ Fe, C ₃ Fe, C ₄ Fe, C ₅ Fe	2.024 Å	
H ₁ tilt	2.3°	all H tilt 1.6°
H ₂ , H ₅ tilt	2.5°	
H ₃ , H ₄ tilt	3.7°	

Table 6.1 Bond lengths and H tilt (cf. Fig 6.1) according to DFT calculations for ferrocene in zeolite Y and ferrocene in the gas phase.

INS ferrocene in KY zeolite (cm ⁻¹)	INS solid ferrocene (cm ⁻¹)	DFT single ferrocene 9° (cm ⁻¹)	DFT single ferrocene 0° (cm ⁻¹)	DFT ferrocene as in zeolite (cm ⁻¹)	Mode #
~30	≤ 20	9			6
192 (207)	180	177	160	176	22,21
330	315	318	316	319	4
405	391	395	386	395	16
(494)	485	511	490	509	11
(519)	504	519	505	520	21,22
606	598	606	593	598	28,34
830 - 860	820 - 860	800 - 840	800 - 840	790 - 830	2,9,14,19,27,33
900	900	876	870	860	14,19,25,31
1000	1010	988	999	993	13,18
1060	1060	1026	1040	1034	24,30

Table 6.1 The frequencies of the normal modes for the INS experiment on ferrocene in KY zeolite, the INS experiment on solid ferrocene, according to DFT calculations on gas phase ferrocene with the rings rotated 9° from the eclipsed orientation, according to DFT calculations on a single eclipsed ferrocene molecule, according to DFT calculations on ferrocene molecule in the geometry as found in zeolite and the normal mode assignments labeled according to Ref. 7.

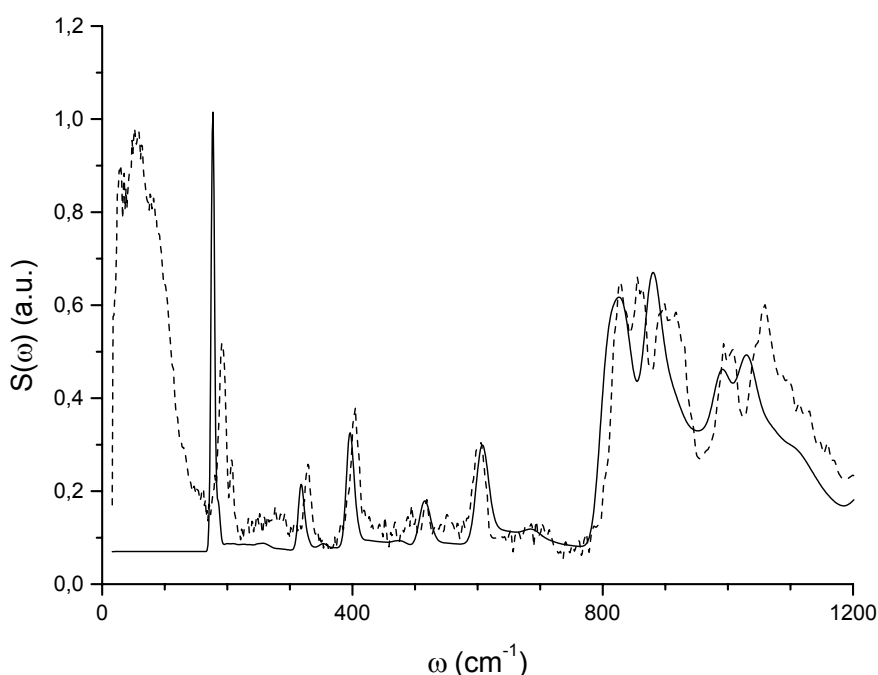


Figure 6.3 Inelastic neutron scattering spectrum $S_z(\omega)$ for ferrocene in KY zeolite at 20 K (dashed line) compared with $S_{t,s}(\omega)$ according to DFT calculations on a single ferrocene molecule with rings rotated by 9° (solid line).

A comparison of the experimental INS spectra of ferrocene in the zeolite, $S_z(\omega)$, with that of solid ferrocene, $S_s(\omega)$, (see Fig. 6.4 and Ref. 2) reveals that the peaks found at 192, 330 and 405 cm^{-1} arise about 14 cm^{-1} higher in energy in $S_z(\omega)$. These modes involve motions of the cyclopentadienyl C_5H_5 rings as a whole with respect to the iron atom (see Ref. 2), namely ring-metal-ring bend combined with antisymmetric ring tilt (192 cm^{-1}), metal-ring stretch (305 cm^{-1}) and symmetric ring tilt (405 cm^{-1}). Such a shift has also been observed for benzene in NaY zeolite, and more general in the formation of metal- π complexes.⁸ The central question is: how much of this shift is caused by the change in geometry of the ferrocene as a result of incorporation in the zeolite, and how much is due to interaction of the cyclopentadienyl rings with the zeolite?

The two peaks at 485 and 504 cm^{-1} in $S_s(\omega)$ appear to correspond to the weaker peaks at 494 and 519 cm^{-1} in the spectrum of ferrocene in zeolite, $S_z(\omega)$, also corresponding to an upward shift of about 12 cm^{-1} . These are attributed to a metal-ring stretch with oscillating Fe and an antisymmetric ring tilt combined with ring-metal-ring, bend, respectively. The final feature for which we can clearly see a difference between solid ferrocene, $S_s(\omega)$, and ferrocene in KY zeolite, $S_z(\omega)$ is the out of plane ring distortion, combined with CH bending, symmetric and antisymmetric, which arise at 598 cm^{-1} and 606 cm^{-1} , respectively. It follows from the rather weak interaction between the ferrocene and the zeolite that the main spectral consequences occur in the low

frequency modes that explore the softer directions on the potential-energy surface, and correspondingly, spectral features at higher frequencies are indistinguishable for the two materials.

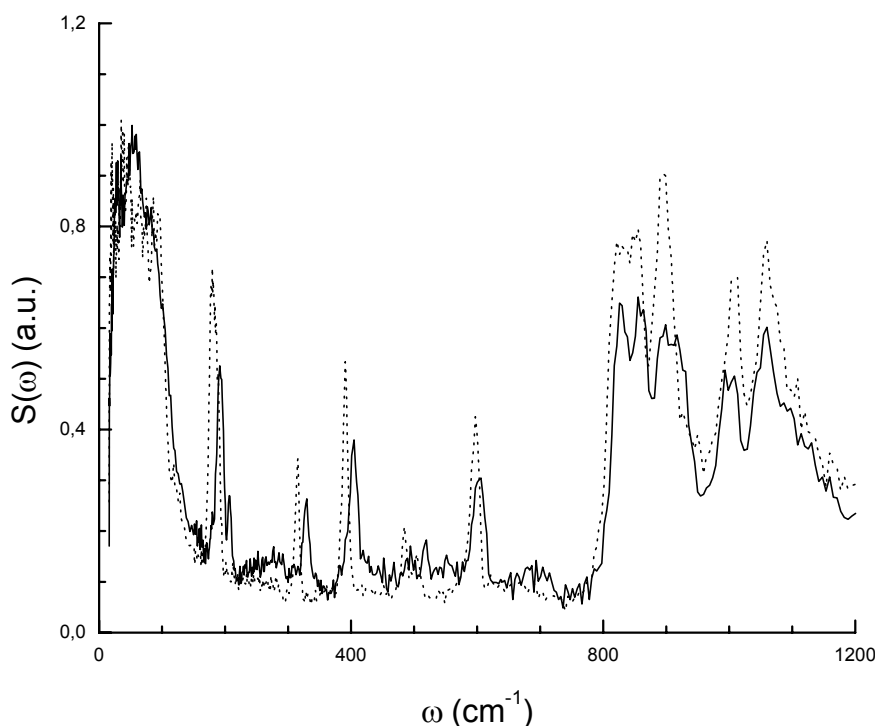


Figure 6.4 Inelastic neutron scattering spectrum $S_z(\omega)$ for ferrocene in KY zeolite at 20 K (solid line) compared with the inelastic neutron scattering spectrum $S_s(\omega)$ for solid ferrocene (dashed line).

The torsional mode in which the two C_5H_5 rings undergo an out of phase libration was not assigned in our INS spectra of solid ferrocene. Since the calculated frequency for an isolated ferrocene molecule is only 9 cm^{-1} , and our data begin at 20 cm^{-1} , we concluded that this mode arises somewhere below this value. It is expected that the torsion mode is sensitive to the environment of the ferrocene molecule. However, also in $S_z(\omega)$ we can not attribute a peak to this mode. It should be noted that the density of states also arises in the low-frequency region, which makes detailed analysis difficult.

In solid ferrocene the dihedral angle between the two rings is 9° whilst when this molecule is in KY zeolite the corresponding angle is 0° . Intuitively, one might expect that this change is responsible for the spectral differences between the two materials, but this is not the case, which we show as follows. The calculated INS spectra of the gas-phase molecule constrained to have eclipsed cyclopentadienyl rings, $S_{t,e}(\omega)$, and the calculated INS spectrum of ferrocene with the exact geometry found in KY zeolite, $S_{t,z}(\omega)$, are compared with the experimental spectrum, $S_z(\omega)$, in figure 6.5. The differences are slight, but it is clear that the change in dihedral angle has rather less

effect on the spectrum than the other small geometrical changes imposed by the zeolite environment. The remaining differences between observed and calculated spectra arise from our use of the harmonic approximation and changes to the vibrational potential energy due to intermolecular interactions. The spectral differences are small, and are comparable for both solid ferrocene and ferrocene in KY zeolite, from which we conclude that the interaction of ferrocene with the zeolite supercage is no stronger than that which occurs between neighbouring molecules in the pure ferrocene lattice.

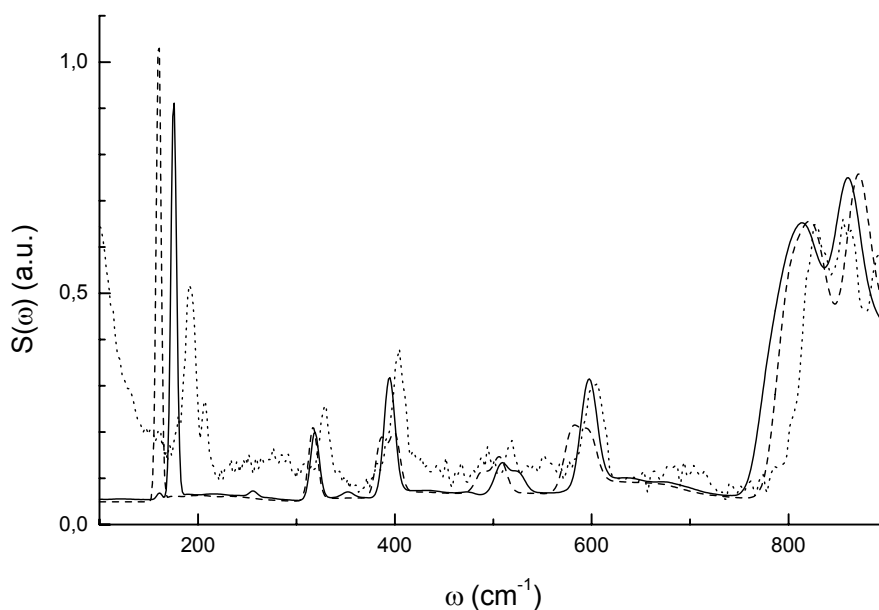


Figure 6.5 Inelastic neutron scattering spectrum $S_z(\omega)$ for ferrocene in KY zeolite at 20 K (dotted line) compared with $S_{t,e}(\omega)$ according to DFT calculations on a single eclipsed ferrocene molecule (dashed line) and $S_{t,z}(\omega)$ according to DFT calculations on a ferrocene molecule in the geometry as in the zeolite (solid line).

6.5 Conclusions

The catalytic activity of zeolites has at least three aspects: shape selectivity, weakening of bonds by host/guest interactions, and holding reactants in close proximity with each other. Our study of ferrocene in KY zeolite shows clearly that host/guest interactions are very weak in this case. It is also interesting to see how modern quantum-chemistry methods can be combined with INS spectroscopy and structural information to provide a fairly detailed analysis of systems as complex as ferrocene in KY zeolite. The zeolite distorts the soft coordinates of the ferrocene molecule, especially the inter-ring angle, and these are seen in the vibrational spectrum due to changes to the kinetic-energy terms. The potential-energy surface however, is virtually unchanged.

References

1. E. Kemner, A.R. Overweg, L. van Eijck, A.N. Fitch, E. Suard, I.M. de Schepper & G.J. Kearley. *Submitted*
2. E. Kemner, I.M. de Schepper, G.J. Kearley & U.A. Jayasooriya. *J. Chem. Phys.* **112** (2000) 10926
3. <http://www.isis.rl.ac.uk/molecularSpectroscopy/tosca/index.htm>
4. B. Delley, *J. Chem. Phys.* **92** (1990) 508
5. P. Perdew & Y. Wang, *Phys. Rev. B* **45** (1992) 13244
6. G.J. Kearley, *Nucl. Instr. Meth. A* **354** (1995) 53
7. J.S. Bodenheimer & W. Low, *Spectrochim. Acta* **29A** (1973) 1733
8. H. Jobic & A.N. Fitch, *Progress in Zeolite and Microporous materials. Studies in Surface Science and Catalysis* **105** (1997) 559

Chapter 7. Low frequency modes of ferrocene in zeolite Y

based on E. Kemner, C.F. de Vroege, M.T.F. Telling, I.M. de Schepper & G.J. Kearley,
Submitted to Appl. Phys. A

Abstract

Using the position of ferrocene in zeolite Y as found from diffraction we calculate the vibration modes of the ferrocene molecule as a whole, and the internal rotation of the ferrocene C₅H₅ rings with respect to each other of a ferrocene molecule in a Y-type zeolite using density functional theory. We compare our computational results with inelastic neutron scattering. We are able to identify two translational modes. The other modes lie at higher energies and are overlaid by motions arising from the flexibility of the zeolite framework.

7.1 Introduction

We study the inclusion of ferrocene Fe(C₅H₅)₂ molecules in the supercages of Y-type zeolites. This is of considerable importance to catalysis. The inclusion of organometallic complexes like ferrocene in a zeolite supercage could provide a means to deposit catalytically active transition metal clusters in the supercage.¹ Ferrocene Fe(C₅H₅)₂ consists of an iron atom ‘sandwiched’ by two identical parallel C₅H₅ rings. Recently we have determined from diffraction experiments the location of a ferrocene molecule in zeolite Y.² We find that the ferrocene molecules are located just above a line joining two neighbouring sodium ions at the SII positions in the zeolite supercage. The C₅H₅ rings are oriented towards the sodium ions in an ordered manner. This structure is confirmed by quantum chemistry calculations. Here we study the interaction between the ferrocene guest molecules and the zeolite host. On the intramolecular vibrational modes this interaction will be most noticeable in the torsion mode, where the two C₅H₅ rings oscillate in plane, but out of phase with each other. Naturally, the interaction between the ferrocene molecule and the zeolite supercage will also appear in external vibrations where the ferrocene molecule vibrates as a whole around its equilibrium position in the zeolite. In the present study we calculate the internal rotational mode of the ferrocene rings and the external translational and rotational modes of the whole ferrocene molecule for ferrocene in the supercages of zeolite Y with *ab-initio* density functional theory. Here we take the zeolite framework to be rigid. We compare our calculated frequencies with inelastic neutron scattering results. We are able to identify one observed peak. The other observed features in the neutron spectra can not be described by just vibrational motions of the ferrocene molecule with respect to a rigid zeolite framework, and we conclude that the flexibility of the zeolite framework is non-negligible.

7.2 RKS experiment

We measure the incoherent dynamic structure factor $S(Q,\omega)$ of ferrocene $\text{Fe}(\text{C}_5\text{H}_5)_2$ in the supercages of NaY zeolite, by means of inelastic neutron scattering at room temperature. For this we use the time-of-flight ‘Rotating Crystal Spectrometer’ or RKS of the IRI.³ Here an incoming neutron wavelength is selected by a rotating pyrolytic graphite crystal. Two Fermi-choppers rotating in phase with the crystal suppress undesired reflections. The scattered neutrons are then detected by ^3He tubes as a function of scattering angle and time. The raw data are subsequently corrected and converted to $S(Q,\omega)$ by standard data analysis methods.

We perform two experiments. First in Exp. I, the ‘high resolution’ experiment, we measure with an incoming neutron wavelength of 2.35 Å, yielding a measurable momentum Q transfer range of $0.3 \text{ \AA}^{-1} \leq Q \leq 3.4 \text{ \AA}^{-1}$ for the scattered neutrons, with an energy resolution $\Delta\omega$ of 0.31 meV. Next in Exp. II or the ‘low resolution’ experiment we measure with an incoming neutron wavelength of 1.56 Å to extend the Q -range. This yields a Q transfer range of $0.8 \text{ \AA}^{-1} \leq Q \leq 5.1 \text{ \AA}^{-1}$ with an energy resolution $\Delta\omega$ of 0.75 meV.

We first discuss the ‘high resolution’ experiment. A typical example of $S(Q,\omega)$ is shown in Fig. 7.1 for $Q = 1.6 \text{ \AA}^{-1}$.

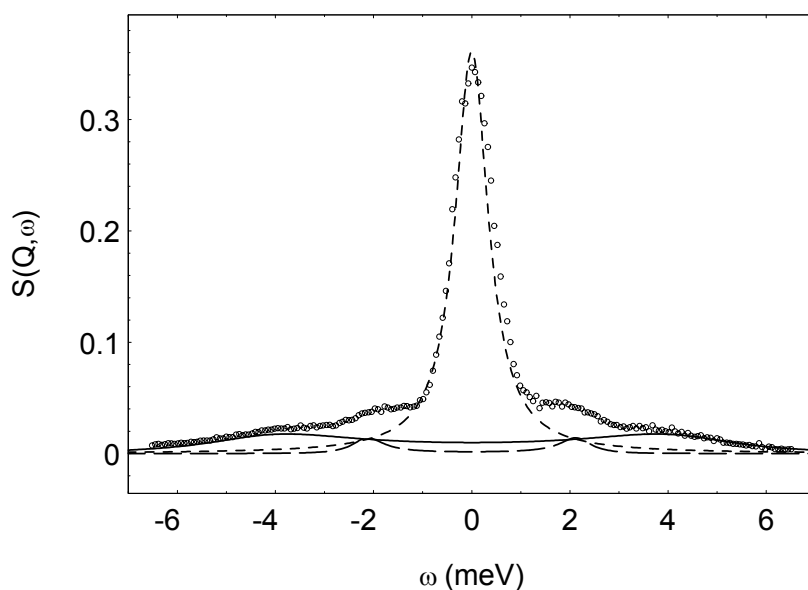


Figure 7.1 Incoherent dynamic structure factor $S(Q,\omega)$ for momentum transfer $Q = 1.6 \text{ \AA}^{-1}$ for Exp. I. of ferrocene in NaY zeolite at $T = 300 \text{ K}$ (open circles), together with a fit with 5 Lorentzians (as explained in the text). The solid line gives the side peaks at $\omega = \pm\omega_1$, the dashed line the side peaks at $\omega = \pm\omega_2$ and the dotted line the central peak at $\omega = 0$.

All $S(Q,\omega)$ can be described by five Lorentzians ($\omega_2 < \omega_1$),

$$S(Q, \omega) = A_0 \frac{1}{\pi} \frac{\lambda_0}{\omega^2 + \lambda_0^2} + A_1 \frac{1}{\pi} \left\{ \frac{\lambda_1}{(\omega - \omega_1)^2 + \lambda_1^2} + \frac{\lambda_1}{(\omega + \omega_1)^2 + \lambda_1^2} \right\} + A_2 \frac{1}{\pi} \left\{ \frac{\lambda_2}{(\omega - \omega_2)^2 + \lambda_2^2} + \frac{\lambda_2}{(\omega + \omega_2)^2 + \lambda_2^2} \right\} \quad (7.1)$$

Here, A_0 , λ_0 , A_1 , λ_1 , ω_1 , A_2 , λ_2 and ω_2 are used as fit parameters and depend on Q . The fits are satisfactory, see Fig. 7.1. We normalize total area $A = A_0 + 2A_1 + 2A_2$ to 1. The area of the central line $A_0(Q)/A$ is given in Fig. 7.2. It can be fitted by

$$A_0(Q) = A \exp\left(-\frac{1}{3} R^2 Q^2\right) \quad (7.2)$$

with $R = 0.65 \text{ \AA}$.

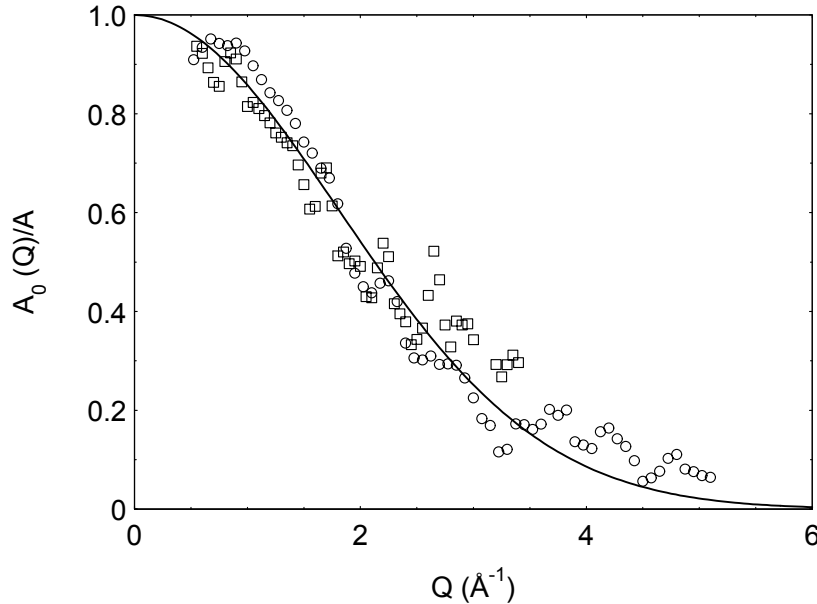


Figure 7.2 Area of the central line $A_0(Q)/A$ for Exp. I (squares) and Exp. II (circles). The solid line is a fit with an exponential, as explained in the text.

The areas of the sidelines A_1 and A_2 are shown in Fig. 7.3 and 7.4. $A_1(Q)$ increases with Q and becomes as large as $A_0(Q)$ at $Q \approx 3.0 \text{ \AA}^{-1}$. $A_2(Q)$ is very small (less than 2% of the total area) and can be described by

$$A_2(Q) = A a^2 Q^2 \exp\left(-\frac{1}{3} b^2 Q^2\right) \quad (7.3)$$

with $a = 0.13 \text{ \AA}$ and $b = 1.0 \text{ \AA}$, cf. the intensity of the fundamental mode of a harmonic oscillator as a function of Q at low temperature (see Eq. (1.54)).

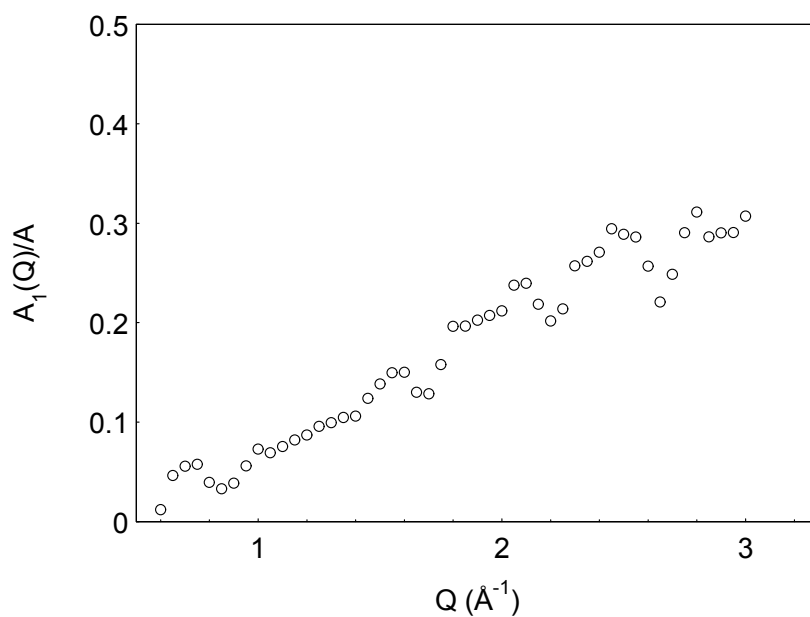


Figure 7.3 Area $A_1(Q)/A$ for Exp. I.

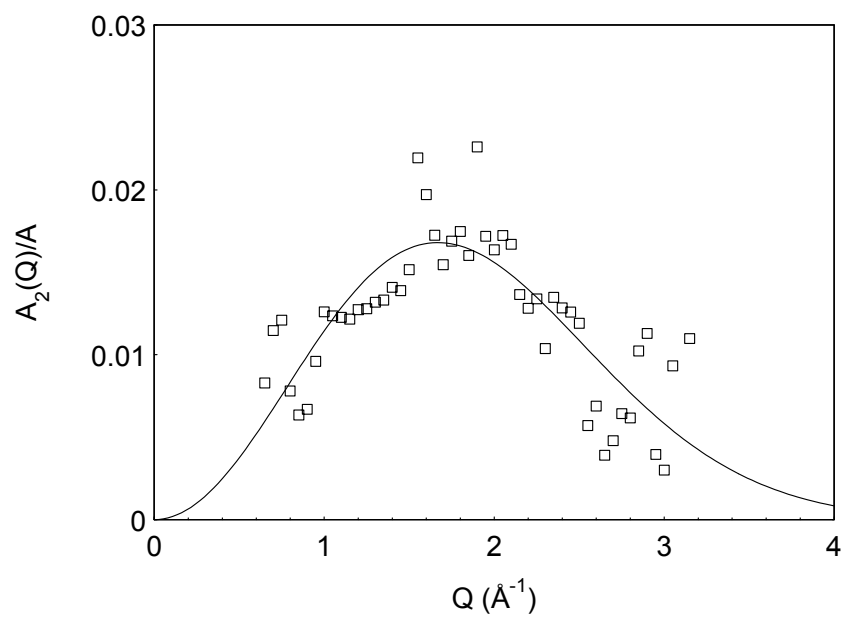


Figure 7.4 Area $A_2(Q)/A$ for Exp. I (squares). The solid line is a fit with $A_2(Q) = Aa^2Q^2 \exp(-\frac{1}{3}b^2Q^2)$, with fit parameters $a = 0.13 \text{ \AA}$ and $b = 1.0 \text{ \AA}$.

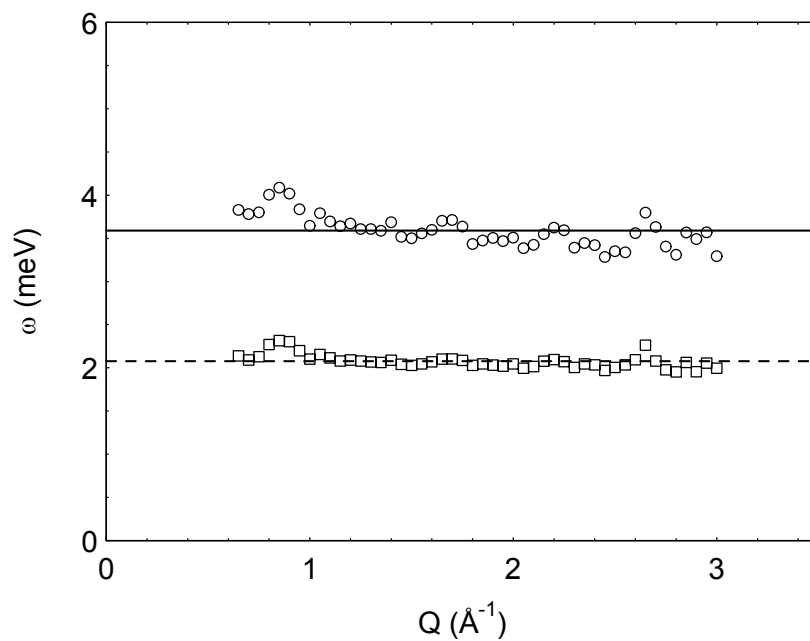


Figure 7.5 Frequencies of the sidelines $\omega_1(Q)$ (circles) and $\omega_2(Q)$ (squares) for Exp. I. The solid line equals $\omega = 3.6$ meV, the dotted line $\omega = 2.1$ meV.

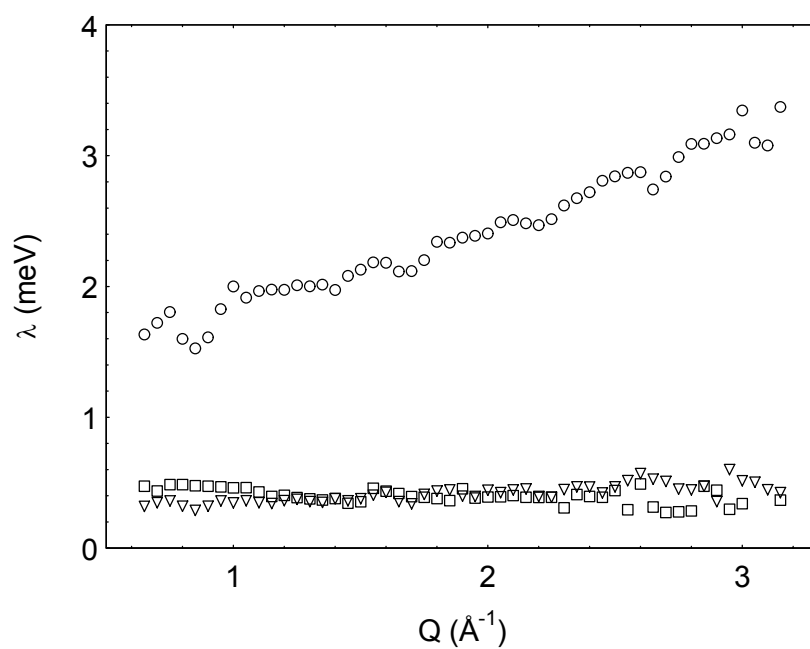


Figure 7.6 Halfwidths $\lambda_0(Q)$ (triangles), $\lambda_1(Q)$ (circles) and $\lambda_2(Q)$ (squares) for Exp. I.

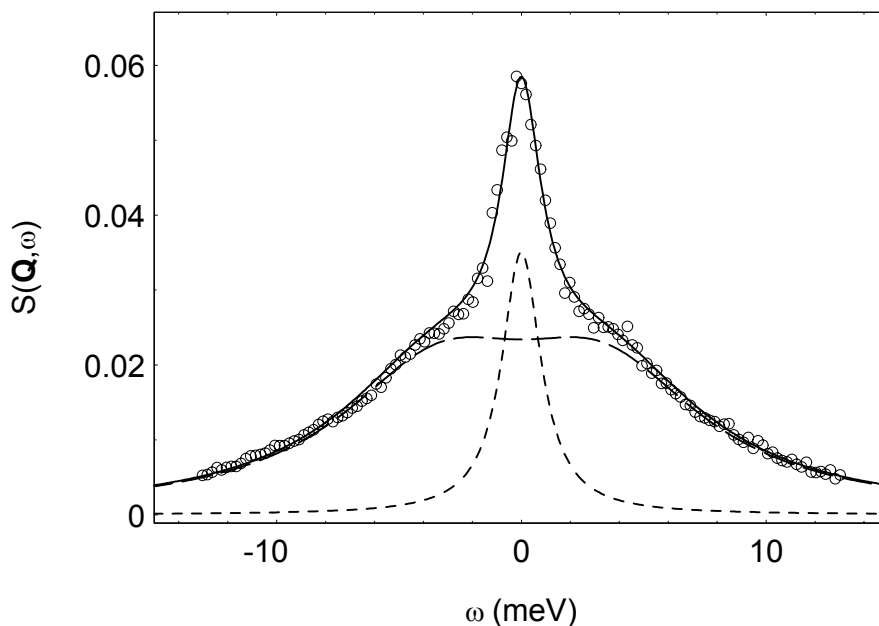


Figure 7.7 Incoherent dynamic structure factor $S(Q, \omega)$ for momentum transfer $Q = 4.0 \text{ \AA}^{-1}$ of ferrocene in NaY zeolite (open circles), together with a fit with 3 Lorentzians (as explained in the text). The dashed line gives the side peaks at $\omega = \pm\omega_1$, the dotted line the central peak $\omega = 0$. The solid gives the total fit.

The frequency of the sidelines $\omega_1(Q)$ and $\omega_2(Q)$ are displayed in Fig. 7.5. No Q -dependence is observed and $\omega_1 = 3.6 \text{ meV}$ ('outer peaks') and $\omega_2 = 2.1 \text{ meV}$ ('inner peaks'). The halfwidths $\lambda_0(Q)$, $\lambda_1(Q)$ and $\lambda_2(Q)$ are given in Fig. 7.6. Both $\lambda_0(Q)$ and $\lambda_2(Q)$ are independent of Q and equal to the experimental resolution: $\lambda_0(Q) = \lambda_2(Q) = \Delta\omega = 0.31 \text{ meV}$. This implies that the central line and the two weak inner peaks in $S(Q, \omega)$ are in fact δ -functions in ω (for the present resolution). The width $\lambda_1(Q)$ of the two outer peaks is much larger than $\Delta\omega$ and increases with Q (see Fig. 7.6).

Next we discuss the 'low resolution' experiment. A typical example of $S(Q, \omega)$ is shown in Fig. 7.7 for $Q = 4.0 \text{ \AA}^{-1}$. The most obvious observation is that there are only two 'outer' peaks located at $\pm\omega_1$. The two weak 'inner' peaks have disappeared, most likely due to the larger experimental resolution. For this experiment $S(Q, \omega)$ can be described by three symmetric Lorentzians given by Eq. (7.1) with $A_2 = 0$, i.e. one central line and two symmetric Lorentzians located at $\pm\omega_1$. The result for the area of the central line $A_0(Q)$ is shown in Fig. 7.3. For $A_0(Q)$ we do not find significant differences between the two experiments (see Fig. 7.2). Also for $\omega_1(Q)$ and $\lambda_1(Q)$ the differences are negligible. This leads us to the conclusion that both experiments are consistent with one another.

7.3 IRIS Experiment

We measure the incoherent dynamic structure factor $S(Q, \omega)$ of ferrocene $\text{Fe}(\text{C}_5\text{H}_5)_2$ in KY zeolite by means of inelastic neutron scattering at temperatures T 150 to 300 K on the IRIS spectrometer⁴ at ISIS, UK. IRIS is an inverted geometry time-of-flight spectrometer. We use the (004) reflection of the pyrolytic graphite analyser to obtain a final neutron energy of 7.28 meV. This yields an energy transfer range from about -3 to 4 meV with a resolution of 50 μeV and a momentum transfer range from 0.5 to 3.7 \AA^{-1} . The measured spectra are converted to $S(Q, \omega)$ using standard procedures. Part of the resulting spectra for $Q = 3.0 \pm 0.1 \text{\AA}^{-1}$ are shown in Fig. 7.8.

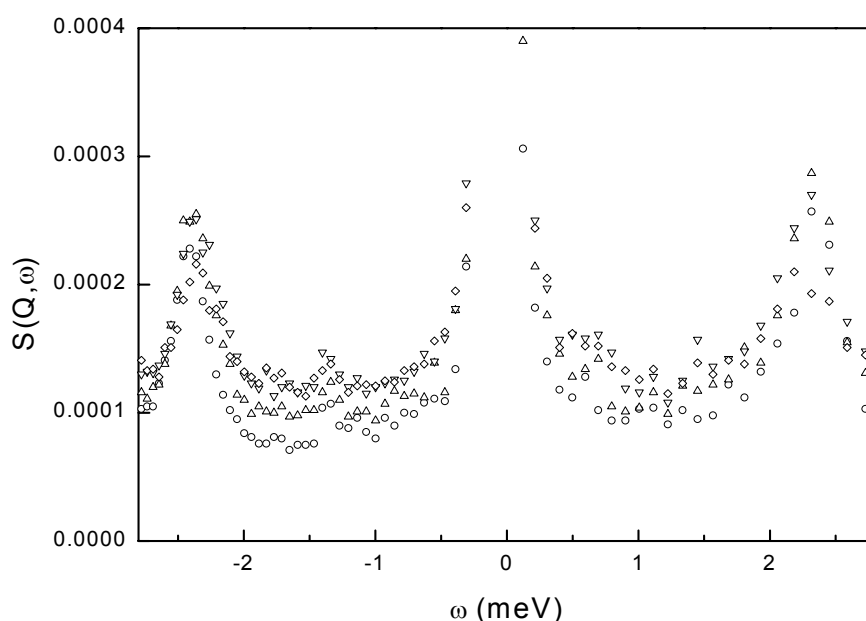


Figure 7.8 Incoherent dynamic structure factor $S(Q, \omega)$ of ferrocene in KY zeolite for momentum transfer $Q = 3.0 \pm 0.1 \text{\AA}^{-1}$ at temperatures $T = 150$ K (open squares), 200 K (circles), 250 K (triangles) and 300 K (inverted triangles).

At temperatures $T = 150$ K to $T = 300$ K we observe clear side peaks at $\omega = \pm\omega_3$, with an intensity of a few percent of the total intensity, as on the RKS, and a width of 0.2 meV. We find $\omega_3 = 2.3$ meV at $T = 250$ and 300 K and $\omega_3 = 2.4$ meV at $T = 150$ and 200 K. We were unable to determine the Q -dependence of the intensity of these peaks.

7.4 Computations

We calculate the frequencies ω_v of the vibrational modes v for translations of a ferrocene molecule in a zeolite fragment in the x , y and z direction (cf. Fig. 7.9), for

rotations of the ferrocene molecule as a whole around the x-, y- and z-axis and of the internal rotation of the cyclopentadienyl C_5H_5 rings with respect to each other. We do this by calculating the total energy of ferrocene and part of the zeolite supercell as in Fig. 7.9, cf. the optimised structure found before², for small translations Δ and rotations φ of the ferrocene molecule. From this we obtain the frequencies using the harmonic approximation. We calculate the various energies with density functional theory using the module Dmol³ of the program Cerius^{2,5}. We use the local density approximation, Perdew Wang functionals,⁶ the DND basis set,⁵ and an atomic cutoff radius of 5.5 Å.

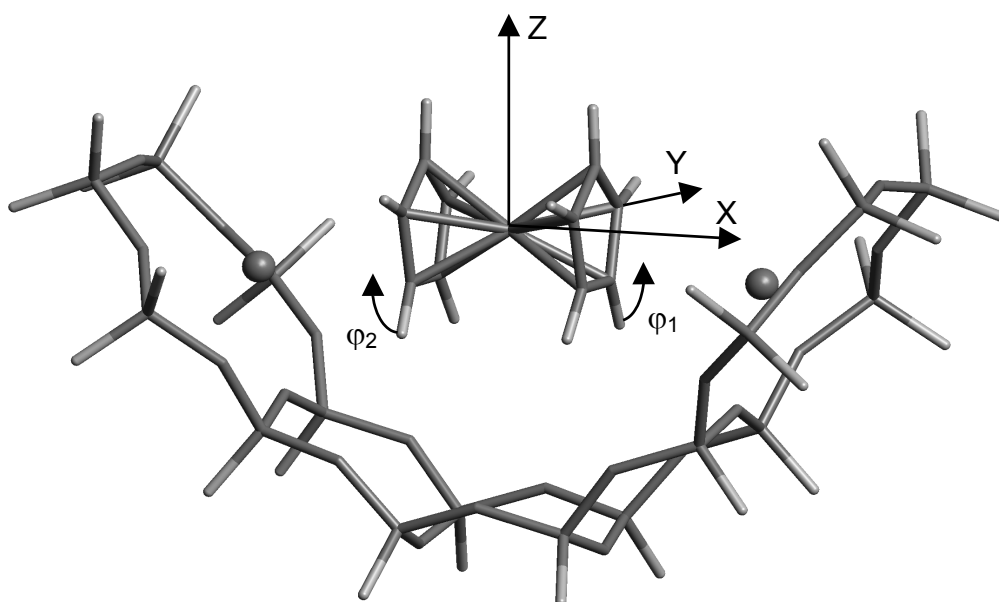


Figure 7.9 Illustration of the zeolite fragment and the ferrocene molecule as used for DFT calculations. Sodium ions are represented by spheres. The oxygen atoms adjacent to the zeolite framework have been replaced by hydrogen atoms.

We start with the external translational modes in the x and y direction (cf. Fig. 7.9). The results for the calculated energies E for displacements Δ from the equilibrium position along the x- and y-axis are shown in Fig. 7.10. Note that due to the symmetry of the position of ferrocene in the zeolite these energies will be the same for positive and negative displacements along the x- and y-axis. We approximate the energy around $\Delta = 0$ by $E = \frac{1}{2}K_v\Delta^2$, where K_v is a force constant (see Fig. 7.10). The results for K_v are shown in Table 7.1. The frequencies ω_v are obtained with $\omega_v = \sqrt{K_v/M}$ with $M = 3.1062 \cdot 10^{-25}$ kg the mass of a ferrocene molecule. The results for ω_v are shown in Table 7.1.

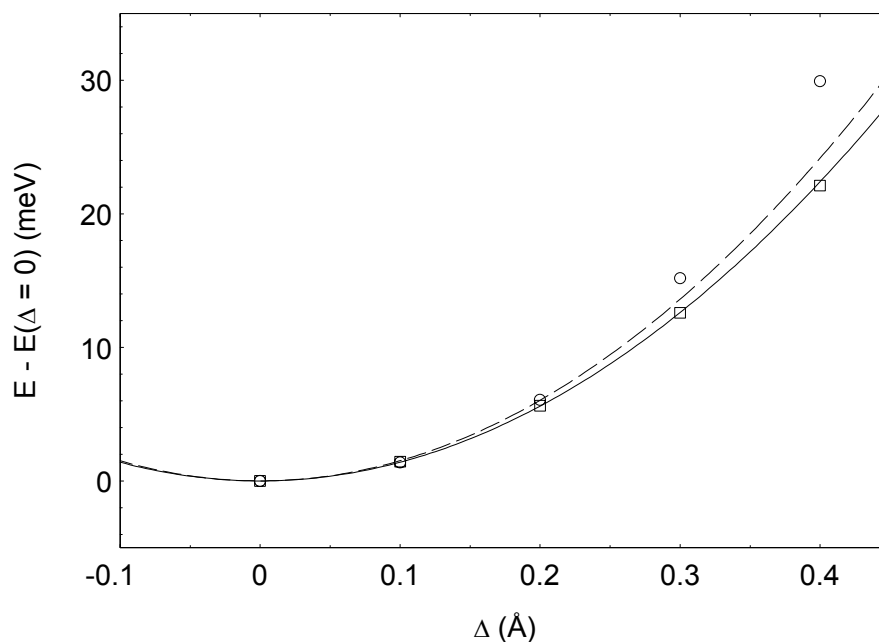


Figure 7.10 Potential $E(\Delta)$ of ferrocene $\text{Fe}(\text{C}_5\text{H}_5)_2$ in a zeolite Y supercage according to DFT calculations for displacements Δ from the equilibrium position along the x axis (circles) and the y axis (squares) (see Fig. 7.7). Also shown are fits with $E = \frac{1}{2}K\Delta^2$ for $\Delta = 0$ to $\Delta = 0.2$ Å along the x-axis (dashed line) and along the y-axis (solid line).

mode ν	K_ν	ω_ν (meV)	$R_\nu(\text{Å})$
translation x	$3.0 \cdot 10^2 \text{ meVÅ}^{-2}$	2.6	0.31
translation y	$2.8 \cdot 10^2 \text{ meVÅ}^{-2}$	2.5	0.31
translation z	$1.2 \cdot 10^3 \text{ meVÅ}^{-2}$	5.2	0.22
rotation y	$6.1 \cdot 10^3 \text{ meV}$	8.3	
rotation z	$5.2 \cdot 10^3 \text{ meV}$	7.6	
rotation x	$5.6 \cdot 10^2 \text{ meV}$	4.5	
internal rotation	$1.4 \cdot 10^3 \text{ meV}$	7.5	

Table 7.1 Force constants K_ν and frequencies ω_ν for the translational and rotational modes of the ferrocene molecule as a whole in a zeolite supercage and of the internal rotation of the cyclopentadienyl rings of ferrocene in a zeolite supercage. Also given are the radii R_ν for the translations at $T = 300$ K.

Next we calculate the energies for displacements along the z-axis. The results are shown in Fig. 7.11. Here $z = 0$ corresponds to the situation where the ferrocene molecule is just in between the two sodium ions. The minimum energy is found for $z = 0.61$ Å instead of $z = 0.88$ Å as found from diffraction. We calculate the force constant K_ν and frequency ω_ν in the harmonic approximation around $z = 0.61$ Å in the same manner as above. Again the results are shown in Table 7.1.

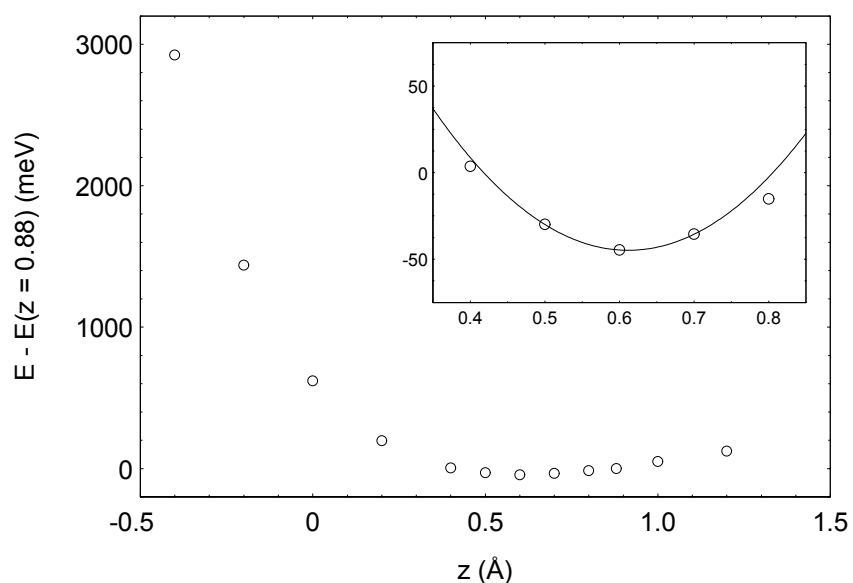


Figure 7.11 Potential $E(z)$ of ferrocene $\text{Fe}(\text{C}_5\text{H}_5)_2$ in a zeolite Y supercage according to DFT calculations for displacements from the position where the ferrocene is right in between the two sodium ions at the SII positions along the z axis (circles). The inset shows an enlargement around the minimum $z = 0.61$ Å together with a fit for $z = 0.5$ to $z = 0.7$ Å with a parabola conform the harmonic approximation.

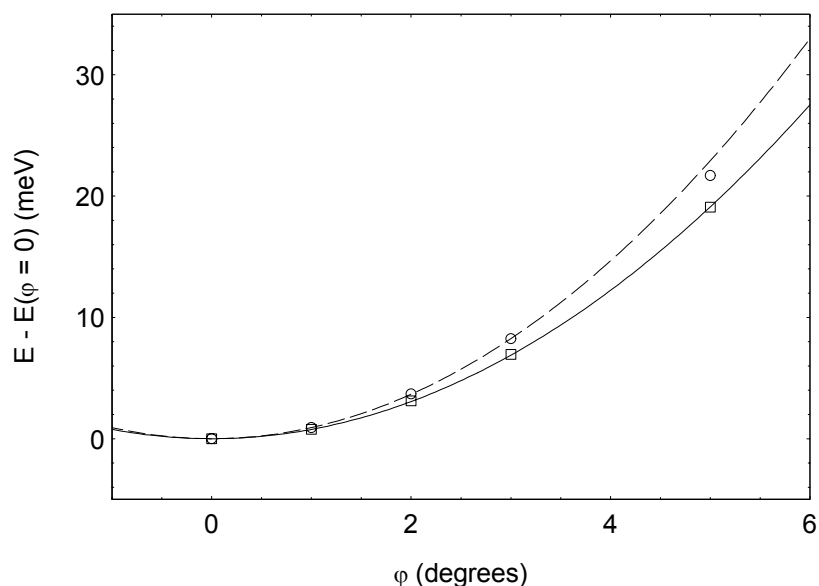


Figure 7.12 Potential $E(\phi)$ of ferrocene $\text{Fe}(\text{C}_5\text{H}_5)_2$ in a zeolite Y supercage according to DFT calculations for rotations ϕ from the equilibrium position around the y axis (circles) and the z axis (squares) (see Fig. 7.7). Also shown are fits with $E = \frac{1}{2}K\phi^2$ for $\phi = 0$ to $\phi = 3$ degrees around the y -axis (dashed line) and around the z -axis (solid line).

The energies for rotations φ from the equilibrium position around the y- and z-axis are shown in Fig. 7.12. Now we approximate the energy E around $\varphi = 0$ by $E = \frac{1}{2}K_\nu\varphi^2$. The frequency ω follows from $\omega_\nu = \sqrt{K_\nu/I_{yz}}$. Here $I_{yz} = 5.98 \cdot 10^{-45}$ kgm² is the moment of inertia for rotations around the y- and z-axis. The results for K_ν and ω_ν are shown in Table 7.1.

For rotations around the x-axis we write the energy E in the harmonic approximation as

$$E = \frac{1}{2}I_x\dot{\varphi}_1^2 + \frac{1}{2}I_x\dot{\varphi}_2^2 + \frac{1}{2}K_z\varphi_1^2 + \frac{1}{2}K_z\varphi_2^2 + \frac{1}{2}K_f(\varphi_1 + \varphi_2)^2 \quad (7.4)$$

Here φ_1 and φ_2 are the angles of rotation of the separate rings from their equilibrium position (see Fig. 7.8), $I_x = 1.88 \cdot 10^{-45}$ kgm² is the moment of inertia of one ring rotating around the x axis, K_z is the force constant for one ferrocene ring interacting with the zeolite and K_f the force constant for one ring interacting with the other ring. Eq. (7.4) can be rewritten as

$$E = \frac{1}{4}I_x(\dot{\varphi}_1 + \dot{\varphi}_2)^2 + \frac{1}{4}I_x(\dot{\varphi}_1 - \dot{\varphi}_2)^2 + \frac{1}{4}(K_z + 2K_f)(\varphi_1 + \varphi_2)^2 + \frac{1}{4}K_z(\varphi_1 - \varphi_2)^2 \quad (7.5)$$

This yields two frequencies,

$$\omega_i = \sqrt{\frac{K_z}{I_x}}, \quad \omega_o = \sqrt{\frac{K_z + 2K_f}{I_x}} \quad (7.6)$$

where ω_i corresponds to the in-phase rotation of the rings and ω_o to the out-of-phase, internal rotation of the rings. To obtain K_z we calculate the energy for rotations of the whole ferrocene molecule (i.e. two rings) around the x axis and dividing the result by two (see Fig. 7.13). We then obtain K_z as above. We have calculated the internal rotational barrier for the rings before (see Fig 7.13),⁷ from which we now obtain K_f . Because the energy is not smooth around $\varphi = 0$ we approximate the energy with $E = \frac{1}{2}E_f(1 - \cos(N\varphi))$ with $N = 5$ the number of minima from $\varphi = 0$ to $\varphi = 360$ degrees and $E_f = 39$ meV the energy barrier. We then obtain the force constant K_f with $K_f = \frac{1}{2}E_fN^2$. The results for K and ω are again shown in Table 7.1.

If we compare the calculated frequencies ω_ν of the external modes with the calculated potential energy we see that the frequencies are all in the region where the energy can be described by a parabola, validating the use of the harmonic approximation (see Figs. 7.10 to 7.13). In Table 7.1 we also give the radius R_ν at temperature $T = 300$ K for mode ν given by

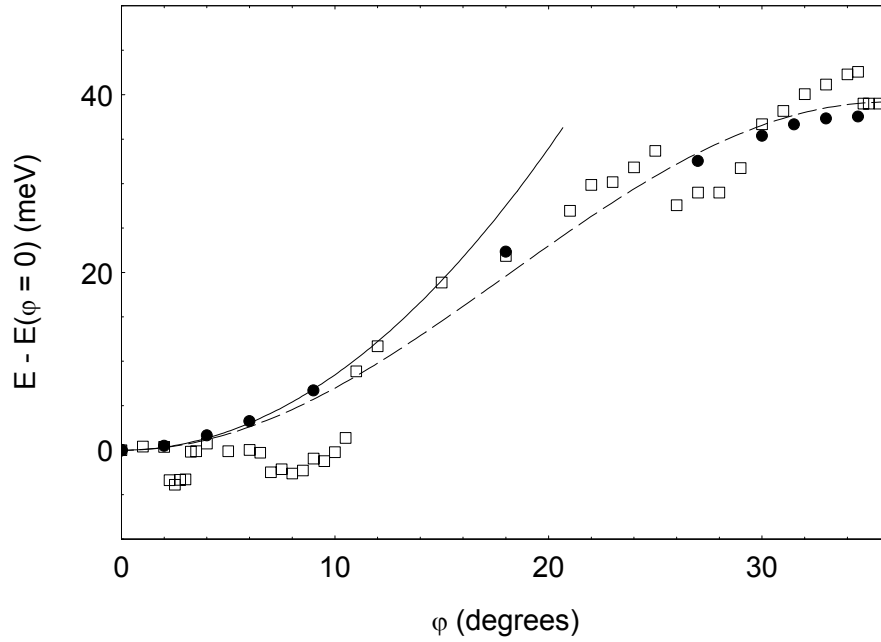


Figure 7.13 Potential $E(\varphi)$ for in-phase rotation of the two C_5H_5 rings in the ferrocene $Fe(C_5H_5)$ molecule in a zeolite Y supercage according to DFT calculations as a function of orientation φ where $\varphi = 0$ corresponds to the equilibrium orientation (solid squares) and a fit with $E = \frac{1}{2}K\varphi^2$ for $\varphi = 0$ to $\varphi = 9$ degrees (solid line). The open squares give the internal potential $E(\varphi)$ for rotation of the two C_5H_5 rings in a single ferrocene $Fe(C_5H_5)_2$ molecule with respect to each other according to Ref. 8. Also shown is a fit with $E(\varphi) = \frac{1}{2}E_f(1 - \cos(\pi(\varphi)/36))$, with energy barrier $E_f = 39$ meV (dashed line).

$$R_\nu = \left(\frac{\hbar}{2M\omega_\nu} \coth \left(\frac{\hbar\omega_\nu}{2k_B T} \right) \right)^{\frac{1}{2}} \quad (7.7)$$

where M is the mass of the ferrocene molecule and ω_ν the vibrational frequency (see also Eq. (1.52)). The quantity R_ν gives the average displacement from the equilibrium position of mode ν of the molecule and occurs in the Debye-Waller factor, $W(Q)$,

$$2W(Q) = \sum_\nu \frac{1}{3} R_\nu^2 C_\nu^2 Q^2 \quad (7.8)$$

where C_ν is the amplitude of the motion normalized with respect to all other motions, i.e. $\sum_\nu C_\nu^2 = 1$. Note that all motions of the molecule have effect on the Debye-Waller factor.

7.5 Discussion and conclusions

First we discuss the peak at $\omega_2 = 2.1$ meV at $T = 300$ K on the RKS and at $\omega_3 = 2.3$ meV at $T = 300$ and 250 K and $\omega_3 = 2.4$ meV at $T = 200$ and 150 K on IRIS. We see that this peak slightly shifts to higher frequency when the temperature decreases. From our calculations at $T = 0$ K we predict two peaks at $\omega_v = 2.5$ meV and $\omega_v = 2.6$ meV, corresponding to translational modes in the x and y direction cf. Fig. 7.9. With the experimental resolution these two modes are indiscernible in our neutron spectra. The intensity $A_2(Q)$ of this peak shows behaviour characteristic of a harmonic oscillator. We note that Eq. (7.3) is only valid when $\frac{k_B T}{\hbar\omega_2} \ll 1$. For ω_2 at $T = 300$ K this is not the case.

However, at higher temperatures we will still find $A_2(Q) = 0$ for $Q = 0$, then a maximum and an exponential drop for large Q , cf. the observed behaviour. The exact expression for $A_2(Q)$ for intermediate values of Q when T is not low depends on all modes the molecule is performing and is therefore extremely difficult to evaluate. we therefore attribute this peak to vibrations along the x- and y-axis. The fitted value for the Debye-Waller factor, with $b = 1.0$ Å, also depends on this intermediate Q behaviour. Consequently, it will not necessarily be the same (cf. the theoretical expectation) as the Debye-Waller factor determined from the central peak where $R = 0.7$ Å, as is indeed the case. The calculated values from Eq. (7.7) are of the same order of magnitude as the observed values. To determine the exact value of the Debye-Waller factor one will either have to measure all motions or perform a (non-trivial) absolute normalization.

At higher frequencies we observe, instead of the calculated discrete frequencies, a very broad and intense peak at $\omega_1 = 3.6$ meV for all Q in the RKS spectra. In the IRIS spectra this peak is indiscernible from the background. Both intensity $A_1(Q)$ and width $\lambda_1(Q)$ increase with increasing Q . Our calculations of the vibrational modes of a ferrocene molecule with respect to a rigid zeolite framework do not predict a peak with such behaviour. In reality the zeolite framework is, certainly at $T = 300$ K, flexible and the ferrocene molecules will move with it in some way. It is these movements that we observe in the neutron spectra. We assign the broad peak to effects arising from the flexibility of the zeolite framework. The large intensity of this peak compared with the small peak at $\omega_2 = 2.1$ meV shows that such effects are far more important to the neutron spectra than the vibrational modes of ferrocene with respect to the zeolite framework. The flexibility of the zeolite framework can not be neglected in calculations of external vibrational modes of molecules adsorbed in a zeolite, but unfortunately calculations of such effects from first principles are presently not feasible.

References

1. A. R. Overweg, H. Koller, J.W. de Haan, L.J.M. van de Ven, A.M. van der Kraan & R.A. van Santen, *J. Phys. Chem. B* **103** (1999) 4298
2. E. Kemner, A.R. Overweg, L. van Eijck, A.N. Fitch, E. Suard, I.M. de Schepper & G.J. Kearley, *Submitted*
3. <http://www.iri.tudelft.nl/~sfwww/meters/rks.html>
4. <http://www.isis.rl.ac.uk/CrystalAnalysers/iris.htm>

5. B. Delley, *J. Chem. Phys.* **92** (1990) 508
6. P. Perdew & Y. Wang, *Phys. Rev. B* **45** (1992) 13244
7. E. Kemner, I.M. de Schepper, G.J. Kearley & U.A. Jayasooriya, *J. Chem. Phys.* **112** (2000) 10926

General discussion and conclusions

We studied the inclusion of the organometallic ferrocene $\text{Fe}(\text{C}_5\text{H}_5)_2$ molecules in the supercages of Y-type zeolites. The scope of this thesis was to illuminate the interaction between ferrocene molecules and the supercages of zeolite Y. We did this by looking at the structure and the dynamics of ferrocene molecules in the zeolite supercage. We also looked into differences between a single ferrocene molecule, solid (crystalline) ferrocene and ferrocene in a zeolite supercage, thus illustrating the influence of a surrounding geometry on an encaged molecule. We focused on two types of zeolites, Na_{55}Y and K_{55}Y .

First we have shown in chapter 2 by powder X-ray and neutron diffraction that ferrocene molecules adsorbed in the supercages of NaY zeolite are located just above a line joining two neighbouring sodium ions at the SII positions in the zeolite supercage for loadings of one or two ferrocene molecules per supercage. The cyclopentadienyl C_5H_5 rings of the ferrocene molecules are oriented towards the sodium ions in an ordered manner. The inclusion of ferrocene in a Y-type zeolite thus provides a homogeneous distribution of iron throughout the zeolite at well-defined locations. We have shown this position to be an energy minimum using density functional theory. Also, the unit cell of the zeolite contracts upon adsorption of ferrocene, indicating an interaction between the ferrocene and the zeolite. The use of both X-ray and neutron diffraction proved to be very useful to locate the ferrocene molecules. On the one hand, with X-ray scattering heavy atoms such as the iron atom in ferrocene are easy to locate due to their high scattering. On the other hand, lighter atoms such as carbon and hydrogen in the cyclopentadienyl rings of ferrocene are clearly visible with neutron diffraction. The combination of both X-ray and neutron powder diffraction could also prove very useful for localising other transition metal complexes in zeolites with potential applications in e.g. catalysis.

Subsequently in chapter 3 we studied the bindings between a ferrocene guest molecule and the zeolite host by a topological analysis of the electron density obtained by density functional theory computations. We found that the ferrocene molecule interacts with the zeolite by hydrogen bonds between the rings and oxygen atoms in the zeolite framework. We also found some novel bond-paths between a ferrocene CC bond and a sodium and oxygen atom of the zeolite cage. These bonds are comparable with weak hydrogen bonds, but should not be thought of as the primary interaction between the ferrocene and the zeolite. They are secondary to the main Coulomb and hydrogen bond interactions that play the primary role in holding the ferrocene molecule in its place. The electrostatic interactions between the π -systems of the aromatic rings and the sodium ions pull the ferrocene molecule in between the ions. The hydrogen bonds between hydrogen atoms in the ferrocene rings and the zeolite framework are the cause of the unexpected orientation of the rings, which point with two hydrogen atoms towards the zeolite framework. This causes the rings of ferrocene in a zeolite to be eclipsed, while the rings in solid ferrocene are rotated by 9° from the eclipsed orientation. The rather long weak bonds from the centre of the ferrocene CC bond and

the zeolite are responsible for the displacement of the ferrocene molecule from the expected position right between the sodium ions. The electronic structure of the ferrocene molecule itself barely changes. It is the orientation in which the ferrocene molecule is held in the zeolite that renders it more reactive. An analysis of bindings by looking at the electron density provides a rather direct understanding of the host-guest interaction, even in complex systems.

We note that the ferrocene molecules might be slightly disordered, and that the position found by diffraction is a time average of several positions. This is a possible explanation for the novel bindings found, which could be forced by symmetry. Such disorder would be visible in the diffraction spectra via anisotropic temperature factors. We have not analysed this further since it involves very delicate effects, barely visible in our spectra that mainly originate from scattering from the zeolite framework. Moreover, the disorder would only be of the order of some hundreds of an Ångstrom, not affecting the global location of the ferrocene molecule or ring orientation. Finally density functional theory shows that the found position is indeed at least a local minimum.

Next we studied the molecular motion of ferrocene in the supercages of KY zeolite at temperatures $22 \text{ K} \leq T \leq 238 \text{ K}$ by means of quasielastic neutron scattering. The geometry of the motion is determined to be a 5-fold internal jump reorientation of the cyclopentadienyl C_5H_5 rings around the symmetry axis of the ferrocene molecule. We also obtain the mean residence time for these jumps at each temperature and determine the activation energy for the process to be 6.0 kJmol^{-1} . We note that from the measured EISF alone one cannot really discriminate between several jump models, or even other motions than reorientations of the rings. However, a 5-fold jump reorientation is consistent with earlier NMR measurements on ferrocene in zeolite. Such a motion has also been found for solid metallocenes. An additional proof of the 5-fold reorientational motion of the rings could come from a molecular dynamics simulation with force field methods. These methods are based on classical mechanics as opposed to *ab-initio* techniques, which start from quantum mechanics. A molecular dynamics simulation with *ab-initio* techniques is not feasible for a system as large as ferrocene in a zeolite supercage due to the large amount of computing time required. Force field methods are much faster, but less accurate. Here we try a simulation with the universal force field from *cerius²* and find that the position of ferrocene in zeolite can be well reproduced, including the orientation of the rings if one takes the hydrogen bonds between the ferrocene rings and the zeolite framework into account. We then calculate the dynamics and find that the resulting motion is indeed a 5-fold ring reorientational motion, but combined with a slight wobbling of the whole molecule and an occasional jump to a site between other ions. However, the calculated time scale is an order of magnitude different from that found in our measurements ($\sim 100 \text{ ps}$). Also, differences in energy for different orientations of the ferrocene molecule obtained with this force field are different from energy differences according to density functional theory. To solve this a more reliable force field for the interaction between ferrocene and a zeolite cage should be developed. Such a force field could also prove to be very useful to simulate the dynamics of other organometallics in zeolites.

In chapter 5 we measured the vibrational spectrum of solid ferrocene with inelastic neutron scattering. Since neutrons probe the vibrations of the nuclei directly, a theoretical calculation of intensities in the corresponding INS spectrum was feasible. We showed that a full comparison, i.e. including relative intensities, could be made between spectra for ferrocene obtained from inelastic neutron scattering (INS) and theoretical *ab-initio* calculations. Thus we could unambiguously assign a vibrational character to each line in the INS spectrum, as we did for the most prominent peaks. As a result we could remove some ambiguities existing in the literature. We also found consistency between the calculated potential energy of a single ferrocene molecule for different orientations, φ , of the two cyclopentadienyl C_5H_5 rings with respect to each other, which shows a potential barrier of 0.9 kcal/mol, and electron diffraction, and between the calculated shallow minimum at $\varphi = 9$ degrees and X-ray diffraction. We note that differences between the calculated and measured spectra, as for the torsion mode, might be due to the fact that we calculated the spectrum for a single ferrocene molecule. In solid ferrocene the molecules are not isolated, but interact with each other. Clearly, low frequency modes as the torsion mode will be the most affected. To calculate the vibrational spectrum for solid ferrocene including the interactions between different molecules from first principles is a formidable task but seems feasible in the near future. Finally, the combined use of inelastic neutron scattering and *ab-initio* calculations forms a powerful tool to analyse molecular vibrations.

Next we discussed the internal vibrations of a ferrocene molecule in a Y-type zeolite supercage. Compared with inelastic neutron scattering on solid ferrocene only small differences between the inelastic neutron scattering spectra are observed. These differences are compatible with those calculated by *ab-initio* calculations taking account only of the geometry of the ferrocene and ignoring the molecular environment. The catalytic activity of zeolites has at least three aspects: shape selectivity, weakening of bonds by host/guest interactions, and holding reactants in close proximity with each other. Our study of vibrations of ferrocene in zeolite Y clearly shows that the host/guest interactions are very weak, and comparable with the intermolecular interactions in solid ferrocene. The zeolite distorts the soft coordinates of the ferrocene molecule, especially the inter-ring angle, and these are seen in the vibrational spectrum due to changes to the kinetic energy terms. The potential energy surface however, is virtually unchanged. It is also interesting to see how modern quantum-chemistry methods can be combined with INS spectroscopy and structural information to provide a fairly detailed analysis of systems as complex as ferrocene in KY zeolite.

We also studied the interaction between the ferrocene guest molecules and the zeolite host in chapter 7. We looked more closely at the torsion mode, but also at the external vibrations where the ferrocene molecule vibrates as a whole around its equilibrium position in the zeolite. We calculated the internal rotational mode of the ferrocene rings and the external translational and rotational modes of the whole ferrocene molecule for ferrocene in the supercages of zeolite Y with *ab-initio* density functional theory, where we took the zeolite framework to be rigid. We compared our calculated frequencies with inelastic neutron scattering results, and were able to identify one observed peak. The other observed features in the neutron spectra could not be described by just vibrational motions of the ferrocene molecule with respect to a rigid zeolite framework, and we

concluded that the flexibility of the zeolite framework is non-negligible at lower frequencies.

Throughout this thesis we assumed that there is no difference between the position and dynamical behaviour of ferrocene in NaY and KY zeolite. The various results that are consistent with each other agree with this assumption. The relevant difference between Na⁺ and K⁺ ions is their size (the radius of a K⁺ ion is about 35% larger), and we believe that this has no significant influence. The main interactions between a ferrocene molecule and the zeolite framework are electrostatic interactions between the ferrocene rings and the zeolite cations and hydrogen bonds between the ferrocene rings and the zeolite framework. As a test we now calculate the energy barrier for rotations of ferrocene in KY zeolite with density functional theory as before for ferrocene in NaY zeolite. We find a difference in energy of only 0.6%.

Concluding, we illuminated the interaction between ferrocene molecules and a zeolite Y supercage. This system can be regarded as a model system for other, more complicated organometallic molecules in zeolites. The present study can also be used as a starting point to look at changes in the chemical reactivity of ferrocene, or other molecules, upon adsorption in a zeolite. This could provide the means to create ion clusters in the zeolite supercage, important for catalysis.

Summary

Zeolites are crystalline aluminosilicates with a three-dimensional open framework structure of channels and cavities of molecular dimensions. Zeolites can thus act as molecular sieves, making catalytic centres in the interior of the zeolite only accessible to molecules of the correct size. Such catalytic centres, especially clusters of transition metals, can be incorporated in zeolites by vapour phase insertion of volatile compounds, such as organometallics. An often used zeolite is zeolite Y, which contains especially large cavities, called supercages. We study the inclusion of the organometallic ferrocene, $\text{Fe}(\text{C}_5\text{H}_5)_2$, molecules in the supercages of Y-type zeolites. Ferrocene consists of an iron atom 'sandwiched' by two identical parallel cyclopentadienyl, C_5H_5 , rings. The scope of this thesis is to determine the structure and dynamics of ferrocene in zeolite Y, and to illuminate the interaction between the ferrocene molecules and the zeolite supercages. We look into differences between a single ferrocene molecule, solid (crystalline) ferrocene and ferrocene in a zeolite supercage, thus illustrating the influence of a surrounding geometry on an engaged molecule. We focus on two types of zeolites, Na_{55}Y and K_{55}Y .

First we find the exact location of the ferrocene molecules within the supercages by performing powder neutron and X-ray diffraction on bare NaY zeolite, and on NaY zeolite loaded with one and two ferrocene molecules per supercage. Using the complementary properties of both techniques we show that the ferrocene molecules are located just above the line joining two neighbouring sodium ions at the SII positions in the zeolite supercage. The C_5H_5 rings are oriented towards the sodium ions in an ordered manner. This structure is confirmed by quantum chemistry calculations. The inclusion of ferrocene in a Y-type zeolite provides a homogeneous distribution of iron throughout the zeolite at well-defined locations.

Subsequently we study the bindings between a ferrocene guest molecule and the zeolite host by a topological analysis of the electron density as calculated by density functional theory. It transpires that the guest and host are not only connected by hydrogen bonds, but also by some novel bond-paths between regions of high electron density on the guest and atoms of the zeolite cage. These bonds are comparable with weak hydrogen bonds. The electronic structure of the ferrocene molecule itself barely changes. It is the orientation in which the ferrocene molecule is held in the zeolite that renders it more reactive.

Next we study the molecular motion of ferrocene in the supercages of KY zeolite at temperatures $22 \text{ K} \leq T \leq 238 \text{ K}$ by means of quasielastic neutron scattering. The geometry of the motion is determined to be a 5-fold internal jump reorientation of the cyclopentadienyl C_5H_5 rings around the symmetry axis of the ferrocene molecule. We also obtain the mean residence time between these jumps at each temperature and determine the activation energy for the process to be 6.0 kJmol^{-1} . The results are consistent with results obtained earlier by NMR measurements.

We then measure the vibrational spectrum of solid ferrocene with inelastic neutron scattering. We compare this with an *ab-initio* calculation of the internal vibrations of a

single ferrocene molecule using density functional theory (without free parameters). Due to the good agreement between the experimental and calculated spectra we can assign each vibrational mode to each observed peak in the neutron spectrum. We also find consistency between the calculated potential energy of a single ferrocene molecule for different orientations, φ , of the two cyclopentadienyl rings with respect to each other, which shows a potential barrier of $0.9 \text{ kcal mol}^{-1}$, and electron diffraction, and between the calculated shallow minimum at $\varphi = 9$ degrees and X-ray diffraction.

Next we compare the measured inelastic neutron scattering (INS) vibrational spectrum of ferrocene in the supercages of KY zeolite with that of solid ferrocene. Only small differences between these spectra are observed. We show that these differences are compatible with those calculated by *ab-initio* calculations taking account only of the geometry of the ferrocene and ignoring the molecular environment. We conclude that the ferrocene-zeolite interactions are rather weak, and comparable with the intermolecular interactions in solid ferrocene.

Using the position of ferrocene in zeolite Y as found from diffraction we also calculate the vibration modes of the ferrocene molecule as a whole, and the internal rotation of the ferrocene C_5H_5 rings with respect to each other, of a ferrocene molecule in a Y-type zeolite using density functional theory. We compare these computational results with inelastic neutron scattering. We are able to identify two translational modes. The other modes lie at higher energies and are overlaid by motions arising from the flexibility of the zeolite framework.

Samenvatting

Zeolieten zijn kristallijne aluminosilicaten met een drie dimensionale open structuur van kanalen en holtes van moleculaire afmetingen. Hierdoor kunnen zeolieten gebruikt worden als moleculaire zeven en zijn eventuele katalytische centra in het zeoliet alleen toegankelijk voor moleculen van de juiste afmetingen. Zulke katalytische centra, vooral clusters van overgangsmetalen, kunnen in het zeoliet ingebouwd worden door het in de gasfase inbrengen van vluchtige verbindingen. Een voorbeeld hiervan zijn organometalen als ferroceen. Ferroceen, $\text{Fe}(\text{C}_5\text{H}_5)_2$, bestaat uit een ijzer atoom omgeven door twee identieke parallelle cyclopentadienyl, C_5H_5 , ringen. Een type zeoliet dat vaak wordt gebruikt is het zeoliet Y. Zeoliet Y bevat zeer grote kooien die superkooien worden genoemd. In dit proefschrift wordt de absorptie van ferroceen moleculen in de superkooien van zeoliet Y bestudeerd. Het doel van het hier beschreven onderzoek is de structuur en de dynamica van ferroceen in zeoliet Y te bepalen, en de interactie tussen de ferroceen moleculen en de superkooien van het zeoliet Y duidelijk te maken. We bekijken verschillen tussen een enkel ferroceen molecuul, vast (kristallijn) ferroceen en ferroceen in een superkooi van het zeoliet en illustreren daarmee de invloed van een omringende geometrie op een opgesloten molecuul. We richten ons op twee soorten zeolieten, Na_{55}Y en K_{55}Y .

Eerst wordt de exacte locatie van de ferroceen moleculen in de superkooien bepaald door middel van neutronen en röntgen diffractie op leeg NaY zeoliet, en op NaY zeoliet beladen met één en twee ferroceen moleculen per superkooi. Door gebruik te maken van de complementaire eigenschappen van beide technieken tonen we aan dat de ferroceen moleculen zich net boven de lijn bevinden die twee natrium ionen op de 'SII' posities in de superkooi met elkaar verbindt. De C_5H_5 ringen richten zich op een geordende manier naar de natrium ionen. Deze structuur wordt bevestigd door quantummechanische berekeningen. De absorptie van ferroceen in een Y-type zeoliet zorgt voor een homogene verdeling van ijzer in het zeoliet op goed gedefinieerde locaties.

Vervolgens bestuderen we de bindingen tussen een ferroceen molecuul en het zeoliet door een topologische analyse van de elektronendichtheid zoals berekend met density functional theory. Het blijkt dat het ferroceen en het zeoliet niet alleen met elkaar verbonden zijn door waterstofbruggen, maar ook door een nieuw soort bindingen tussen gebieden met een hoge elektronendichtheid in het ferroceen en atomen van het zeoliet. Deze bindingen zijn vergelijkbaar met zwakke waterstofbruggen. De elektronische structuur van het ferroceen molecuul zelf verandert nauwelijks. Het is de oriëntatie waarin het ferroceen door het zeoliet gehouden wordt die het molecuul chemisch actiever maakt.

Daarna onderzoeken we de moleculaire beweging van ferroceen in de superkooien van KY zeoliet op temperaturen $22 \text{ K} \leq T \leq 238 \text{ K}$ met behulp van quasielastische neutronenverstrooiing. We zien een sprongsgewijze 5-voudige interne heroriëntatie van de C_5H_5 ringen rond de lengte as van het ferroceen molecuul. We vinden ook de gemiddelde verblijfstijd tussen deze sprongen op elke temperatuur en we bepalen dat de

activeringsenergie voor dit proces $6,0 \text{ kJmol}^{-1}$ is. Deze resultaten zijn consistent met eerdere resultaten van NMR metingen.

Vervolgens meten we het vibratiespectrum van vast ferroceen met inelastische neutronenverstrooiing. Dit wordt vergeleken met een ab initio berekening van de interne vibraties van een enkel ferroceen molecuul waarbij gebruik gemaakt wordt van density functional theory, zonder vrije parameters. Door de goede overeenkomst tussen het experimentele en het berekende spectrum kan elke vibratie toestand aan elke geobserveerde piek in het neutronen spectrum toegekend worden. We vinden ook consistentie tussen de berekende potentiële energie van een enkel ferroceen molecuul voor verschillende oriëntaties, φ , van de twee C_5H_5 ringen ten opzichte van elkaar, met een potentiaal barrière van 0.9 kcalmol^{-1} , en elektronen diffractie, en consistentie tussen het berekende ondiepe minimum voor $\varphi = 9$ graden en röntgen diffractie.

Daarna vergelijken we het met inelastische neutronenverstrooiing gemeten vibratiespectrum van ferroceen in de superkooien van KY zeoliet met dat van vast ferroceen. We zien slechts kleine verschillen tussen deze spectra. Deze verschillen komen overeen met die zoals berekend met density functional theory, waarbij we alleen de structuur van het ferroceen in rekening brengen en de moleculaire omgeving verwaarlozen. De interacties tussen het ferroceen en het zeoliet zijn zwak en vergelijkbaar met de intermoleculaire interacties in vast ferroceen.

We berekenen ook de trillingswijzen van het ferroceen molecuul als geheel, en van de interne rotatie van de ferroceen C_5H_5 ringen ten opzichte van elkaar, van een ferroceen molecuul in een Y-type zeoliet met behulp van density functional theory. De computer resultaten worden vergeleken met resultaten van inelastische neutronenverstrooiing. Twee translatiewijzen kunnen geïdentificeerd worden. De andere vibratietoestanden hebben een hogere energie en vallen samen met bewegingen veroorzaakt door de flexibiliteit van het zeoliet.

Appendix A. Model independent determination of the elastic incoherent structure factor in neutron scattering experiments

E. Kemner, I.M. de Schepper, A.J.M. Schmets & H. Grimm, *Nucl. Instr. Meth. B* **160** (2000) 544

Abstract

In quasielastic neutron scattering the dynamic structure factor $S(Q, \omega)$ consists of an elastic central line with area given by the Elastic Incoherent Structure Factor (EISF) and a continuous quasielastic broadening. Using only the resolution function of the spectrometer we discuss a method to derive the EISF directly from the raw experimental data points $S(Q, \omega)$ without any smoothing or any modelling of the quasielastic broadening. We compare this model to the Fourier transform method, show how it works on actual neutron scattering data and discuss its accuracy for several cases.

A.1 Introduction

Quasielastic neutron scattering (QENS) has proven to be a successful technique to determine translational and rotational motions of hydrogen containing molecules locked up in crystals or confined geometries in general.¹

The normalized theoretical incoherent dynamic structure factor $S_{th}(Q, \omega)$, i.e. the scattered neutron intensity as a function of momentum Q and energy ω transfer, can, for a powder sample, in general be written as

$$S_{th}(Q, \omega) = E(Q)\delta(\omega) + B_{th}(Q, \omega) \quad (\text{A.1})$$

where the amplitude $0 \leq E(Q) \leq 1$ of the delta function in ω is the so called elastic incoherent structure factor EISF and $B_{th}(Q, \omega)$ is the continuous quasielastic broadening, which depends on the precise dynamics of the molecule. The EISF is directly related to the static geometry of the process and given by

$$E(Q) = \left\langle \left| \sum_{i=1}^n P_i \exp(i\mathbf{Q} \cdot \mathbf{R}_i) \right|^2 \right\rangle_{ang} \quad (\text{A.2})$$

Here, n is the number of sites accessible to the molecule (which may be infinite), \mathbf{R}_i the location of site i and P_i the normalized probability to be at site i . In Eq. (A.2) we have taken the angular powder average over all directions of the unit vector $\hat{\mathbf{Q}} = \mathbf{Q}/Q$, with Q the length of the vector \mathbf{Q} .

The behaviour of the EISF as a function of Q is of great practical interest since it determines to a large extent (but not uniquely) the basic static properties n , \mathbf{R}_i and P_i of the process. For example, from the small Q behaviour $E(Q) = 1 - R_G^2 Q^2 / 3 + \dots$ one determines the Guinier radius R_G that is the effective radius of the region in which the molecule is locked up. Also, when knowing that the sites are equally accessible ($P_i = 1/n$), $E(Q) = 1/n$ for $Q \rightarrow \infty$ as follows from Eq. (A.2). Thus the behaviour of $E(Q)$ for large Q directly determines the number of sites accessible to the molecule (which is infinite, when $E(Q) \rightarrow 0$ for $Q \rightarrow \infty$). A thorough discussion of the intermediate behaviour of $E(Q)$ is given in Bée.¹

In the theoretical spectrum $S_{th}(Q, \omega)$ of Eq. (A.1) the relevant elastic peak $E(Q)\delta(\omega)$ is clearly separated from the continuous quasielastic broadening $B_{th}(Q, \omega)$. Experimentally, this distinction is often not straightforward due to finite resolution. In this paper we discuss a simple and convenient method to determine $E(Q)$ from the corresponding experimental spectra in a model independent way i.e. not assuming a particular shape of $B_{th}(Q, \omega)$.

The experimentally measured incoherent dynamic structure factor $S(Q, \omega)$ is given by $S_{th}(Q, \omega)$ folded with the resolution function $R(Q, \omega)$ of the spectrometer, i.e.

$$S(Q, \omega) = \int_{-\infty}^{+\infty} d\omega' S_{th}(Q, \omega') R(Q, \omega - \omega') \quad (\text{A.3})$$

so that

$$S(Q, \omega) = E(Q)R(Q, \omega) + B(Q, \omega) \quad (\text{A.4})$$

with the experimental quasielastic broadening or ‘background’ given by

$$B(Q, \omega) = \int_{-\infty}^{+\infty} d\omega' B_{th}(Q, \omega') R(Q, \omega - \omega') \quad (\text{A.5})$$

In this paper we use for all Q the conventional normalisations in ω for the even functions $S(Q, \omega)$ and $R(Q, \omega)$, i.e.

$$\int_{-\infty}^{+\infty} d\omega S_{th}(Q, \omega) = \int_{-\infty}^{+\infty} d\omega S(Q, \omega) = \int_{-\infty}^{+\infty} d\omega R(Q, \omega) = 1 \quad (\text{A.6})$$

We also assume that the resolution function $R(Q, \omega)$ of the spectrometer is so accurately known that $R(Q, \omega)$, its Fourier transform in ω and $\partial^2 R(Q, \omega) / \partial \omega^2$ can all be represented by numerical interpolation formulas, without significant error.

To determine the EISF, $E(Q)$, from the experimental spectrum $S(Q,\omega)$ of Eq. (A.4) two methods have been discussed before in the literature.^{1,2} In the first method, by “Fourier transforms”, one determines the experimental intermediate scattering function

$$F(Q,t) = \int_{-\infty}^{+\infty} d\omega \exp(i\omega t) S(Q,\omega) \quad (\text{A.7})$$

and the Fourier transform $F_R(Q,t)$ of the resolution function

$$F_R(Q,t) = \int_{-\infty}^{+\infty} d\omega \exp(i\omega t) R(Q,\omega) \quad (\text{A.8})$$

Then, it follows from Eqs. (A.1), (A.3) and (A.4), that

$$E(Q) = \lim_{t \rightarrow \infty} F(Q,t) / F_R(Q,t) \quad (\text{A.9})$$

In practice however, this method is often not feasible,^{1,3} due to the noise in $F(Q,t)$ and the fact that $F_R(Q,t)$ tends to zero for $t \rightarrow \infty$. We discuss this further at the end.

In the second method, by “model fitting”, one determines the EISF from a fit on the total spectrum, thereby assuming a model for $B_{th}(Q,\omega)$. For example, the $B_{th}(Q,\omega)$ for jump diffusion over n sites is described by a sum of $n - 1$ Lorentzians with area $B_i(Q)$, i.e.

$$B_{th}(Q,\omega) = \sum_{i=1}^{n-1} B_i(Q) L(\lambda_i; \omega) \quad (\text{A.10})$$

where

$$L(\lambda; \omega) = \frac{1}{\pi} \frac{\lambda}{\omega^2 + \lambda^2} \quad (\text{A.11})$$

is a normalized Lorentzian with halfwidth at halfmaximum (HWHM) equal to λ . However, this method is rather cumbersome since a model to describe $B_{th}(Q,\omega)$ is not known a priori. In fact such a model is derived from the behaviour of the EISF as a function of Q . Thus it is highly convenient to have a procedure to determine the EISF first in a model independent way, also avoiding Fourier transforms. Here we present such a method, discuss its accuracy and illustrate the method using a particular neutron spectrum $S(Q,\omega)$.

A.2 Theory

We discuss the simple and convenient relation for $E(Q)$ given by

$$E(Q) = \int_{-\infty}^{+\infty} d\omega S(Q, \omega) \Re(Q, \omega) - \Delta(Q) \quad (\text{A.12})$$

with $\Re(Q, \omega)$ determined solely by the resolution function as

$$\Re(Q, \omega) = \frac{\partial^2}{\partial \omega^2} R(Q, \omega) \bigg/ \int_{-\infty}^{+\infty} d\omega R(Q, \omega) \frac{\partial^2}{\partial \omega^2} R(Q, \omega) \quad (\text{A.13})$$

and where usually the correction factor $\Delta(Q)$ can be neglected as will be shown at the end. Thus, by setting in Eq. (A.12) $\Delta(Q) = 0$ and using the independently numerically known $\Re(Q, \omega)$, the EISF $E(Q)$ is directly obtained from a single integration (i.e. summation) over the raw experimental data points $S(Q, \omega)$. We note that $S(Q, \omega)$ is needed only in the small region around $\omega = 0$ where $R(Q, \omega) \neq 0$ and that no limiting, modelling or smoothing procedures are involved.

To derive Eq. (A.12) we define for $0 \leq \alpha \leq 1$

$$\tilde{S}(\alpha; Q, \omega) \equiv S(Q, \omega) - \alpha R(Q, \omega) \quad (\text{A.14})$$

and

$$I(\alpha; Q) \equiv \int_{-\infty}^{+\infty} d\omega \left\{ \frac{\partial}{\partial \omega} \tilde{S}(\alpha; Q, \omega) \right\}^2 \quad (\text{A.15})$$

The idea is that by partially subtracting the sharp resolution function $R(Q, \omega)$ from $S(Q, \omega)$ in Eq. (A.14) with varying α , the result $\tilde{S}(\alpha; Q, \omega)$ must become as ‘smooth’ as possible to optimally represent the continuous quasielastic broadening $B(Q, \omega)$ in Eq. (A.4) for $S(Q, \omega)$. Hence $I(\alpha; Q)$ which is the integral over the square of the derivative of $\tilde{S}(\alpha; Q, \omega)$ with respect to ω must be as small as possible. Therefore the ‘smoothest’ $\tilde{S}(\alpha; Q, \omega)$ ($\approx B(Q, \omega)$) is obtained when $\alpha = \alpha^*$ for which

$$\left. \frac{\partial I(\alpha; Q)}{\partial \alpha} \right|_{\alpha=\alpha^*} = 0 \quad (\text{A.16})$$

for each value of Q . Substitution of Eqs. (A.14) and (A.15) for $I(\alpha; Q)$ yields

$$\alpha^*(Q) = \int_{-\infty}^{+\infty} d\omega S(Q, \omega) \Re(Q, \omega) \quad (\text{A.17})$$

Substitution of $S(Q, \omega) = E(Q)R(Q, \omega) + B(Q, \omega)$ (cf. Eq. (A.4)) and using that $\int_{-\infty}^{+\infty} d\omega R(Q, \omega) \Re(Q, \omega) = 1$ (cf. Eq. (A.13)) leads to

$$E(Q) = \alpha^*(Q) - \Delta(Q) \quad (\text{A.18})$$

which is Eq. (A.12) with the error given by

$$\Delta(Q) = \int_{-\infty}^{+\infty} d\omega \int_{-\infty}^{+\infty} d\omega' B_{th}(Q, \omega') R(Q, \omega - \omega') \Re(Q, \omega) \quad (\text{A.19})$$

From the fact that $\int d\omega \Re(Q, \omega) = 0$ follows that $\Delta(Q) = 0$ when $B_{th}(Q, \omega)$ is constant over the (small) range of the resolution function where $R(Q, \omega) \neq 0$.

To estimate $\Delta(Q)$ explicitly we assume two extremal functional shapes of the normalized resolution function $R(Q, \omega)$ with given HWHM $\lambda_R(Q)$, i.e. Lorentzian $R(Q, \omega) = L(\lambda_R(Q), \omega)$ (cf. Eq. (A.11)) and Gaussian $R(Q, \omega) = G(\lambda_R(Q), \omega)$ where

$$G(\lambda; \omega) = \frac{1}{\lambda} \sqrt{\frac{\ln 2}{\pi}} \exp\left(-\ln 2 \frac{\omega^2}{\lambda^2}\right) \quad (\text{A.20})$$

We calculate $\Delta(Q)$ in Eq. (A.12) for the following four cases.

- I. First we assume that the resolution is Lorentzian with HWHM $\lambda_R(Q)$ and that the theoretical background is Lorentzian with area $B(Q)$ and HWHM $\lambda_B(Q)$, i.e. $B_{th}(Q, \omega) = B(Q)L(\lambda_B(Q), \omega)$. Then, cf. Eq. (A.19), one finds straightforwardly

$$\Delta(Q) = \Delta_{L,L}(Q) = B(Q) \left[1 + \frac{\lambda_B(Q)}{2\lambda_R(Q)} \right]^{-3} \quad (\text{A.21})$$

- II. Next, we assume that the resolution is Gaussian with HWHM $\lambda_R(Q)$ and that the theoretical background is Gaussian with area $B(Q)$ and HWHM $\lambda_B(Q)$, i.e. $B_{th}(Q, \omega) = B(Q)G(\lambda_B(Q), \omega)$. Then, cf. Eq. (A.19),

$$\Delta(Q) = \Delta_{G,G}(Q) = B(Q) \left(1 + \frac{\lambda_B(Q)}{\lambda_R(Q)} + \frac{\lambda_B(Q)^2}{2\lambda_R(Q)^2} \right)^{-\frac{3}{2}} \quad (\text{A.22})$$

III. We assume that the resolution is Gaussian (HWHM $\lambda_R(Q)$) and the theoretical background is Lorentzian (area $B(Q)$, HWHM $\lambda_B(Q)$). Then

$$\begin{aligned} \Delta(Q) &= \Delta_{G,L}(Q) \\ &= B(Q) \left(\left(1 + 2y(Q)^2 \right) \exp\left(y(Q)^2 \right) \operatorname{erfc}\left(y(Q) \right) - \frac{2}{\sqrt{\pi}} y(Q) \right) \end{aligned} \quad (\text{A.23})$$

where

$$y(Q) = \sqrt{\frac{\ln 2}{2}} \frac{\lambda_B(Q)}{\lambda_R(Q)} \quad (\text{A.24})$$

and $\operatorname{erfc}(y)$ is the error function.⁴

IV. Finally we assume that the resolution is Lorentzian (HWHM $\lambda_R(Q)$) and the theoretical background is Gaussian (area $B(Q)$, HWHM $\lambda_B(Q)$). Then

$$\begin{aligned} \Delta(Q) &= \Delta_{L,G}(Q) \\ &= B(Q) z(Q)^3 \left(\sqrt{\pi} \left(1 + 2z(Q)^2 \right) \exp\left(z(Q)^2 \right) \operatorname{erfc}\left(z(Q) \right) - 2z(Q) \right) \end{aligned} \quad (\text{A.25})$$

where

$$z(Q) = 2\sqrt{\ln 2} \lambda_R(Q) / \lambda_B(Q) \quad (\text{A.26})$$

In Fig. A.1 we plot $\Delta(Q)/B(Q)$ as a function of λ_B/λ_R for all four cases. One observes a strikingly similar behaviour of $\Delta(Q)$ as a function of λ_B/λ_R . The error $\Delta(Q)/B(Q)$ tends to one when $\lambda_B \rightarrow 0$, corresponding to a background $B_{\text{th}}(Q, \omega)$ in Eq. (A.1) which tends to a delta function in ω . Clearly the simple estimate for $E(Q)$ given by Eq. (A.12) breaks down in this limit.

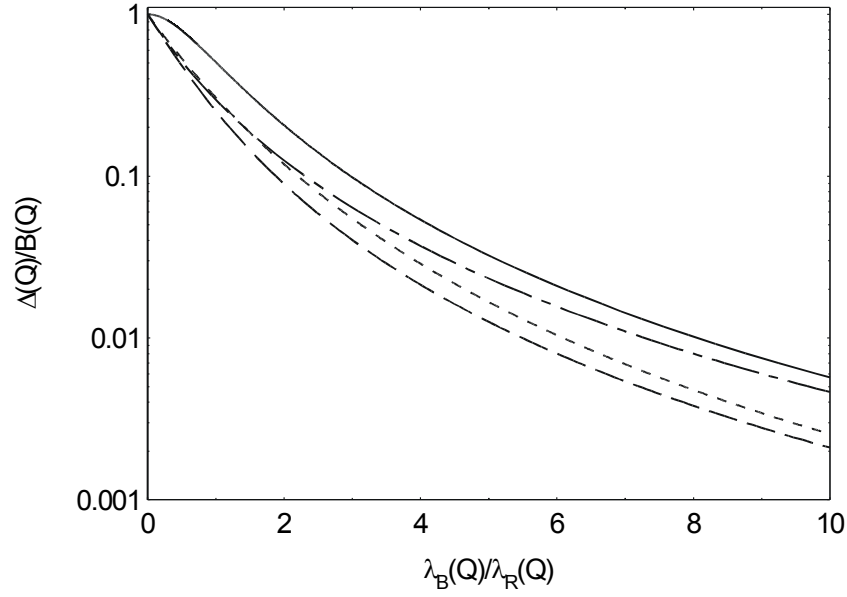


Figure A.1 Relative error $\Delta(Q)/B(Q)$ as a function of the ratio between the halfwidth of the background and the halfwidth of the resolution λ_B/λ_R for a Gaussian background with a Lorentzian resolution (solid line), a Lorentzian background with a Lorentzian resolution (dash-dotted line), a Lorentzian background with a Gaussian resolution (dotted line) and a Gaussian background with a Gaussian resolution (dashed line).

For halfwidths $\lambda_B(Q)$ of $B_{th}(Q, \omega)$ considerably larger than the halfwidths $\lambda_R(Q)$ of the resolution function $R(Q, \omega)$, the error $\Delta(Q)$ quickly decreases proportional to the third power of λ_B/λ_R (cf. Fig. A.1), i.e.

$$\Delta(Q) = B(Q) d_{i,j} (\lambda_R(Q)/\lambda_B(Q))^3 \quad (\lambda_R \rightarrow 0) \quad (\text{A.27})$$

where $i = L, G$ and $j = L, G$ and $d_{L,L} = 8$ (cf. Eq. (A.21)), $d_{G,G} = 2\sqrt{2} = 2.83$ (cf. Eq. (A.22)), $d_{G,L} = (2/\ln 2)^{3/2}/\sqrt{\pi} = 2.76$ (cf. Eq. (A.23)), and $d_{L,G} = 8\sqrt{\pi}(\ln 2)^{3/2} = 8.18$ (cf. Eq. (A.24)). One observes that the error $\Delta(Q)$ is particularly small for Gaussian resolution functions ($d_{G,G} \approx d_{G,L} \approx 2.8$). For general resolution functions $R(Q, \omega)$ and general background functions $B_{th}(Q, \omega)$ one expects Eq. (A.27) for $\Delta(Q)$ to hold with values of $d_{i,j}$ somewhere in between 2.8 and 8.

A.3 Example

We will illustrate our method using the $S(Q, \omega)$ of ferrocene molecules $\text{Fe}(\text{C}_5\text{H}_5)_2$ locked up in KY zeolite at a temperature $T = 200\text{K}$ and a momentum transfer $Q = 1.34 \text{ \AA}^{-1}$ (scattering angle 84°), as measured on the backscattering spectrometer BSS of the Forschungszentrum Jülich. For the resolution function we take the $S(Q, \omega)$ of the same sample at $T = 20\text{K}$, at the same Q .

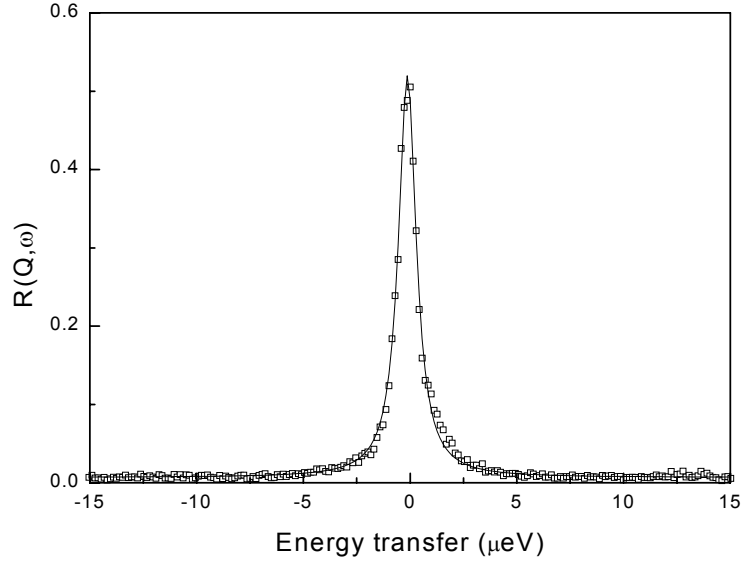


Figure A.2 Resolution function $R(Q, \omega)$ of the neutron backscattering spectrometer BSS at $Q = 1.34 \text{ \AA}^{-1}$ obtained from ferrocene in KY zeolite at $T = 20 \text{ K}$. The solid line is a Lorentzian fit.

The resolution function can be very well described by a single Lorentzian (Fig. A.2), with a HWHM $\lambda_{\text{exp}} = 0.54 \text{ \mu eV}$. Thus we use $R(Q, \omega) = L(\lambda_{\text{exp}}, \omega)$. We then calculate the value for the EISF according to Eq. (A.12) with $\Delta = 0$, using the raw $S(Q, \omega)$ (without any smoothing). We find a value for the EISF of $E(Q) = 0.49$. We then consider $\tilde{S}(\alpha^*; Q, \omega)$ defined by Eq. (A.14) with $\alpha = \alpha^* = E(Q) = 0.49$. The result $\tilde{S}(\alpha^*; Q, \omega) = S(Q, \omega) - 0.49R(Q, \omega)$ is shown in Fig. A.3 (crosses). It appears that $\tilde{S}(\alpha^*; Q, \omega) \approx B(Q, \omega)$ represents the quasielastic broadening fairly well, illustrating our method in practice. One observes in Fig. A.3 that $B(Q, \omega)$ has a HWHM larger than about 2 \mu eV so that λ_B/λ_R is larger than ~ 4 . Using that the area of the background $B(Q) \approx 1 - E(Q) = 0.5$ we derive from Fig. A.3 that the error $\Delta(Q) < 0.02$. Thus for the present case the EISF is given by $E(Q) = 0.49 \pm 0.02$.

We compare this result with that obtained using Fourier transforms. Applying a Fast Fourier Transform algorithm to the raw experimental data $S(Q, \omega)$ we obtain $F(Q, t)$ (cf. Eq. (A.7)) as shown in Fig. A.4. In Fig. A.4 we also show the Fourier transform of the resolution function $F_R(Q, t) = \exp(-\lambda_{\text{exp}} t)$ (cf. Eq. (A.8)), and the ratio $F(Q, t)/F_R(Q, t)$. One sees that both $F(Q, t)$ and $F_R(Q, t)$ tend to zero for $t \rightarrow \infty$ and that as a consequence $F(Q, t)/F_R(Q, t)$ is wildly varying for $t > 7 \text{ ns}$. Obviously it is not possible to determine $E(Q)$ from the limit $F(Q, t)/F_R(Q, t)$ for $t \rightarrow \infty$ (cf. Eq. (A.9)). There is however a small intermediate time region ($1 < t < 3 \text{ ns}$) where the ratio $F(Q, t)/F_R(Q, t)$ is close to $E(Q) = 0.49$. As discussed in the literature^{2,5} trustworthy values of $E(Q)$ can be obtained from such an intermediate time region. Clearly, the Fourier transform method is more

involved than the single integration of Eq. (A.12), while it is not a priori obvious that it is more accurate.

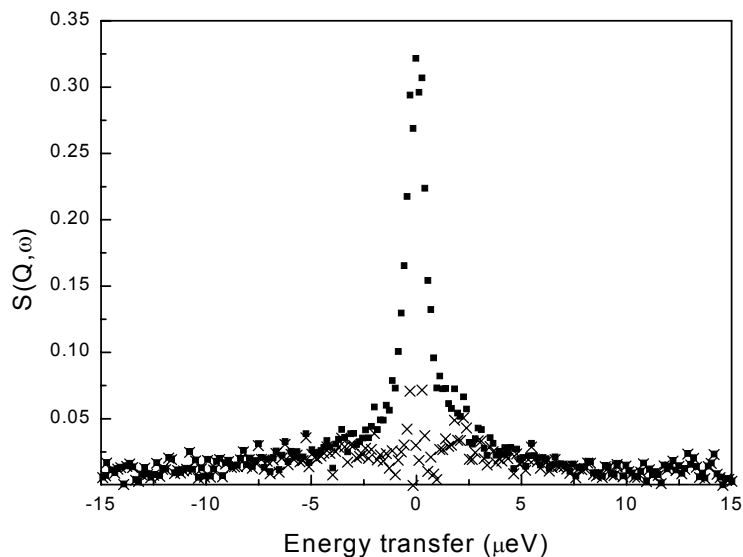


Figure A.3 Quasielastic neutron spectrum $S(Q, \omega)$ (black squares) of ferrocene in KY zeolite at 200 K as a function of ω for $Q = 1.34 \text{ \AA}^{-1}$. The crosses are $S(Q, \omega) - 0.49R(Q, \omega)$ representing the quasielastic broadening for all ω , as explained in the text.

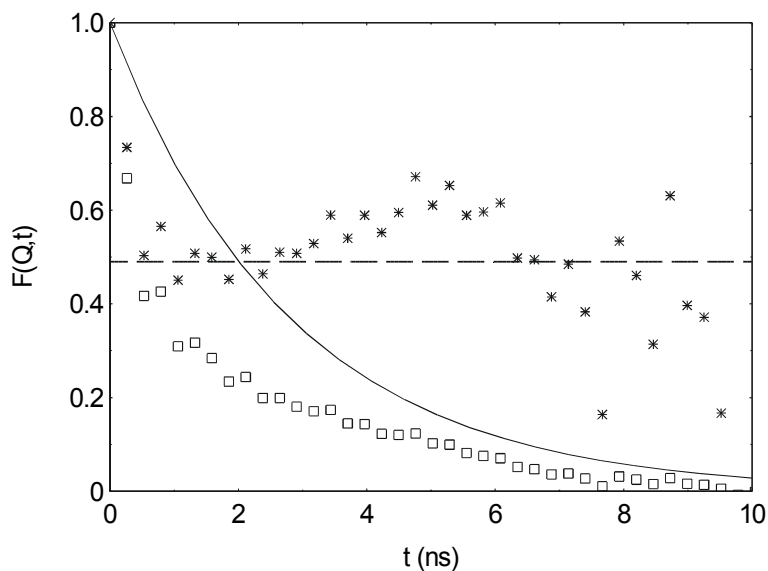


Figure A.4 Fourier transform $F(Q, t)$ of the experimental data (open squares) and $F_R(Q, t)$ of the resolution function (solid line). The crosses give $F(Q, t)/F_R(Q, t)$ approaching the EISF = 0.49 (dashed line) for $t \rightarrow \infty$.

A.4 Conclusions

We have presented a simple, convenient and model independent method to determine the elastic incoherent structure factor $E(Q)$ directly from the measured raw neutron data $S(Q,\omega)$. This method given by Eq. (A.12) works well in practical cases, and its accuracy is good as long as the halfwidth τ_B of the quasielastic broadening is at least two to three times larger than the halfwidth τ_R of the resolution function (cf. Fig. A.1). To determine $E(Q)$ only the experimental data around $\omega = 0$ are needed, where the resolution function $R(Q,\omega) \neq 0$ (cf. Eq. (A.13)). Therefore, unlike the Fourier transform method, our procedure is insensitive to the noise in $S(Q,\omega)$ dominantly present in the side wings.

In practice, our procedure given by Eq. (A.12) is meant to yield a first estimate for $E(Q)$ as a function of Q . From $E(Q)$ one can then determine the possible static geometries given by the parameters, n , \mathbf{R}_i and P_i , in Eq. (A.2). Finally one can apply the usual model fitting procedures to describe $S(Q,\omega)$.¹ The advantage is that models for $B_{th}(Q,\omega)$ are used (e.g. Eq. (A.10)) which are consistent with the behaviour of $E(Q)$ for all Q .

References

1. M. Bée, *Quasielastic Neutron Scattering* (Adam Hilger, Bristol, 1988)
2. F. de Mul & J. Bregman, *Nucl. Instr. Meth.* **98** (1972) 53
3. K.E. Larsson, T. Månsson & L.G. Olsson, in: *Neutron Inelastic Scattering 1977 Vol. I* (International Atomic Energy Agency, Vienna, 1978) 435
4. M. Abramowitz & I.A. Stegun, *Handbook of mathematical functions* (Dover Publications, New York, 1965)
5. P. Verkerk, *Comp. Phys. Comm.* **25** (1982) 325

Appendix B. TOSCA and TFXA

Tosca is an inelastic neutron scattering spectrometer optimised for vibrational spectroscopy. It is the successor of TFXA, which worked in the same way. A schematic diagram of these spectrometers is given in Fig. B.1.

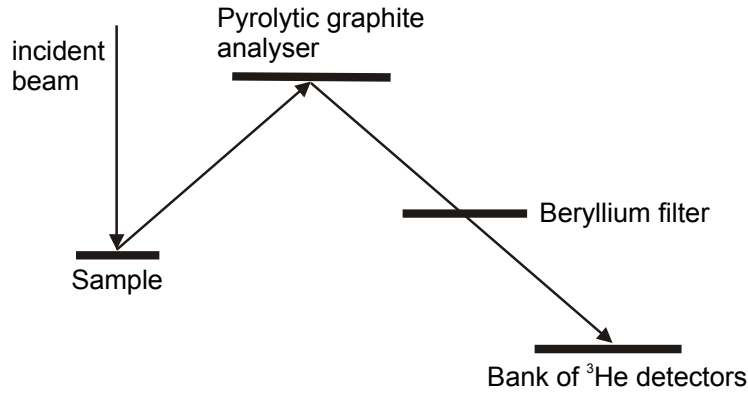


Figure B.1 Schematic diagram of TOSCA and TFXA.

A pulsed white beam of neutrons, originating from a water moderator, is scattered by the sample. The neutrons that are backscattered through an angle of 135° impinge on a pyrolytic graphite crystal that selects, by Bragg reflection, a final neutron wavelength of $\sim 32 \text{ \AA}$. Higher order reflections are suppressed by a beryllium filter. The remaining neutrons are then detected by ^3He filled detector tubes. The time of arrival of a scattered neutron at a detector T is the sum of the time from the moderator to the sample, t_i , and the time from the sample to the detector, t_f ,

$$T = t_i + t_f = \frac{L}{v_i} + \frac{l}{v_f} = L \sqrt{\frac{2E_i}{m}} + l \sqrt{\frac{2E_f}{m}}. \quad (\text{B.1})$$

Here L is the flight path from moderator to sample, v_i the velocity of the incoming neutron, l the flight path in the analyser system and v_f the velocity of the scattered neutron. The velocities are respectively given by the incident neutron energy E_i and the final neutron energy E_f , where m is the mass of a neutron. Since T , L , l and E_f are known we also know E_i , from which the energy transfer from the neutron to the sample is trivially obtained.

Dankwoord

Promoveren doe je niet alleen. Als laatste wil ik daarom graag een aantal mensen bedanken die in het bijzonder geholpen hebben bij het in dit boekje beschreven onderzoek.

Ignatz, dank voor het getoonde vertrouwen en de vrijheid die je me gaf om me bezig te houden met een onderwerp dat voor ons beiden nieuw was. Don, thank you for your enthusiasm and for putting my research on the right track. This thesis would have looked a lot different without your help.

Arian, bedankt voor het bereiden van de samples en voor je hulp bij de metingen op het ESRF. Alexander, veel dank voor je hulp bij de metingen op de BSS, je mooie fitwerk en je enthousiasme over allerlei onderwerpen dat mij ook aanstak. Lambert, bedankt voor je hulp bij de diffractie metingen. Verder wil ik Kees bedanken voor de hulp bij de RKS en Carlo voor de hulp bij IRIS.

Jas, thank you for arranging the INS measurements and for your data on solid ferrocene. A lot of thanks to Hans Grimm, Andy Fitch, Emmanuelle Suard, Stewart Parker and Mark Telling for helping me perform the measurements described in this thesis and for discussing the results.

En alle overgebleven (oud-)collega's, bedankt voor de prettige werksfeer waar ik met veel plezier naar zal terugkijken.

Curriculum Vitae

I was born on the 6th of February 1973 in Amsterdam. After graduating in 1991 from the VWO of the Waterlant College in Amsterdam, I started my physics study at the Delft University of Technology. I specialised in the dynamics of liquid helium at the neutron scattering group of the Interfaculty Reactor Institute. This resulted in the theses 'Dynamics of helium at 13 K and 300 bar' and 'Energy and damping of excitations in liquid helium'. I obtained my Masters degree in August 1996.

In October 1996 I continued working at the Interfaculty Reactor Institute of the Delft University of Technology as a Ph.D. student under the supervision of Prof. dr. G.J. Kearley and Prof. dr. I.M. de Schepper. I investigated the structure and dynamics of molecules in zeolites and focussed on ferrocene in zeolite Y. The main results of this research are presented in this thesis.